The Pennsylvania State University

The Graduate School

Department of Mechanical and Nuclear Engineering

KINETICS OF ZIRCONIUM HYDRIDE PRECIPITATION AND REORIENTATION STUDIED USING SYNCHROTRON RADIATION

A Thesis in

Nuclear Engineering

by

Kimberly B. Colas

Submitted in Partial Fulfillment
of the Requirements
for the Degree of

Master of Science

August 2009

The thesis of Kimberly B. Colas was reviewed and approved* by the following:

Arthur T. Motta
Professor of Mechanical and Nuclear Engineering
Professor of Materials Science and Engineering
Thesis Advisor

Donald A. Koss
Professor Emeritus of Material Science and Engineering

Karen A. Thole
Professor of Mechanical Engineering
Head of Department of Mechanical and Nuclear Engineering

*Signatures are on file in the Graduate School

ABSTRACT

Hydrogen ingress into zirconium alloy fuel cladding during corrosion can degrade cladding performance as a result of the formation of brittle hydrides. Hydride platelets normally precipitate with the platelet habit plane in the transverse-rolling plane of the sheet and are homogeneously distributed through the cladding thickness. Once hydrogen enters the cladding it can respond to a combination of temperature and stress such that hydrides particles reorient with their habit planes normal to the sheet surface and processes such as delayed hydride cracking may occur by preferential reoriented hydride precipitation at crack tips. This reorientation of hydrides can severely reduce ductility, thus it is crucial to understand the kinetics of hydride dissolution and precipitation under stress at temperature. Studies of hydrogen behavior in zirconium alloys are normally performed *post facto*, and suffer both from a scarcity of data and from the confounding effects of studying a hydride microstructure different from that present at higher temperature.

In the current study we have used synchrotron radiation diffraction to study the kinetics of hydride precipitation and dissolution *in situ* (under stress and at temperature). Samples of Zircaloy-4 and Zircaloy-2 hydrided between 80 and 610 wt.ppm and cut in different orientations were examined by transmission x-ray diffraction (using 80 keV synchrotron radiation), while heated and cooled in a furnace at temperatures ranging from 20 to 550ºC and stresses up to 100 MPa. Under these conditions the hydrides dissolved and re-precipitated in a different orientation under sufficiently high stress. A careful study of the intensities and peak broadening of the diffraction peaks as a function of time, stress and temperature allowed the identification of specific characteristics of the diffraction patterns of reoriented hydrides. As a result, the kinetics of dissolution, re-precipitation and orientation of the hydrides could be followed continuously by

monitoring the peak broadening of diffraction peaks. The analysis of the diffraction patterns allowed detailed understanding of the kinetics of the hydride evolution under temperature and stress. Additional experimental techniques were used to enhance the understanding of hydrides in the material such as metallography and reflection x-ray diffraction using synchrotron radiation. Finally a preliminary experiment was performed using micro-beam synchrotron radiation to study hydride precipitation at a crack tip while under stress. The experiment was done at room temperature and under no load on a hydrided cracked sample, and showed the viability of using micro-beam synchrotron radiation to study hydride precipitation at a crack tip.

TABLE OF CONTENTS

LIST OF FIGURES

LIST OF TABLES

ACKNOWLEDGEMENTS

First, I would like to thank my advisor Dr Arthur Motta for his help and guidance during these two and a half years of research. This has been a very enriching learning experience in many aspects. Thank you for the continuous support, advice and commitment during this project.

We are very thankful for the financial support of this research program provided by the National Science Foundation in the Materials World Network. I would also like to thank the CEA (Commissariat à l'Energie Atomique) for letting me use Hydromorph®, one of their hydride analysis programs.

I would also like to thank my collaborators for Queen's University in Kingston, Ontario (Canada), Dr Mark Daymond and Matthew Kerr for their considerable help before, during and after the experiments at the APS synchrotron.

Next, I would like to thank Dr Jonathan Almer and Dr Yong Chu for their help running the experiments at the APS and analyzing the data.

Also, I would like to thank Dr Koss for accepting to review my thesis.

Finally I would like to thank my fellow graduate students for their help in many aspects in and out of the lab: Patrick Raynaud, Michelle Flanagan, Jeremy Bischoff, Jamie Kunkle and Djamel Kaoumi.

Chapter 1

INTRODUCTION

1.1. Zirconium Alloys for Nuclear Fuel Cladding

The core of a light-water reactor (LWR) consists of fuel assemblies that are cooled and moderated by water. Each assembly is made of a series of fuel rods that contain fissile material in the form of uranium dioxide pellets (UO_2). The uranium dioxide pellets are contained in cladding tubes made of zirconium alloys. This cladding serves as the first barrier of fission product containment between the nuclear fuel and the primary coolant, which in the case of LWR is water.

Zirconium alloys have been chosen as cladding material primarily for their very low thermal neutron absorption cross-section (0.185 barns (or $0.185 \times 10^{-24} cm^2$) for 0.0253eV neutrons) which allows a higher operating efficiency of the reactor [1] . Zirconium alloys also exhibit good corrosion resistance, appropriate mechanical strength for reactor conditions and are, to a certain extent, resistant to radiation damage [2].

During in-reactor operation the zirconium cladding is subject to environmental degradation. The cladding tube is under stress from the pressure of the fission gases emitted by the uranium pellet and can develop chemical bonding with the pellet itself. The typical temperature of the inner cladding wall is about 400ºC. The outer wall of the cladding is in contact with the cooling water and its temperature is approximately 350ºC. At this boundary waterside corrosion can occur, leading to hydrogen pickup by the cladding. Radiation damage also affects the properties of the cladding. Typically during the 3 years operating lifetime of the fuel rod each atom in the zirconium cladding is displaced 20 times (20 dpa).

Historically the alloy most often used in PWRs (Pressurized Water Reactors) is Zircaloy-4, while Zircaloy-2 is used in BWRs (Boiling Water Reactors). Recently, PWRs have started to use more modern alloys such as Zirlo and M5 which exhibit improved corrosion resistance [3, 4]. The chemical compositions of Zircaloy-4 and of Zircaloy-2 are given in Table 1-1.

Table 1-1 Composition of alloying elements for Zircaloy-4 and Zircaloy-2[2]

Element (wt.percent)	Zr	Sn	Fe	Cr	O	Ni
Zircaloy-4 (wt.percent)	Balance	1.2-1.7	0.18-0.24	0.07-0.13	1000-1400 wt.ppm	NA
Zircaloy-2 (wt.percent)	Balance	1.43-1.45	0.13-0.14	0.1	1260-1440 wt.ppm	0.05

Zircaloy-4 is a two-phase alloy characterized by a hexagonal close packed (hcp) zirconium matrix containing a fine dispersion of intermetallic precipitates such as $Zr(Cr,Fe)_2$. Zircaloy tubes used in PWRs have a wall thickness of 0.6-0.7 mm, a diameter of 9.5-10.0 mm and are approximately 4 m long. The extrusion process used during fabrication produces a textured microstructure, leading to strong anisotropic mechanical behavior. In the cold-worked-stress-relieved (CWSR) condition, the texture is such that most of the grains have their c-axes tilted 30-40º away from the normal to the sheet or tube surface along the transverse direction [2].

1.2. Hydride Formation in Fuel Cladding

1.2.1. Structure and Morphology of Zirconium Hydrides

As discussed in Section 1.1, in the reactor environment the zirconium cladding reacts with the cooling water to form a layer of zirconia (ZrO_2) on the cladding surface. The reaction shown below liberates hydrogen which can be absorbed by the cladding:

$$Zr + 2H_2O \rightarrow ZrO_2 + 4H \qquad 1\text{-}1$$

Hydrogen is also generated by radiolysis [5] according to the following reaction:

$$H_2O \underset{\gamma,n}{\rightarrow} H^+ + OH^- \qquad 1\text{-}2$$

Some of these hydrogen atoms are transported to the metal oxide interface and can be absorbed into the cladding. This is called hydrogen pick-up. The absorbed hydrogen migrates through the material in response to thermodynamic driving forces, such as concentration and thermal gradients, which can cause local concentrations in the form of blisters or rims. For Zircaloy-4, 10-20% of the hydrogen liberated from corrosion is typically absorbed into the cladding. Hydrogen precipitates forming zirconium hydrides when the hydrogen content reaches the solubility limit in the α-zirconium matrix. The terminal solubility limit (TSS) of hydrogen in α-zirconium during a temperature rise (thus TSSd for dissolution) is given in Figure 1-1 from [6-8] and also by the following equation:

$$\text{TSSd (wt.ppm)} = 120000 \exp(-35770/RT) \qquad 1\text{-}3$$

where T is the temperature in Kelvin and R is the gas constant.

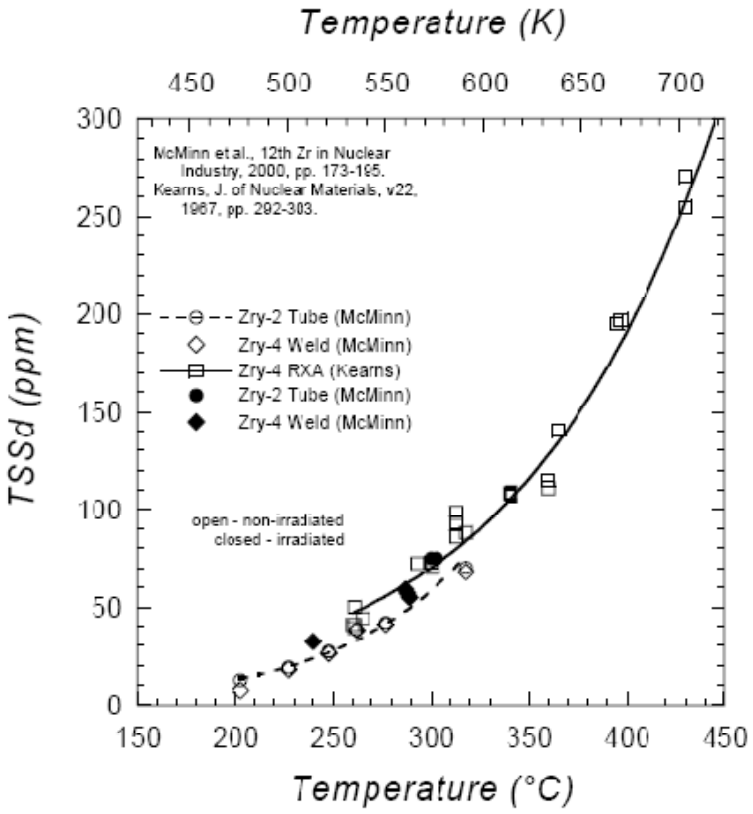

Figure 1-1 Terminal solid solubility of dissolution (TSSd) of hydrogen in the alpha phase of Zircaloy-2 and Zircaloy-4[6, 8]

The determination of the terminal solid solubility limit is discussed in the following section (Section 1.2.2). As seen in Figure 1-1 the terminal solubility limit of hydrides is about 100 wt.ppm at 350ºC. When this limit is reached hydrogen atoms react with zirconium atoms and precipitate as zirconium hydrides.

The phase diagram for the zirconium-hydrogen system is given in Figure 1-2 [9]. The zirconium-hydrogen system has the particularity to allow hydrogen super-saturation during cool-down. This means the alpha zirconium phase can contain more hydrogen during cool-down that the phase diagram allows [10]. For example, at 300ºC the alpha zirconium matrix can contain 75wt.ppm more than is allowed in solid solution. This leads to a lower precipitation temperature and a higher dissolution temperature than predicted by the phase diagram, and thus a hysteresis phenomenon exists for the dissolution and precipitation temperatures of hydrogen in zirconium.

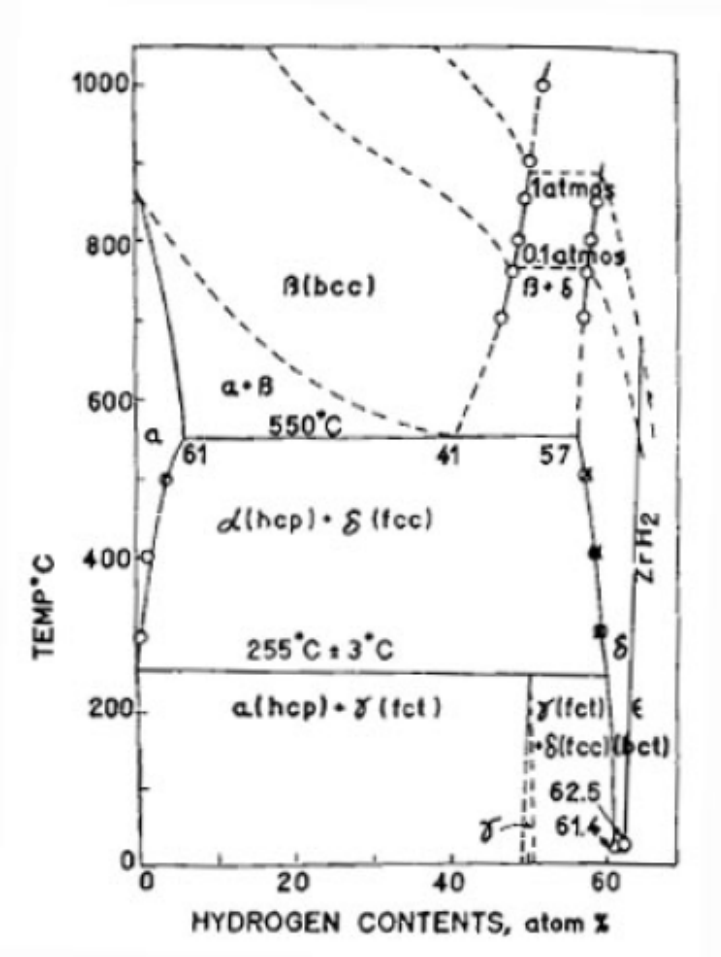

Figure 1-2 Zirconium-hydrogen binary phase diagram showing α- and β-Zr phases and δ-, γ- and ε-hydride phases by [9, 11].

It has been observed experimentally that zirconium could absorb much more hydrogen than previous studies on the solubility limit of hydrogen in alpha zirconium have shown. This excess hydrogen has been observed to re-distribute along the grain boundaries. This phenomenon called 'supercharging' is in contradiction with the thermodynamic principles that state that the hydrogen concentration should increase until the solubility limit is reached [10, 12]. These hydrogen atoms diffuse through the material without forming hydrides, then, once the solubility limit is reached the hydrogen atoms would precipitate at the outer surface of the material which is where the solubility limit is reached first. The hydride layer formed will then grow in a similar fashion to a zirconia oxide layer. This hydride layer formation has been observed in samples hydrided by cathodic charging, but not by gaseous charging or by waterside corrosion. For these

cases, hydrogen atoms distribute as hydride precipitates in the matrix. Hillner has shown that the hydrogen precipitation was not continuous with decreasing temperature, as illustrated in Figure 1-3 [13]. In this figure, the hydrogen concentration decreases by steps instead of following the continuous solubility curve. From Hillner's studies, it has been concluded that as hydrides are precipitated in the matrix, the matrix can accept more hydrogen than expected by the predicted solubility limit. Marino modeled the diffusion and growth of hydrides in Zircaloy and found that, depending on the speed of growth of hydride precipitates, hydrogen charging occurs either by supersaturation or by formation of a hydride film [14].

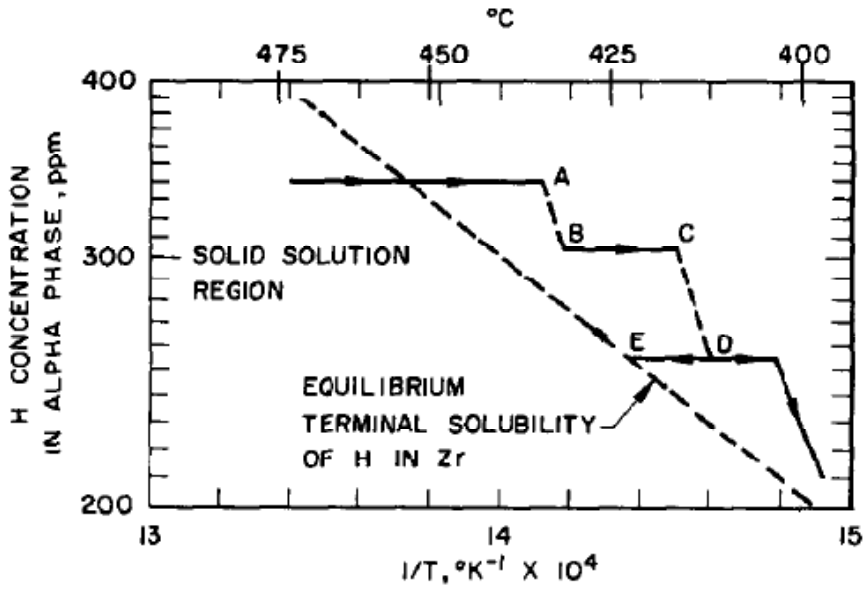

Figure 1-3 Concentration of hydrogen in alpha phase during cooling or zirconium samples containing 340 wt.ppm hydrogen[13]

As seen in Figure 1-2 three types of zirconium hydrides have been identified: the stable δ phase, the metastable γ phase and the ε phase. All these phases have different chemical composition and crystallographic properties. Their crystallographic properties and compositions are summarized in Table 1-2. The morphology and orientation of these hydrides in α-zirconium is different for each phase, as summarized in Table 1-2. All these phases have a different settlement mode in the matrix to accommodate the volume expansion attendant after precipitation; these settlement modes are also described in Table 1-2. The transformations that lead to the formation

of the different hydride phases are presented in Table 1-3. There has been some controversy in the literature on the formation of γ hydrides. Several studies suggest than γ hydrides would appear only upon quenching of zirconium alloys [15], whereas some studies suggest than γ hydrides would only appear for samples hydrided to more than 640 wt.ppm [16]. Finally it has been suggested by Mishra et al.[11] that the γ hydride phase is in fact an equilibrium phase resulting from a peritectoid reaction of α-Zr and δ hydride below 255ºC. Figure 1-2 shows that the γ hydride and the α-Zr are in equilibrium at low temperatures and at hydrogen contents less than 50 atom percent (%) or about 10,000 wt.ppm. Above this concentration, the γ hydride and δ hydride are in equilibrium [17].

Table 1-2 Crystallographic properties of the different zirconium hydride phases; all parameters are given at room temperature [12, 18]

Hydride Phase	Chemical composition	Crystal structure and parameters	Orientation relationship with α-Zr	Mode of settlement of precipitate	Morphology and habit planes
δ stable	ZrH_x $1.53 \leq x \leq 1.66$	Face-centered cubic; a=0.4777-0.4779 nm	$[1\text{-}10]_\delta // [11\text{-}20]_\alpha$ and $(111)_\delta // (0001)_\alpha$	Mostly plastic	Platelets // (0001) or (10-17)
γ metastable	ZrH	Tetragonal Face-centered; a=0.4617 nm c=0.4888 nm	$[1\text{-}10]_\gamma // [11\text{-}20]_\alpha$ and $(111)_\gamma // (0001)_\alpha$	Elastic and plastic	Needles //<11-20>
ε	ZrH_x $1.71 \leq x \leq 2$	Tetragonal Face-centered; a=0.488-0.502 nm c=0.457-0.436 nm c/a=0.935-0.865			

Table 1-3 Transformation characteristics for the different hydride phases [10, 12, 18-20]

Hydride	Cooling rate	Volume change	Transformation type
δ stable	<2ºC/min	16.3-17.2%	Martensitic: transformation of hexagonal lattice of α-Zr in FCC lattice then dilatation under the influence of H which is in tetrahedral sites (1/4,1/4,1/4) and their equivalent. The site's radius is 0.0378nm and there are 2 sites per Zr atoms
γ metastable	>2ºC/min	12.3-15.7%	The γ phase forms from the α-Zr phase by shear deformation of the hexagonal lattice and by simultaneous diffusion of H atoms. A similar process occurs for the δ to γ transition.
ε			The ε phase appears after low temperature martensitic transformation of the δ phase

When hydriding occurs during normal reactor operating conditions the phase observed is the δ phase. These precipitates ZrH_x ($1.53 \leq x \leq 1.66$) have 60.4 to 62.4 at. % hydrogen and their density is 5.65g/cm^3. Their formation is enhanced by the oxygen concentration above 1000 wt.ppm, by slow cooling (in reactor or in a furnace) and require sufficient amount of hydrogen (above 100 wt.ppm). Our study will focus on hydride formation conditions in which δ hydrides form since they are the most relevant to reactor conditions and to spent fuel storage [21].

Now that the different phases of hydrides have been detailed, we will focus on the morphology and habit planes of the δ-hydrides. It is now well accepted that the large hydride precipitates are formed by aggregation of smaller hydride platelets [22-24]. Figure 1-4 shows in schematic form the smaller hydride platelets forming the larger hydride precipitate by coalescing.

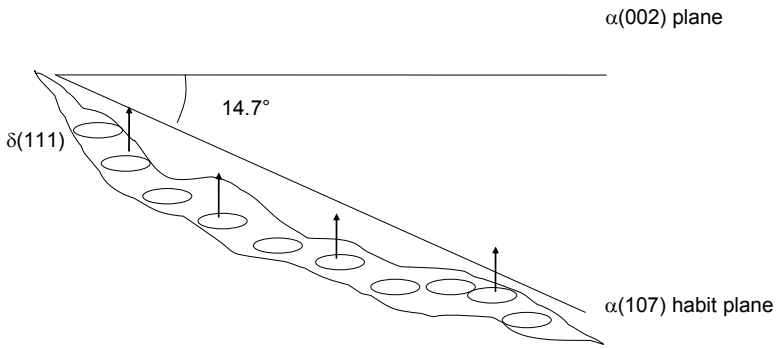

Figure 1-4 Cartoon representing the aggregation of microscopic hydride platelets to form macroscopic hydrides [12].

The habit plane of the microscopic platelets and the plane where the macroscopic hydrides precipitate are not the same [25]. The face of the macroscopic hydrides is parallel to the $\{10\bar{1}7\}_{Zr}$ plane, the pole of which is oriented 14.7º from the basal poles. The microscopic hydride platelets (represented by small ellipses in Figure 1-4) precipitate with their faces parallel to the $\{0002\}_{Zr}$ crystal plane. Table 1-4 summarizes the dimensional information and habit planes of the macroscopic hydrides and microscopic hydride platelets normally formed in α-zirconium for material from BWR and PWR cladding in the cold work stress relieved state (elongated grains and a high density of dislocations). Hydrides can precipitate inter- or intra-granularly (which of the two sites is predominant is still under discussion). It appears that the nucleation location depends on the local stress state [24] which would explain why the macroscopic hydride habit plane can be very different than that of the microscopic hydride platelet. Figure 1-5 from [25] illustrates why circumferential hydrides are not strictly aligned since the basal planes are oriented at ±30º from the radial direction and why macroscopic hydrides present this wavy shape. Macroscopic hydrides are a long chain of smaller precipitates that are precipitated in different grains that have different orientation of the basal planes which are at either +30º or -30º from the

radial direction. Since the macroscopic hydrides lie 14.7º from the basal planes, for each grain, they will have a slightly different orientation and thus exhibit a non-linear aspect when observed by optical microscopy.

Table 1-4 Dimensions and habit planes of macroscopic hydrides and microscopic hydride platelets [12, 25]

	Dimensions	Habit plane
Macroscopic hydrides (seen by SEM or by etching and optical microscopy)	Length: 2000 to 10000 nm Thickness: 100 to 200 nm	$(10\text{-}17)_{Zr}$ at 14.7º from basal planes
Microscopic hydride platelets (observed by TEM)	Length: 100 to 200 nm Thickness: 30 to 50 nm Grain size: 5x10 µm (inter- or intra-granular precipitation)	$(0002)_{Zr}$ (or near dislocation loops for irradiated materials)

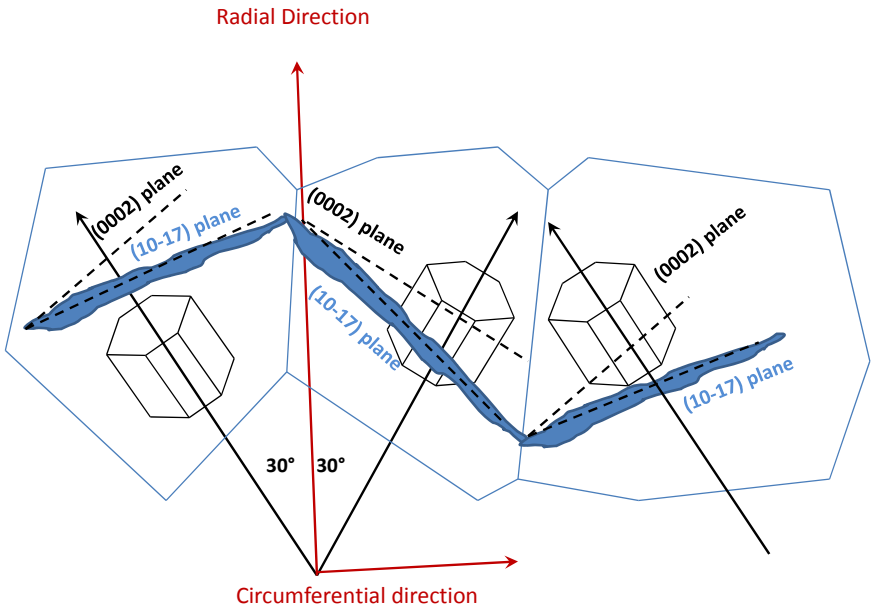

Figure 1-5 Macroscopic hydride orientation and habit planes with respect to the zirconium matrix[25]

The question of macroscopic hydride orientation is very important, since hydrides that are precipitated in the radial direction of a cladding or pressure tube (radial hydrides) can considerably degrade the material's resistance to fracture. In unstressed material, it is the thermo-

mechanical processing history that will influence the macroscopic hydride orientation [26]. When the material is stressed during cooling, the macroscopic hydride orientation depends both on texture and on the applied stress and hydride reorientation may occur. Certain conditions favor hydride re-orientation under stress. The first condition that enhances hydride re-orientation is that the material must present an appropriate texture such as one with many basal poles aligned parallel to the stress direction [26]. Also only hydrides that are dissolved in solid solution can be re-oriented. This explains why determining accurately the terminal solid solubility limit is essential to the study of re-oriented hydrides. Another very important feature in stress induced re-orientation of hydrides is that when compressive stress is applied hydrides re-orient *parallel* to the stress direction whereas when a tensile stress is applied they re-orient *perpendicular* to the stress direction [27]. The discussion of the parameters influencing hydride terminal solid solubility and hydride re-orientation under stress is detailed in the following.

1.2.2. Previous Studies on Hydride Dissolution, Precipitation and Re-Orientation

The terminal solid solubility (TSS) determination is essential for a better understanding of the behavior of zirconium hydrides. Kearns' study on the terminal solubility limit using the diffusion couple method has been widely used as the reference for TSS determination [7]. This study states that below 550ºC which is a thermodynamic equilibrium, the following equation determines the TSS:

$$\mathbf{TSS\ (wt.ppm) = 120000\ \exp(-4302/T)} \qquad \mathbf{1\text{-}4}$$

where T is the temperature in Kelvin.

A hysteresis phenomenon has been observed in several studies between the TSS for dissolution (TSSd) and the TSS for precipitation (TSSp). Using differential scanning calorimetry, McMinn studied the effect of different parameters on the TSSd and the TSSp [8]. For unirradiated Zircaloy materials the TSS equations were found to be:

$$TSSd\ (wt.ppm) = 106\ 446.7 \exp(-4328.67/T)$$
$$TSSp\ (wt.ppm) = 138\ 746.0 \exp(-4145.72/T) \quad 1\text{-}5$$

Where TSSd and TSSp are the hydrogen terminal solid solubility for dissolution and precipitation respectively in wt.ppm; T is the temperature in Kelvin.

For irradiated Zircaloy materials the TSS equations were found to be:

$$TSSd\ (wt.ppm) = 24\ 236.1 \exp(-3391.1/T)$$
$$TSSp\ (wt.ppm) = 212.1 \exp(-1003.6/T) \quad \text{for } T<170^{o}C \quad 1\text{-}6$$
$$TSSp\ (wt.ppm) = 66\ 350.1 \exp(-3557.2/T) \quad \text{for } T>170^{o}C$$

Where TSSd and TSSp are the dissolution and precipitation hydrogen concentrations respectively in wt.ppm; T is the temperature in Kelvin. These equations illustrate the fact that the behavior for dissolution and precipitation is very different for irradiated material than for unirradiated material, as illustrated in Figure 1-6. McMinn's results indicate that there is little effect of material composition or microstructure on the TSSd and TSSp for unirradiated material. This result is confirmed by Bertolino's work [28]: in oxygen-strengthened tungsten inert gas (TIG) welded material it was found that oxygen additions could significantly influence the TSS likely as a result of hydrogen trapping by the oxygen solute. Increasing the peak temperature and the hold time at peak temperature resulted in a decrease of the TSSp and an increasing hysteresis between TSSd and TSSp. This has been explained by the memory effect that results from preferential sites such as dislocation networks, which allow easier precipitation. At higher temperatures this memory effect can be diminished or removed by annealing the material. It was found that heating and cooling rates over the ranges of 0.5 to 10ºC/min have little effect on the measured dissolution an precipitation temperatures. The effect of stress on the TSSd and TSSp has been studied by Eadie and Coleman by observing hydride precipitation at a flaw [29]. The equation they give governing the effect of stress on the TSS is given by:

$$\Delta \ln TSS = p(V_{H\text{-}Hydr} - V_H)/RT \quad 1\text{-}7$$

Where the TSS is in wt.ppm, p is the hydrostatic stress, $V_{H\text{-}Hydr}$ and V_H are the partial molar volumes of hydrogen in the delta hydride and the alpha zirconium phases respectively (1.4 x 10^{-6} m^3 per mole and 1.67 x 10^{-6} m^3 per mole respectively). After several studies using different

techniques (such as time-of-flight neutron diffraction), stress was found not to have a strong effect on the TSS [29].

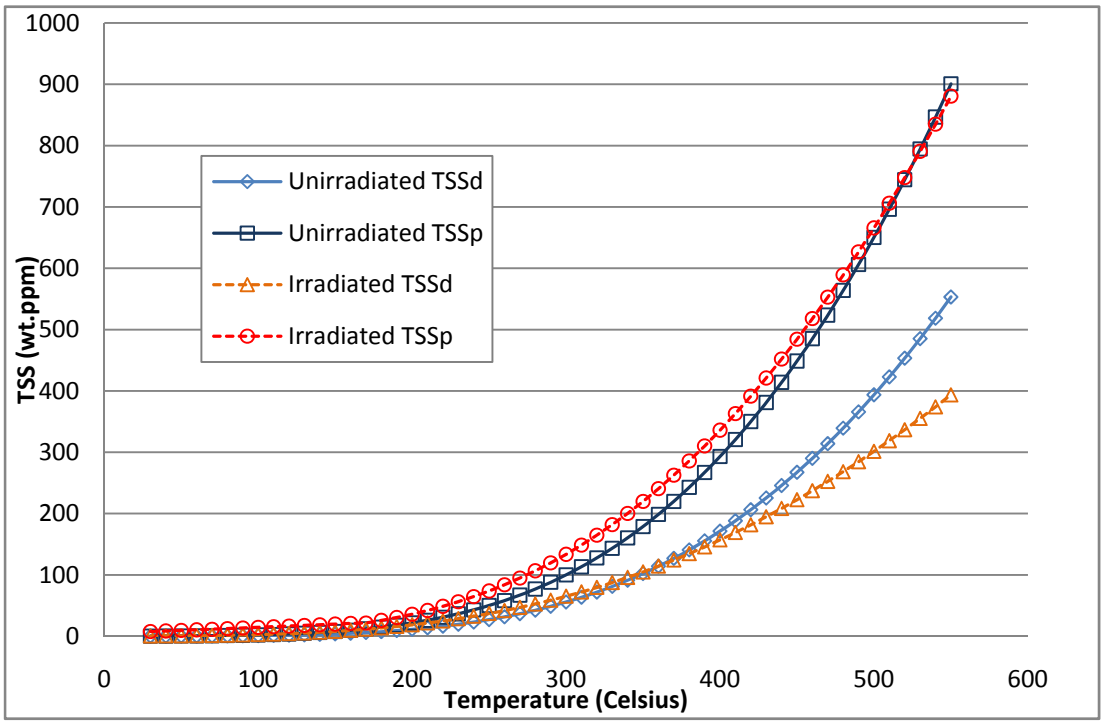

Figure 1-6 Comparison of McMinn's equations for the TSSd and TSSp of unirradiated and irradiated material[8].

The study of the kinetics of hydride dissolution and precipitation and the re-orientation of hydrides is another essential element in the characterization of hydride behavior in nuclear fuel cladding. Mishima used electrical resistivity measurements to study the kinetics of hydride precipitation in unalloyed zirconium [30]. He used a simple rate law to analyze his data:

$$-dn/dt = Kn^{\gamma} \qquad 1\text{-}8$$

where n is the normalized hydrogen content in solution, γ is the order of the reaction and K is a constant.

It was found that the order of the reaction was approximately one for ageing temperatures between -16 and -35ºC, and approximately two at even lower ageing temperatures. For higher temperatures (above 14ºC), the precipitation kinetics were too rapid to allow a precise

determination of γ. Kearns used a simple diffusion model to determine the rates of hydride dissolution as a function of hydride platelet thickness h (cm) [6]:

$$t = 1.65\ h^2 \exp(24900/RT) \qquad 1\text{-}9$$

where t is the dissolution time in seconds, and T is the temperature in Kelvin (R is the gas constant). The actual times for dissolution below the eutectoid temperature of 550ºC are short, on the order of tens to hundreds of seconds, and are shown as a function of reciprocal temperature in Figure 1-7[6]. The data points obtained in this figure are from metallography analysis of samples that were heated and quenched in ice-brine at different times during the heating stage. The calculated curves come from diffusion equations. In Figure 1-7, the observed times for complete dissolution range from 1 to 300 seconds. Times required for the samples containing 114 and 205 wt.ppm hydrogen were about triple those required for the 60 wt.ppm sample. This difference is attributed to the existence of coarser hydrides in the former samples.

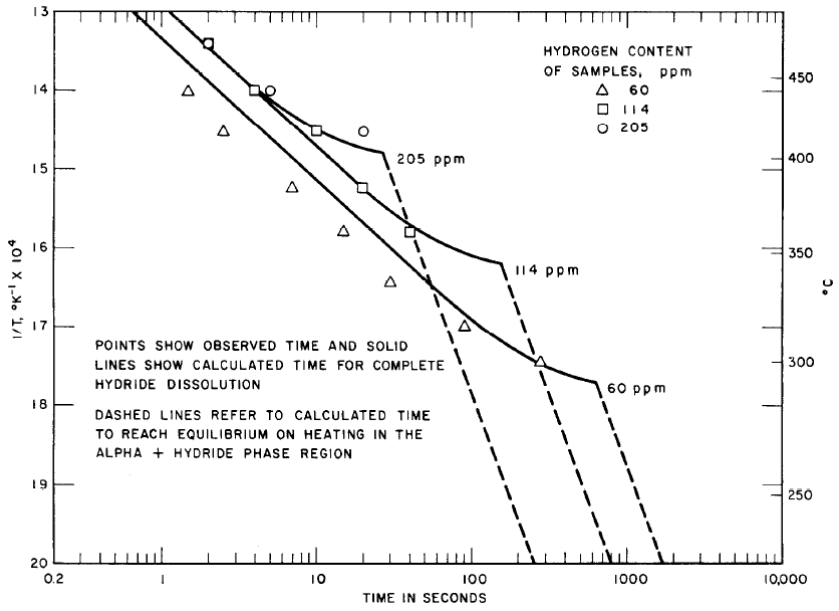

Figure 1-7 Effects of temperature and hydrogen content on the isothermal dissolution kinetics of zirconium hydride [6]

Similar calculations were made to obtain the time to reach equilibrium in the two-phase region hydrides-zirconium matrix:

$$t = 3.5\text{x}10^{10}\ h^2/C^2 \exp(8380/RT) \qquad 1\text{-}10$$

where t is the time in seconds, C is the hydrogen concentration in wt.ppm, and h is the thickness of the platelets in cm (R is the gas constant).

Using differential calorimetry measurements, Une studied the precipitation and dissolution kinetics of hydrides in Zircaloy-2 and high Fe Zircaloy [31]. It was found that the precipitation rate could be modeled as:

$$H_p \text{ (wt.ppm/s)} = 1.18 \times 10^3 \exp(-35716/RT) \qquad 1\text{-}11$$

where H_p is the precipitation rate, T is the temperature in Kelvin and R is the gas constant. Finally, more recently, using neutron diffraction, Root obtained the curves presented in Figure 1-8 for the dissolution kinetics of hydrides in Zr-2.5Nb [32]. The following equation was used to fit his data:

$$I_N = A(H_T - C_0 \exp(-Q/RT)) \qquad 1\text{-}12$$

where A is a constant, H_T is the total amount of hydride that would be formed if all hydrogen was precipitated (this is an adjustable parameter related to the total hydrogen content), C_0 is approximately the TSS, Q is analogous to the molar enthalpy of precipitation (found to be 30 kJ/ mol for the heating curve and 28 kJ/mol for the cooling curve), R is the gas constant and T is the temperature in Kelvins. Root also proposes that hydride precipitation and dissolution could involve very slow processes (with time constants in the order of hours) because the hysteresis found in his data between the TSSp and TSSd is not significant, in contrast to other studies [7, 8]. Another study from Kammenzind observed the migration of hydrogen atoms to zones of higher stresses and the re-orientation of hydrides upon precipitation of these atoms during cool-down [33]. He demonstrated that the effect of stress on the TSS was small and that thermal cycling increased the transfer of hydrogen atoms under an applied-stress gradient. It was also demonstrated that any effect of an applied stress on hydrogen migration was small compared to the effect of temperature i.e., when both temperature and stress gradients are present in a sample, the temperature gradient has the strongest effect on the migration of hydrogen atoms.

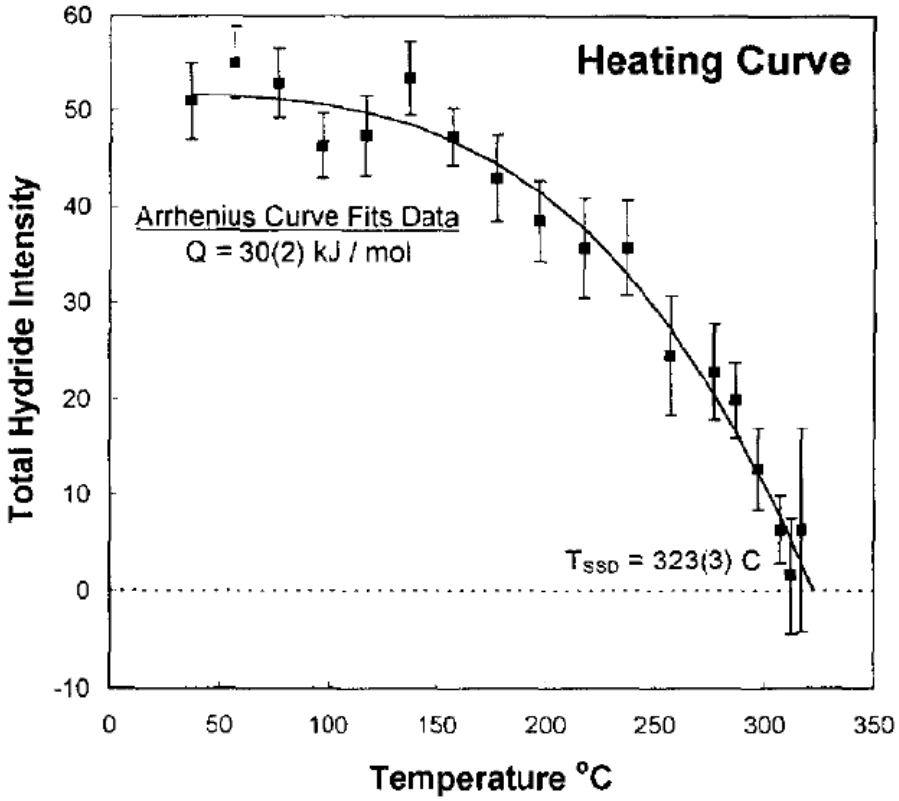

Figure 1-8 The reduction of total diffraction peak intensity as the temperature of the specimen is increased. The continuous line is the fitted function [32].

The final essential behavior of interest of the zirconium hydrides is their capacity to re-orient under stress. Since this is a very important phenomenon that can lead to the embrittlement of nuclear fuel cladding, it has been thoroughly studied throughout the years. It has been found that certain factors influence the hydrides capacity to re-orient. Hardie et al. showed that a favorable texture of the zirconium matrix in Zr-2.5Nb strongly influences hydride re-orientation [26] (a favorable texture is one that presents a high concentration of basal poles parallel to the direction of applied stress). It was also demonstrated that a threshold stress existed for re-orientation and that the degree of rearrangement depended on stress, temperature history and the hydrogen concentration in the material. The data in this study were found to be well fitted using Ells' equation[34]:

$$R_\sigma = F/(F_m - F) \qquad 1\text{-}13$$

where R_σ is the ratio of the number of hydrides oriented within a particular angle of the direction perpendicular to the applied stress to those outside this angle; F is the % radial hydride (lying within 0 to 45º of the perpendicular to the applied stress), and F_m is the maximum % radial hydride obtained for a particular hydrogen content and temperature. For example for a specimen containing x wt.ppm cooled under stress from a temperature where the hydrogen solubility was y wt.ppm, $F_m = 100y/x$. Hardie used the following relation for R_σ:

$$R_\sigma = R_0 \exp(B\sigma) \qquad 1\text{-}14$$

Where R_0 is the ratio in the absence of stress, B is a fitting parameter and σ is the applied stress (in N/mm^2).

A study of the value of the threshold stress σ_{th} was performed by Singh [35]. It was found that σ_{th} decreased non-linearly with an increase in re-orientation temperature. For a given temperature and hydrogen content, the degree of re-orientation was found to increase with re-orientation stress. Also at temperatures lower that 473 K, competition from existing circumferential hydrides reduced the efficiency of re-orientation. Finally a study by Kim et al. [36] demonstrated that the smaller hydride platelets that compose the larger macroscopic hydrides by stacking always had the same habit plane $\{0001\}_\alpha$ even when re-orientation under applied stress of the macroscopic hydrides occurred using X-ray diffraction pole figures. The {111} pole figure pattern of the reoriented hydrides was very similar to that of the $\{0001\}_\alpha$ of the initial α-zirconium matrix. Thus, nucleation of the reoriented hydrides occurred in a limited area keeping the initial texture ahead of the crack tip. It was concluded from this that the re-oriented hydrides nucleate first within the α-zirconium grains, keeping initial texture and maintaining the orientation relationship of $\{111\}_\delta$ // $\{0001\}_\alpha$.

We now focus on the reason of interest for such studies, the delayed hydride cracking phenomenon, a potential form of hydrogen embrittlement in nuclear fuel cladding and in CANDU pressure tubes.

1.3. Delayed Hydride Cracking

Zirconium alloys cladding tubes are susceptible to hydride embrittlement, as described in the previous section. One particular form of hydride embrittlement is called delayed hydride cracking (DHC). This is a time-dependent crack growth process resulting from the stress-assisted diffusion of hydrogen to the crack tip, followed by the formation of radial hydrides and the subsequent fracture of the hydrides in the crack-tip region resulting in a crack advance at a stress intensity factor $K<K_{IC}$ [10, 37, 38]. As explained in the previous section, the most common orientation for zirconium hydrides in cladding tubes is in the circumferential direction. However, under a crack-tip stress field or a stress gradient, the hydrogen atoms in solid solution migrate to the tip of the crack, in the direction of increasing stress gradients. In CANDU reactors, DHC occurs in the Zr-2.5%Nb pressure tubes especially in the weld regions [38, 39]. DHC has also been suspected as the possible cause of fuel failure in reactivity-initiated accidents such as those tested in the French CABRI test reactor [40]. The onset of DHC is controlled by the growth threshold, K_{IH}, which is the stress intensity factor that a crack must exceed for DHC growth to occur [41-43]. The main factors influencing DHC and its growth threshold are the applied stress, the size of cracks and defects present, temperature profile in the cladding, hydrogen content, texture, fluence and cooling rate [29, 41, 44, 45]. Alloy composition, microstructure and heat treatment might also affect the DHC susceptibility of an alloy.

Thus DHC is a serious issue, and developing a mechanistic understanding of this phenomenon is essential to enable safe operation of nuclear fuel.

1.4. Motivation of Study

In the previous sections, it was demonstrated that the behavior of hydrogen in cladding must be well understood for a safer storage of spent-fuel or a safer operation of CANDU reactors. The key elements of its understanding are the determination of the hydrogen terminal solid solubility limit and the factors that influence it, the determination of hydride orientation and morphology as a function of stress, temperature, texture, heating and cooling rates and the kinetics of hydride dissolution and precipitation. As seen in the previous sections, most of the studies on DHC and on hydride dissolution and precipitation have been performed post-facto. There is presently much uncertainty on the DHC mechanisms, at least partly because the examinations have been conducted post-facto (after cool-down and stress relaxation). These factors can confound the interpretation of results. As a result parameters such as the actual concentrations of hydrides at the crack tip necessary for advancement, the kinetics of precipitation under different states and levels of stress as well as temperatures are not well known and any prediction from these studies cannot be accurate enough for reactor conditions or spent fuel storage. The objective of this work is to present a new type of *in-situ* experiment by using synchrotron radiation. Using the unique capacity of third generation synchrotron to perform high resolution diffraction, Zircaloy samples can be studied by x-ray diffraction (XRD). As a result the precipitation/dissolution of pre-existing hydrides can be studied while it occurs. The use of two dimensional detectors and transmission XRD allows us to obtain the full texture information on re-oriented hydrides. The in-situ data obtained in these experiments can help address on the TSS determination and on hydride dissolution and precipitation phenomena that might not be observed when studies are led post-facto or with very long incubation times such as for neutron diffraction. Finally the observation of hydrides at the tip of a crack by micro XRD will enable us to have a better understanding of how the hydrides precipitate during DHC and thus have a better mechanistic understanding of this phenomenon.

Chapter 2

EXPERIMENTAL PRODEDURES

2.1. As-Received Material

Zircaloy-2 and Zircaloy-4 base alloys were used in this study. The Zircaloy-2 material used was taken from a warm-rolled and fully re-crystallized square bar of 60 x 60 mm^2; this produced an equiaxed grain structure with an average diameter of 20 μm. The Zircaloy-4 furnished by Western Zirconium was in the form of a 0.5 mm thick sheet in the cold-rolled stress-relieved condition. As a result the grains are not equiaxed, but elongated in the rolling direction. For both sets of samples the following orientation convention will be used (RD) Rolling Direction, (ND) Normal Direction to rolling and (TD) Transverse Direction to rolling. The Zircaloy-2 material used in this study has been well characterized in terms of texture/mechanical properties as discussed below [46]. The texture was obtained by neutron diffraction and the $\{0002\}$ and $\{10\bar{1}0\}$ pole figures are shown in Figure 2-1. The pole figure shows a strong normal texture, with the basal poles concentrated along the normal direction to rolling, with some intensity along the transverse direction and little intensity in the rolling direction. Quantitatively this is assessed by calculating the associated Kearns factors [47]. The Kearns factor is a parameter that quantifies basal pole intensity and is calculated for a given reference direction. The Kearns factor is defined as the resolved fraction of basal poles along a particular macroscopic direction. For example, for the normal direction of the model material, the Kearns factor (denoted f_N) is given by Equation 2-1:

$$f_N = \int_0^{\pi/2} I_\phi \sin\phi \cos^2\phi \, d\phi \qquad 2\text{-}1$$

where I_Φ is the average basal pole density at an angle Φ from the reference direction (in this case the normal direction). The value of the Kearns factor can vary between 0 (indicating perfect alignment of basal poles perpendicular to the reference direction), and 1 (indicating perfect alignment of basal poles parallel to the reference direction). When basal poles are randomly distributed in all directions, the Kearns factors f_N, f_R, and f_T equal 1/3 for the three reference directions. For the Zircaloy-2 square bar used in this study, the values of the Kearns factors are: $f_N = 0.887$, $f_T = 0.101$ and $f_R = 0.012$.

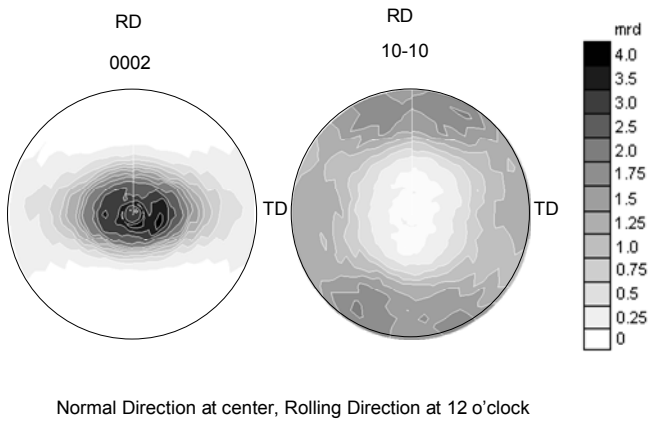

Figure 2-1 Basal {0002} and prismatic {$10\bar{1}0$} pole figures for the Zircaloy-2 plate. The intensity scale is shown on the right [Courtesy of M. Daymond, Queen's University, Kingston, ON Canada].

The mechanical properties for this slab of Zircaloy-2 were characterized by tensile and compressive testing at Queen's University. The resultant stress/strain curve is presented in Figure 2-2. These curves fully characterize the mechanical behavior of the samples used in this study for different orientations at room temperature. To calculate the yield stress at temperature a MATPRO model was used[48]. The equation chosen to calculate Young's modulus at temperature is given by Equation 2-2:

$$E[GPa] = 10^9 \times (1.088 \times 10^{11} - 5.475 \times 10^7 \times (T + 273)) \qquad 2\text{-}2$$

In this Equation E is the elastic modulus in GPa and T is the temperature in Celsius. The resultant yield stress was calculated using Hooke's law

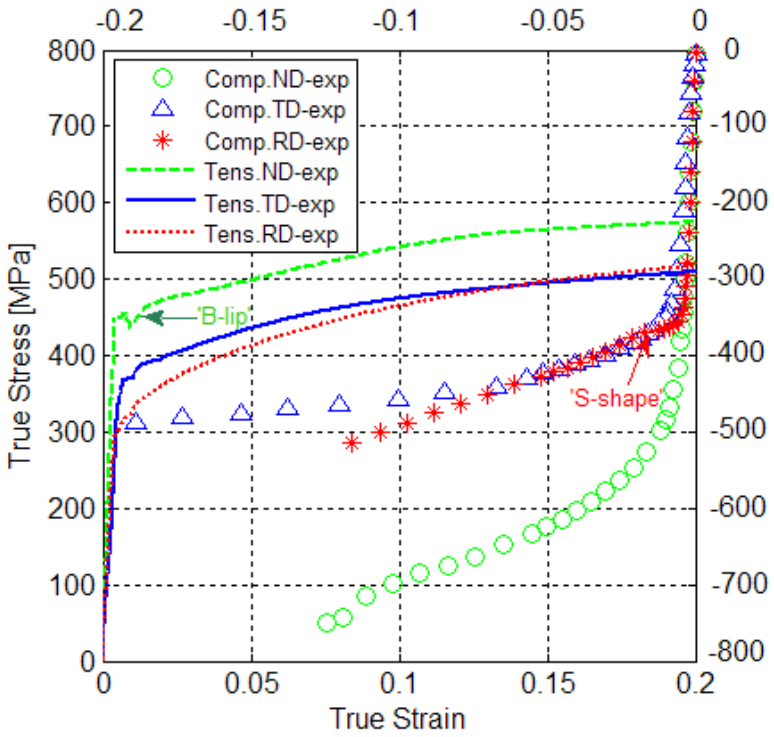

Figure 2-2 Stress-Strain curve for the Zircaloy-2 slab measured at Queen's University at room temperature [Courtesy of M. Daymond, Queen's University, Kingston, ON Canada].

2.2. Sample Preparation

2.2.1. Preparation of Samples with Different Orientations

In order to study the effect of texture, two sample geometries were used in two different orientations for the Zircaloy-2 and the Zircaloy-4 samples, as illustrated in Figure 2-3. The rectangular plain sheet sample on the left was machined from the Zircaloy-2 square bar in different orientations as illustrated by the left hand side of Figure 2-3(b) and used for the bulk diffraction experiments with scattering vectors along normal direction (ND) and transverse direction (TD). The rolling direction (RD) is the direction of rolling for both the Zircaloy-2

square bar and the Zircaloy-4 thin sheet, the normal direction (ND) is perpendicular to the rolling direction coming out of the rolled surface and the transverse direction (TD) is perpendicular to the ND and the RD and is in the plane of the rolling surface. The second, dog-bone type tension samples were machined from the Zircaloy-4 thin sheet and from the Zircaloy-2 square bar (in different orientations as well for Zircaloy-2) and used for the in-situ experiments (with scattering vectors along ND and TD for the Zircaloy-2 and ND and RD for the Zircaloy-4). The right hand side of Figure 2-3(b) shows basal planes are oriented about 30º from the normal direction in the ND-TD plane which is the initial texture of the Zircaloy-2 square bar.

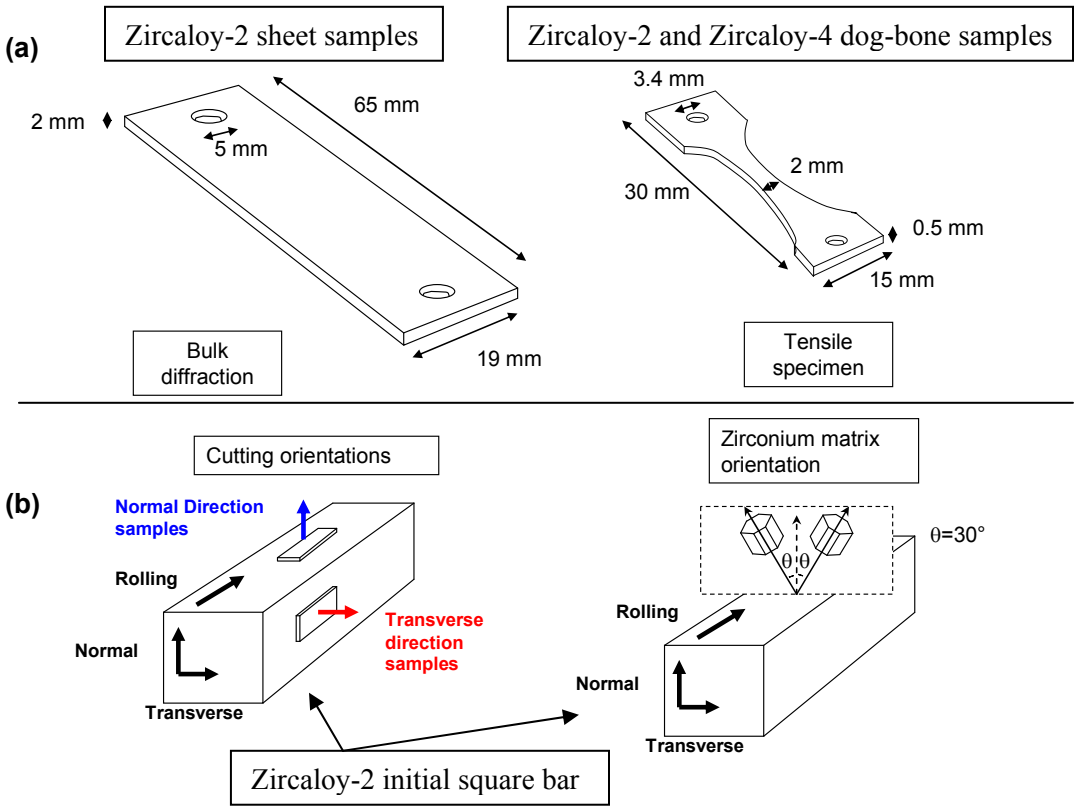

Figure 2-3 (a) Sample geometries (bulk diffraction) on left and dog-bone specimen on the right; (b) Sample orientation and matrix texture

2.2.2. *Hydrogen Charging Procedures*

These samples were hydrogen-charged by high temperature gas diffusion, for which several steps were needed. First, the native oxide layer present on the surface of the samples was removed by dipping the samples for 1 minute in an acid solution of 1 part HF, 10 parts nitric acid and 10 parts H2O. Second, using an electron-beam evaporator available at the Penn State University National Science Foundation (NSF) National Nanotechnology Infrastructure Network (NNIN) facility, a thin layer of nickel was deposited onto the sample surface to prevent oxidation [49]. The samples were then hydrogen-charged in a vacuum furnace using a mixture of 12% hydrogen and 82% argon, introduced at 450°C. Several temperature cycles were necessary to charge to the desired level of hydrogen. The typical temperature profile is presented in Figure 2-4. The total time at 450˚C was 3 hours, so no significant re crystallization occurred [27]. The samples were charged to different contents varying between 96 wt.ppm and 1280 wt.ppm of hydrogen. A more detailed description of the hydrogen charging set-up is presented in Appendix A. The first estimation of how much hydrogen the sample absorbed was done by noting the pressure drop in the furnace before and after the temperature cycles. In most cases, for the first cycle there was a pressure drop of approximately 10% which suggest most hydrogen has been absorbed since the gas mixture that is inserted in the furnace is a 12.5% H and 87.5% Argon mixture. In the following cycles it appeared that less hydrogen was absorbed, since a very small or no pressure drop was observed. In addition to the pressure drop measurement, the weight of each sample was measured before and after hydriding and the mass difference was an indicator of how much hydrogen had been absorbed. This first approximation method was found to be relatively accurate when compared to hot vacuum extraction for samples of masses equal or above 4g. For lighter samples the measurement was not precise enough. For a more exact determination of the hydrogen contents actually obtained, hot vacuum extraction was performed

by Luvak Inc (Boylston, MA). More information on the estimation of hydrogen contents are in Section 3.1.

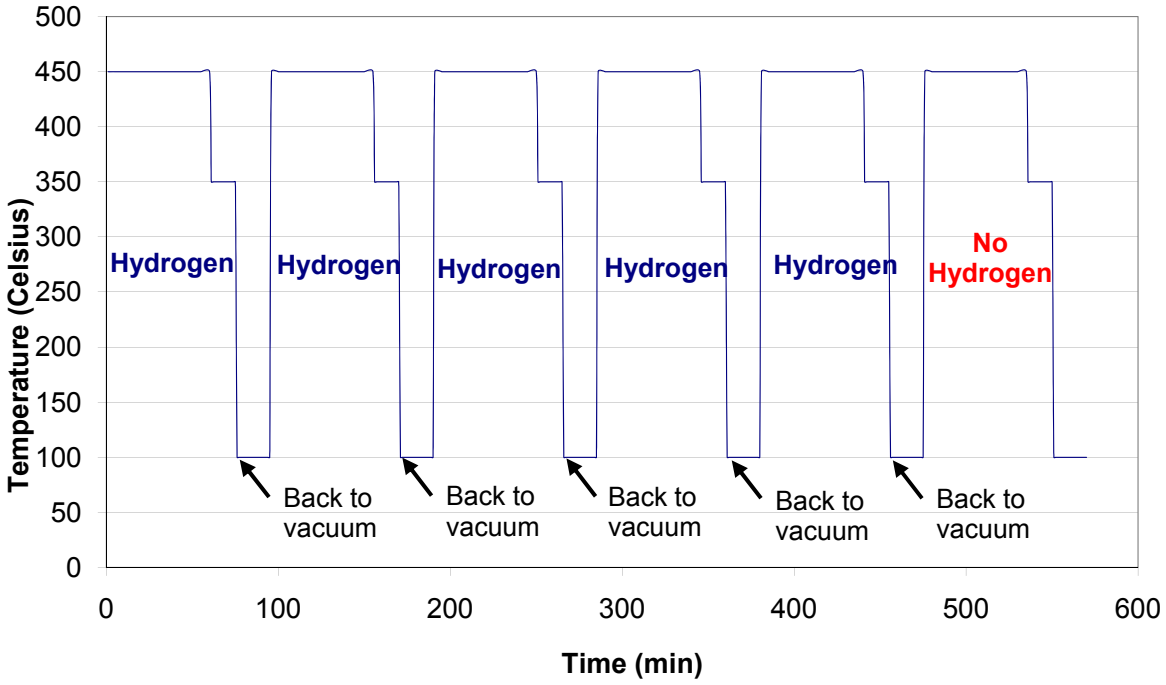

Figure 2-4 Hydrogen charging temperature cycle

2.2.3. Heat-Treatment and Tensile Loading of Samples

In preparation for the post-facto experiments performed at beamline 2-BM (see Section 2.4 for more details) some of the bulk Zircaloy-2 samples were heat-treated with or without stress. A tensile loading system designed and fabricated at Penn State for the bulk samples, was used to apply a stress during the heat cycles. The system, shown in Figure 2-5 and Figure 2-6, consists of two grips which can put the sample in tension, and which are connected by a screw which can be used to apply a desired strain. The tensile device had to respect the following principles: capacity to apply a tensile and compressive stress to the sample, conservation of mechanical characteristics at 400ºC and stability and uniform loading of the system. The loading system was fabricated out of 304 Stainless Steel. In order to estimate the applied stress to the

sample during the heat cycle, the difference between the thermal expansion coefficients of stainless steel and zirconium was taken into account and the number of turns of the main screw was recorded. By combining both applied stresses from thermal expansion difference and applied loading with the screw, we were able to determine the total applied stress on the samples.

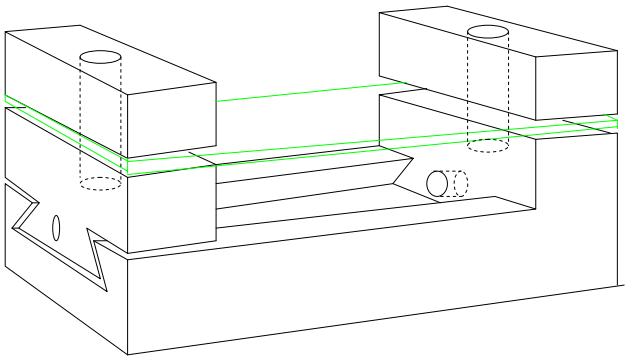

Figure 2-5 Tensile device, the sample is represented in green (note: the screws are not represented).

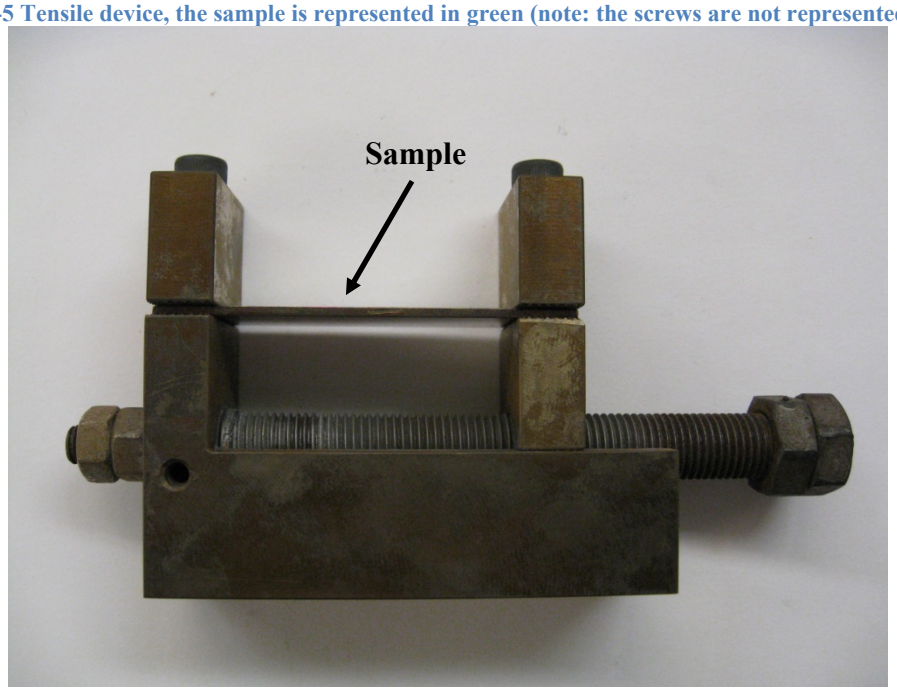

Figure 2-6 Picture of the tensile device with sample loaded (arrowed).

Using the tensile device, two hydrogen-charged samples for each direction ND and TD (ND samples have the normal direction coming out of their sheet surface; TD samples have the transverse direction coming out of their sheet surface) were loaded using the tensile device (four samples in total). Only elastic deformation was necessary for our experiments, so a stress of approximately 50% of the yield stress needed to be applied. Since the samples were cut in different orientations, the yield stress was not the same for all samples. The values of the yield stress at room temperature were taken from Figure 2-2 and the value at higher temperature was calculated using the MATPRO model described in Section 2.1. As a result for the Transverse Direction samples the applied stress will be 225 MPa in the compression mode and for the Normal Direction samples the applied stress will be 185 MPa in tension mode. The cycles for heat treatment are shown in Figure 2-7.

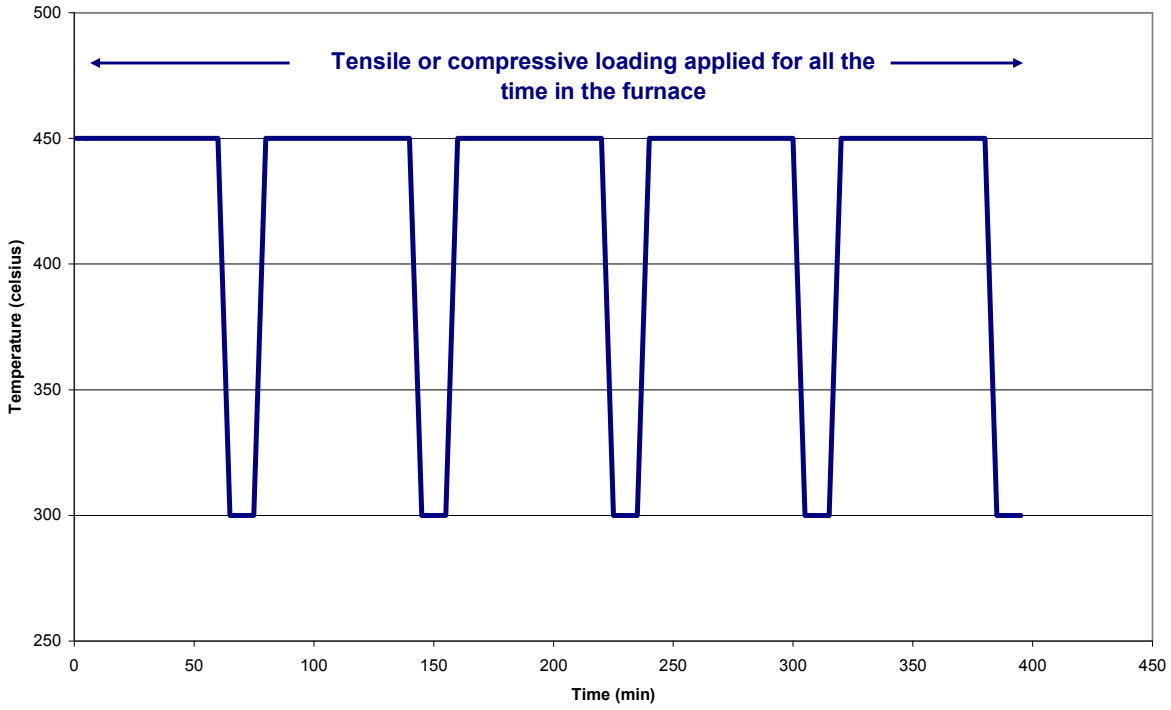

Figure 2-7 Heat treatment temperature cycle with loading

2.2.4. *Crack-tip Sample Preparation*

The crack-tip sample used in the micro-beam diffraction experiment (see Section 2.4 for more details) was a Zircaloy-2 sample cut from the square bar described in Section 2.1. The sample was prepared by Matthew Kerr at Queen's University. The sample was 2 mm thick and hydrided up to 100 wt.ppm using a cathodic hydriding technique [50]. The sample dimensions are 20x20x2 mm^3. The sample was fatigue pre-cracked; then hydrides were dissolved by taking the sample up to 400ºC under vacuum. Hydrides re-precipitated at the tip of the crack upon cool down forming crack-tip hydrides [51]. All the sample preparation was done by Matthew Kerr at Queen's University. The resulting crack tip hydrides can be seen on a Scanning Electron Microscopy (SEM) image on Figure 2-8, courtesy of Stephanie Stafford, Kinetrics Inc. The hydrides are the darker elongated features. They are situated at the tip of the fatigue crack and some of the hydrides are cracked due to loading that was applied to this sample. This SEM image is a surface image representing the hydrides and the cracks at the surface of the CT sample and not the state inside the sample thickness.

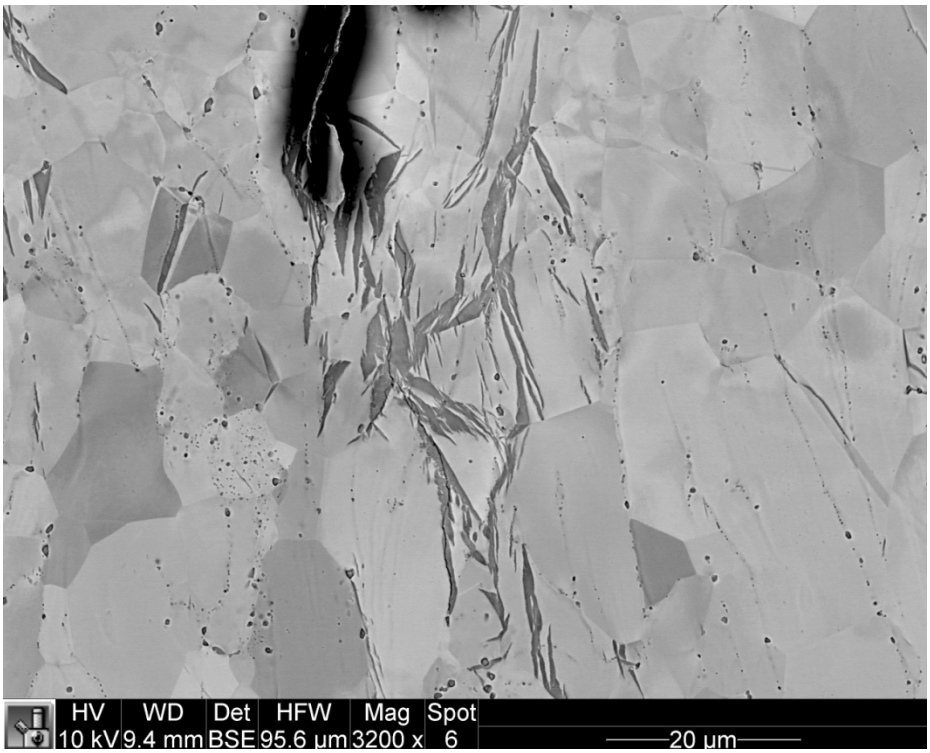

Figure 2-8 SEM picture of a crack-tip Zr-2.5Nb sample [courtesy of Stephanie Stafford, Kinetrics, Inc.].

2.3. Metallography

Metallography was performed to characterize initial hydride orientation and morphology and to estimate the hydrogen content using image analysis. The samples were cold-mounted in epoxy casts and mechanically polished with 180 to 1200 grit silicon carbide paper, followed by chemical etching using the same solution used for oxide layer removal (10 parts water, 10 parts nitric acid and 1 part hydrofluoric acid). This solution preferentially etched the zirconium hydrides, which allowed their observation using optical microscopy. Figure 2-9 shows a typical metallograph obtained for Zircaloy-2 samples hydrided at 500 wt.ppm and Figure 2-10 shows a typical metallograph obtained for Zircaloy-4 samples hydrided at 500 wt.ppm. The hydrides platelets are the dark lines on the white zirconium matrix. We can notice that the hydrides present

a preferential orientation since they are all aligned in a similar direction; this feature will be discussed in details in Section 3.2.

Some image analysis of the metallographs was performed in this study. The first type of image analysis was realized with ImageJ® which was used to transform the metallographs into binary images with only black and white pixels. This was made by adjusting the threshold value to transform levels of grey into black and white. Another software used for image analysis was Hydromorph® which is a program developed by the CEA (*Commissariat à l'Energie Atomique*, French Atomic Energy Commission). This program identifies individual hydrides from the metallographs, extract a 'hydride skeleton' and can measure their orientation, their length, the number of branches they are made of, etc as illustrated in Figure 2-11. Several options to define each of these parameters are possible. To define the particle orientation, we chose to have the program calculate the weighted average of the orientation; this means that for a particle made of two branches with different length, the orientation will be defined as the orientation of one branch multiplied by the length of this branch plus the orientation of the other branch times its length, and all this would be divided by the sum of the two branches lengths. The particle length was defined as the distance between the two farthest points of the particle. These parameters were tested on several samples of known geometry to validate their relevance. To determine the radial hydride content of a sample, each individual particle was counted as either circumferential hydride, mixed hydride or radial hydride. The circumferential hydrides were those with an orientation between 0 and 40º from the normal direction (or circumferential direction for a cladding tube), the mixed hydrides had an orientation between 40 and 65º from the normal direction and the radial hydrides had an orientation between 65 and 90º form the normal direction. The radial hydride content in percent was defined as:

$$RHC = (0.5 \times MH + RH)/N_{TOTAL} \qquad 2\text{-}3$$

where the RHC is the radial hydride content in percent, the MH is the number of mixed hydrides, RH is the number of radial hydrides and N_{TOTAL} is the total number of hydrides. This definition of radial hydride content was found to be accurate for our type of sample geometry.

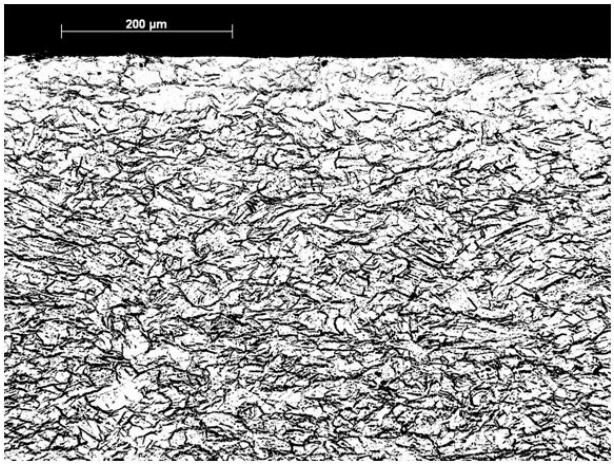

Figure 2-9 Optical metallograph of Zircaloy-2 sample hydrided at 500 wt.ppm.

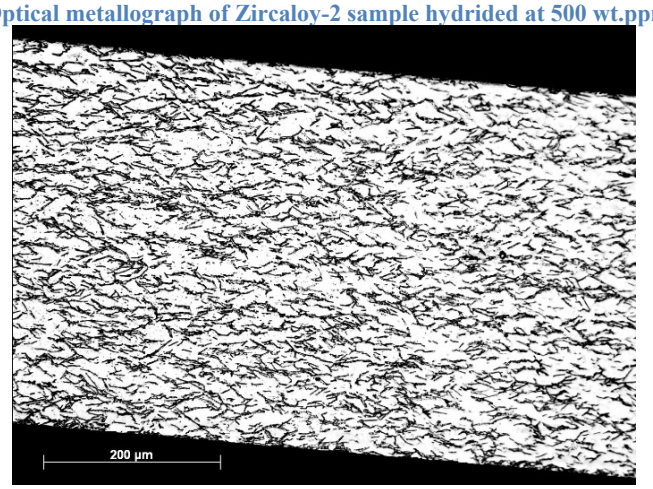

Figure 2-10 Optical metallograph of Zircaloy-4 sample hydrided at 500 wt.ppm.

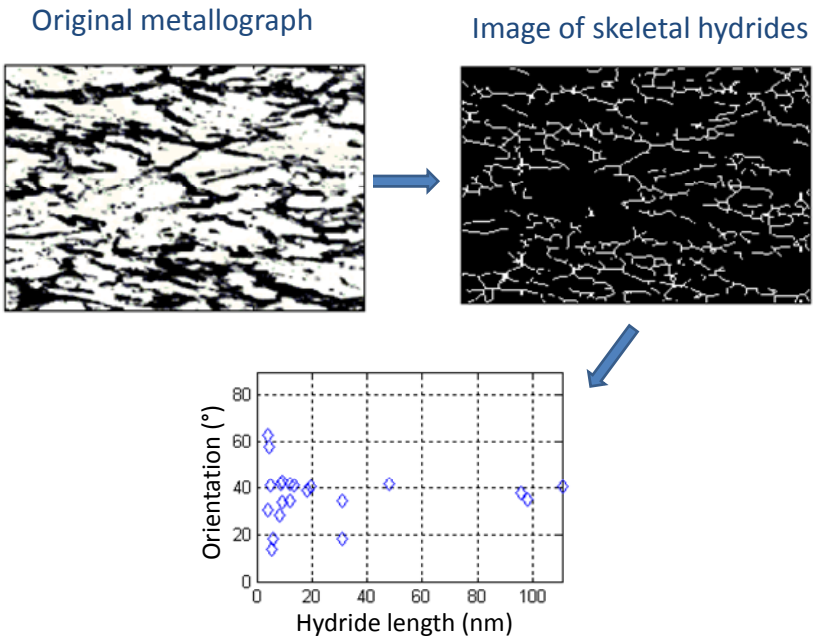

Figure 2-11 Hydromorph analysis process: from the original metallograph to the individual hydride orientation by identifying each individual hydride.

2.4. X-Ray Diffraction Experiments Using Synchrotron Radiation

2.4.1. General Description of XRD using Synchrotron Radiation

The main technique used in this study is synchrotron radiation X-ray diffraction at the Advanced Photon Source (APS) at Argonne National Laboratory (Argonne, Ill). The APS is a third generation synchrotron which produces X-rays at a very high brilliance which allows enhanced resolution and high energy radiation compared to conventional laboratory X-ray sources such as Cu-Kα for example. In addition, the high photon flux can be produced over a various range of energies. In the experiments performed for this study, several incoming energies were used to study our samples, allowing flexibility and customization of our experiments. The high photon flux also enables us to detect small volume fractions of phases that would otherwise

not be detected. The brilliance on the other hand is a measure of the intensity (photons per second per unit area) and directionality of the X-ray beam through its divergence (milliradians squared). In the next sections, the different beamlines used for our experiments, 2-BM, 1-ID and 2-IDD are described. Their position along the APS synchrotron ring is presented in Figure 2-12. Table 2-1 represents the peak positions of the phases of interest for the three different beam energies used in the APS experiments described in the following sections. These peak positions were calculated from the powder diffraction files (PDF) presented in Appendix B using Bragg's Law [52, 53]:

$$\lambda = 2\, d \sin\theta \qquad 2\text{-}4$$

where λ is the wavelength (m), d is the interplanar spacing (m) and θ is the diffraction angle (radians).

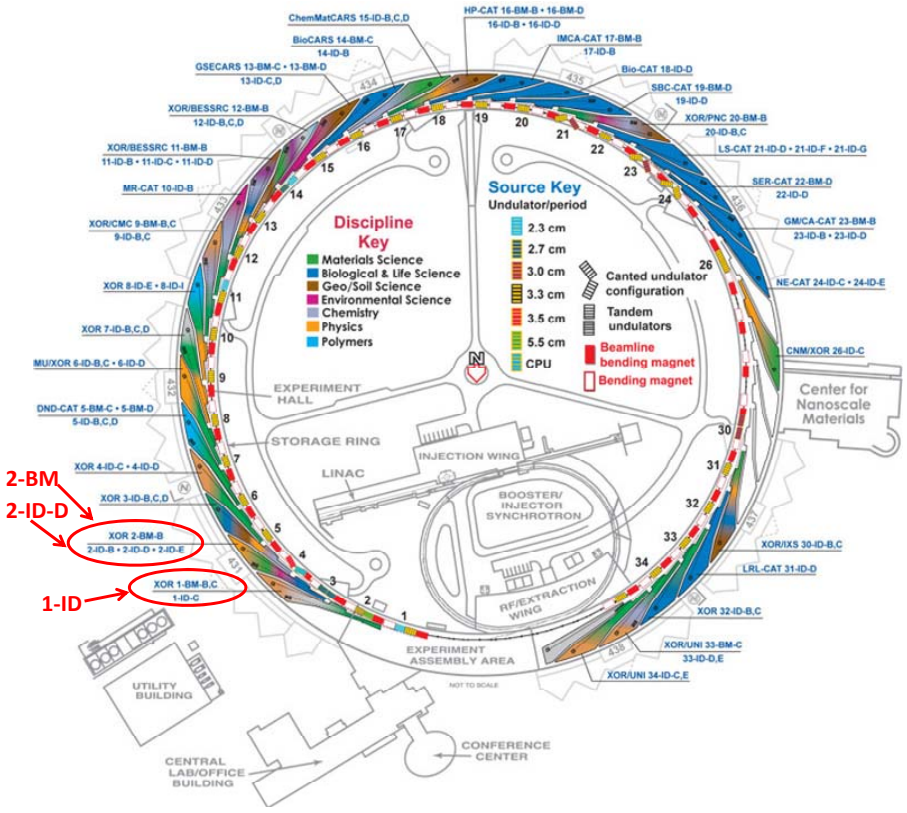

Figure 2-12 Advanced Photon Source synchrotron and position of the beamlines used in our experiments

Table 2-1 Peak position for the phases of interest for all three beam intensities used in the APS experiments

Phase (hkl)	80keV 2θ peak position(°)	15keV 2θ peak position(°)	10.1 keV 2θ peak position(°)	Relative Intensity
α(100)	3.1744	16.990	25.347	33
α(002)	3.4521	18.488	27.605	32
α(101)	3.6122	19.354	28.912	100
α(102)	4.6903	25.211	37.823	17
α(110)	5.4977	29.639	44.650	17
α(103)	6.0732	32.822	49.618	18
α(200)	6.3513	34.369	52.053	3
δ(111)	3.2181	17.226	25.702	100
δ(200)	3.7149	19.910	29.753	47
δ(220)	5.2568	28.313	42.598	37
δ(311)	6.1617	33.314	50.390	43
γ(111)	3.2655	17.481	26.086	100

2.4.2. *Reflection XRD Experiment at Beamline 2-BM at the APS*

Experiments at 2BM were conducted in reflection using a theta-two theta scattering geometry, as illustrated in Figure 2-13(a). Monochromatic 15 keV x-rays (λ= 0.0827 nm) were used which leads to an interaction depth of about 25 μm. The beam was slit to 1mm x 10mm. X-rays were detected using an NaI point detector with horizontal and vertical acceptances of 1 and 5 mrad. The diffraction measurements were carried out using a conventional four-circle diffractometer. A more detailed description of the beamline set-up is described in [54].

The samples examined received different hydrogen charging and heat treatments with and without load prior to coming to the APS as described in Section 2.2 and were observed post-facto at room temperature. Table 2-2 summarizes the samples studied at beamline 2-BM. The main objective of this experiment was to observe the relative influence of stress and texture on hydride orientation by studying samples subjected to different thermo-loading cycles. In order to

study the kinetics of hydride precipitation near a crack tip, which is an essential problem of DHC, it is important to observe how hydrides re-orient under stress. An objective of this experiment was to observe this orientation behavior of hydrides under tensile stress and for different initial textures. Metallography was used to verify if the results found using XRD at the APS were coherent. This experiment was also used to perform hydride phase identification. X-Ray diffraction patterns can be indexed and analyzed to measure the hydrogen content by fitting the intensity of the δ-hydride (111) diffracted peak relative to the (0002) hcp Zr peak when the diffraction vector is near the ND direction and $(10\bar{1}0)$ peak when near the TD direction [17].

The diffraction patterns obtained by rotating the point detector and the sample in the four-circle diffractometer were corrected with the Lorentz polarization factor. Then the diffraction patterns were fitted using PeakFit®. First the background was removed by using the best background fit, and then peaks were fitted using a Pearson VII profile function. In this peak shape both the full width at half maximum and the full width at tenth maximum can be varied. The integrated intensity, peak location and full width half-maximum were determined by this method.

Table 2-2 Summary of Zircaloy-2 samples studied at beamline 2-BM at the APS (sample orientation stands for which direction is coming out of the sample surface i.e. diffraction vector here)

Sample Orientation	Hydrogen contents (wt.ppm)	Load applied during thermal cycle
Normal	0	0
Normal	100	0
Normal	150	Tension 185MPa
Normal	660	0
Normal	660	Tension 185MPa
Transverse	0	0
Transverse	660	0
Transverse	660	Compression 185MPa

2.4.3. *Transmission In-Situ XRD Experiment at Beamline 1-ID at the APS*

Experiments at 1ID were conducted in transmission with a forward scattering geometry, illustrated in Figure 2-13(b). 80 keV x-rays (λ= 0.015 nm) were used and the beam was slit to 0.3mm^2 [55]. A high speed amorphous silicon GE area detector was used to study the kinetics of hydride dissolution/precipitation. This geometry allows the full diffraction rings to be recorded, which helps reveal in-plane texture. Since obtained in transmission, this data is averaged over the full sample thickness. The diffraction rings obtained are then integrated over the whole angular range to obtain average diffraction patterns or over sections of the angular range to investigate particular orientations. The samples were placed in a tensile device which can be operated under either displacement or force control. The MTS® frame used for applying stress to the samples allowed computer monitoring of the applied force, the displacement, or the displacement rate. The testing temperature was controlled using an optical furnace and the sample temperature was monitored using K-type thermocouples, spot welded onto the sample surface.

In this experiment the kinetics of hydride reorientation and precipitation in bulk samples were observed in-situ. Under temperature (up to 550°C) the hydrogen is dissolved to form a solid solution in the zirconium matrix and upon cooling down, the hydrogen precipitate as hydrides. Diffraction patterns are recorded continuously during these cycles. The evolution of the hydride peaks in terms of integrated intensity and peak shape gives us direct in-situ information on the kinetics of dissolution and precipitation and on the terminal solid solubility. By cycling several times the same sample at high temperature and back to room temperature, the ‘memory effect’ [56] of hydrides precipitating can be studied by comparing the diffraction patterns at room temperature for each cycle . The reorientation of the hydrides is also observed as a function of time by applying a constant load during cool-down. By observing the change in intensity and full width half maximum of the different hydride peaks, the hydride orientation can be determined,

and its kinetics calculated. The morphology and orientation of hydrides are determined as a function of stress, texture, cooling rates and texture. A summary of all samples ran at the 1-ID beamline and of the parameters used for these samples is presented in Table 2-3.

The typical raw data obtained during this experiment was ten two-dimension images from the plate detector for each diffraction pattern recorded (this was necessary to avoid saturation of the detector). The ten images were summed and averaged by a Matlab® routine developed by J. Almer [55] and the background was subtracted. Using the Matlab® routine, full diffraction rings were integrated over four specific banks or ±10º around 0º, 90º, 180º and 270º. The 'pizza-slices' obtained were then reduced to a one dimension GSAS file by the Matlab® routine. The GSAS peaks obtained were then analyzed using GSAS/Rawplot® [57]. This software program is primarily a Rietveld refinement program that can fit all the different parameters that would affect peak height, shape and position (these parameters can be sample characteristics such as composition, crystal structure, atom positions, etc. or exterior parameters such as sample to detector distance, temperature, pressure, etc). However GSAS also allows a faster refinement by only fitting the peak shape, position and intensity of the raw data in a sub routine called Rawplot. For our peak fitting, the precision and amount of information given by Rawplot were sufficient. The peaks are fitted to a pseudo-Voigt function which is a convolution of Gaussian and Lorentzian peak shapes, only the Gaussian full width half maximum was fitted while the Lorentzian full width half maximum remained constant; this Gaussian FWHM gives an understanding of what is the sample contribution to broadening. The background was modeled to a degree three polynomial function and several refinement steps were ran (usually 10 successive refinements for each parameter we chose to refine). This allowed us to fit the diffraction peaks and obtain (i) the integrated intensity, (ii) the Gaussian full width half maximum (FWHM), (iii) the peak positions for the desired peaks.

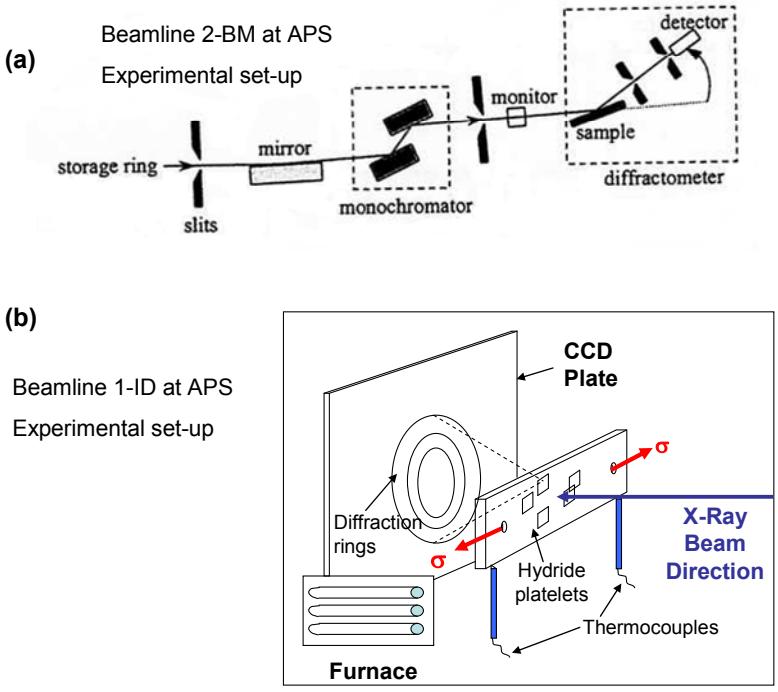

Figure 2-13 (a) Experimental set-up of beamline 2-BM at the Advanced photon source. (b): Experimental set-up of beamline 1-ID at the Advanced Photon Source

Table 2-3 Summary of samples ran at beamline 1-ID at the APS

Material	Sample orientation	Hydrogen contents (wt.ppm)	Heat Cycle	Load applied
Zircaloy-2	Normal	0	Up to 400°C and down	0
Zircaloy-2	Normal	150	Up to 400°C and down Different heat/cool rates	0
Zircaloy-2	Normal	100	Up to 400°C and down	50MPa-100MPa 150MPa
Zircaloy-2	Normal	600	Up to 550°C and down Different heat/cool rates	Run1: no load Run2: increasing load during cooling
Zircaloy-2	Normal	600	Up to 550°C and down Different heat/cool rates	0
Zircaloy-2	Normal	600	Up to 550°C and down (six cycles)	12.5MPa-25MPa 37.5MPa-50MPa 62.5MPa-75MPa
Zircaloy-2	Normal	600	Up to 550°C and down	Increasing load during cooling
Zircaloy-2	Normal	600	Up to 550°C and down	100MPa
Zircaloy-2	Normal	600	Up to 550°C and down	85MPa
Zircaloy-2	Transverse	0	Up to 400°C and down	0
Zircaloy-2	Transverse	150	Up to 400°C and down Different heat/cool rates	0
Zircaloy-2	Transverse	150	Up to 400°C and down	No load-40MPa 60MPa-80MPa 100MPa-120MPa
Zircaloy-2	Transverse	600	Up to 550°C and down	0
Zircaloy-4	Normal	600	Up to 550°C and down	75MPa
Zircaloy-4	Normal	600	Up to 550°C and down	85MPa
Zircaloy-4	Normal	600	Up to 550°C and down	100MPa
Zircaloy-4	Normal	1200	Up to 550°C and down	90MPa

2.4.4. *Micro-beam Crack-tip XRD Experiment at Beamline 2-IDD at the APS*

The 2-ID-D beamline is specialized in sub-micron high resolution X-ray studies. The X-rays are produced by the deceleration of the electrons present in the synchrotron as they pass through the insertion device of the beamline. For the 2-ID-D beamline, the insertion device that is used to produce the X-rays is an undulator. The X-rays are then focused using various optics such as Fresnel zone-plates for example. The experimental set-up for our experiment is presented in Figure 2-14. The detector for this experiment is a CCD camera. The beam was focused to 0.2 μm x 2 μm for our studies. More details on the 2-IDD beamline can be found in [58]. For our sample, the energy of the X-ray beam used was 10.1 keV which corresponds to a wavelength of 1.228 Å. As seen on Figure 2-14, the sample is a compact tension (CT) specimen of hydrided Zircaloy-2 with a crack grown by fatigue and hydrides precipitated at the tip of the crack. The tip of the crack was found by scanning the sample along x and y. Once the tip of the crack was found, the beam was set to scan first in the x direction, then in the y direction with a step size of 5 μm.

The two-dimensional images collected by the CCD camera were reduced to one-dimension diffraction patterns by a software from the 2-IDD beamline called CCD Sum. Then a Lorentz polarization correction factor was applied. Finally all the plots were assembled using Matlab®.

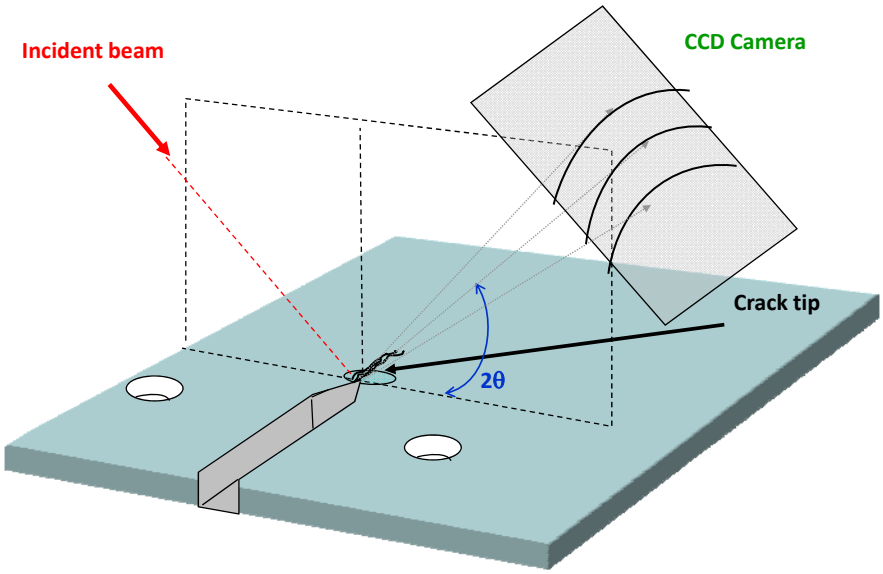

Figure 2-14 Experimental set-up of beamline 2-ID-D at the Advanced Photon Source

Chapter 3

RESULTS AND DISCUSSION

In this chapter, the results of metallographic and x-ray diffraction examination of hydrided zirconium alloy samples are presented and discussed. The first step in characterizing hydride behavior is to estimate the hydrogen content of our samples. This estimation is performed with three different techniques, presented in section 3.1. Since the hydrogen solubility limit is very low at room temperature, most of the hydrogen present in the samples precipitates as hydrides. It is important to fully describe the hydride orientation and morphology with respect to the alpha zirconium matrix and this is the subject of section 3.2. Once the hydride precipitates have been characterized, their dissolution and precipitation behavior during heat cycling is studied in section 3.3. In this section the kinetics of hydride dissolution and precipitation with no applied stress is determined using synchrotron x-ray diffraction. In section 3.4, the dissolution and precipitation of hydrides during heat cycling and under applied tensile stress is examined. In particular the reorientation from circumferential hydrides to radial hydrides is characterized in terms of threshold stress and morphology of reoriented hydrides. A “signature” for reoriented hydrides is identified for x-ray diffraction. In the last section of this chapter, a hydrided sample, with a previously existing crack and which has hydrides grown at its tip is studied using micro-beam synchrotron x-ray diffraction.

3.1. Estimation of Hydrogen Contents

3.1.1. *Hot Vacuum Extraction*

The first method to measure the hydrogen content is hot vacuum extraction (heating the sample to cause hydrogen to degas and measure pressure of the evolved hydrogen). The hot vacuum extraction was performed by Luvak Inc. (Boylston, MA) and serves as a reference 'true' value for the calibration of the metallography image analysis presented in the next section. The results given by hot vacuum extraction have a precision of ±5 wt.ppm. The results from hot vacuum extraction are presented in Table 3-1. One should note that variations in hydrogen content can occur from sample to sample and within one sample.

3.1.2. *Diffraction Intensity Ratio*

The second technique to estimate the local hydrogen content, the Direct Comparison Method, consists of taking the ratio of the diffracted peak intensities of the hydride δ(111) peak and the zirconium α(0002) peak [59]. This ratio can be related to the volume fraction of hydrogen V_δ / V_α by the following equation [17, 52]:

$$\frac{I_{\delta(111)}}{I_{\alpha(002)}} = \frac{R'_{\delta(111)} V_\delta}{R'_{\alpha(002)} V_\alpha} \qquad 3\text{-}1$$

where

$$R'_{X(hkl)} = \left(\frac{1}{\nu_X{}^2}\right)\left[\left|F_{X(hkl)}\right|^2 p_{X(hkl)} \left(\frac{1}{\sin^2\theta_{X(hkl)} \cos\theta_{X(hkl)}}\right)\right]\left(e^{-2M}\right)_{X(hkl)}$$

where ν_X is the volume of the unit cell (m^3), $\left|F_{X(hkl)}\right|^2$ is the structure factor for peak hkl, $p_{X(hkl)}$ is the multiplicity factor, $\theta_{X(hkl)}$ is the Bragg angle for the peak considered and $(e^{-2M})_{X(hkl)}$ is

the temperature factor, all for peak *hkl* of phase *X*. It should be noted that in the majority of the samples, δ hydrides were the predominant phase; therefore it was not necessary to take into account γ or ε hydrides to calculate the total hydrogen content. Figure 3-1 shows an example of the data used for this technique. The relative diffracted intensity acquired in reflection XRD at 15 keV is plotted versus two-theta angle for samples with three different hydrogen contents. The diffraction peaks identified are the α-zirconium matrix peak $(10\bar{1}0)$ and the δ-hydride (111) peak. For the sample with the highest hydrogen content the γ-hydride (111) peak can also be observed.

The intensity of the α-zirconium $(10\bar{1}0)$ peak is similar for the three samples; the small variations observed between samples are ascribed to grain sampling differences. The γ-hydride (111) peak intensity was accounted for, in the analysis of the sample with the highest hydrogen content. Those peaks were fitted as described in Section 2.4.2 and the integrated intensities were plugged into Equation 3-1, using the numerical values of the parameters shown in reference [17]. The results of these calculations are presented in Table 3-1.

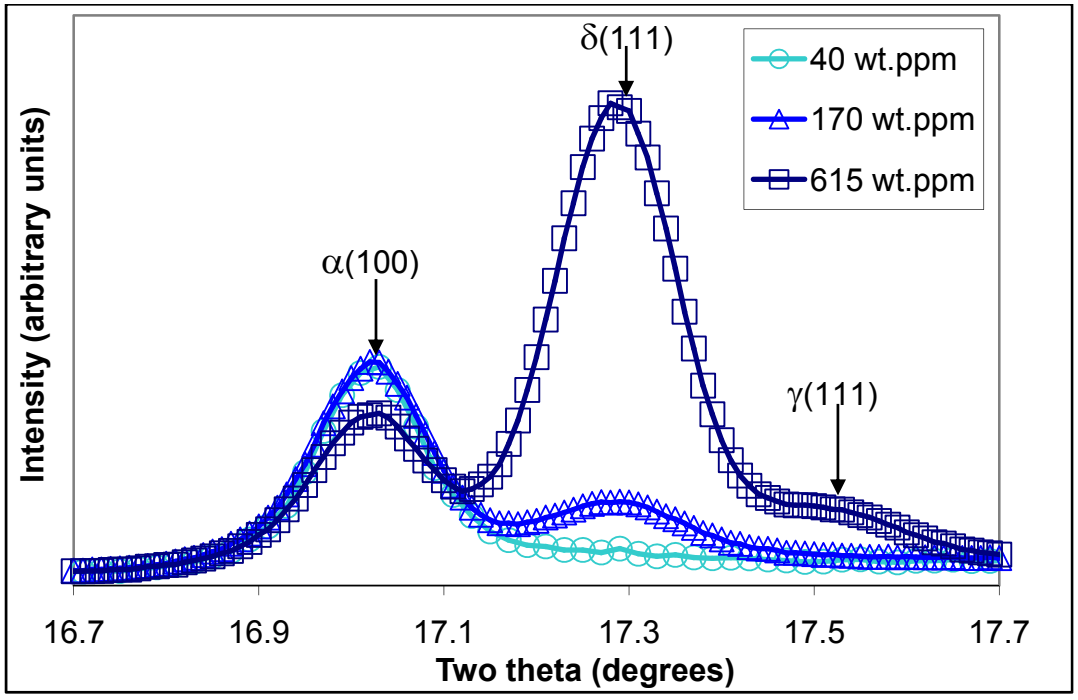

Figure 3-1 X-ray diffraction patterns of three Zircaloy-2 samples with hydrogen contents of 40 wt.ppm, 170 wt. ppm and 615 wt. ppm.

3.1.3. *Image Analysis*

The third method used to estimate local hydrogen contents was image analysis of the metallography pictures taken from samples that were chemically etched to reveal the hydrides, as described in section 2.3. The process of transforming an optical metallograph (Figure 3-2(a)) into a binary black and white picture is illustrated in Figure 3-2. Using the image analysis software ImageJ®, the greyscale optical metallographs were first transformed to black and white. Once the binary images are obtained, a relative area fraction of hydrides is calculated using ImageJ® [59, 60]. Because the area fraction changes with etching procedure and the calibration is dependent on the etching procedure, the hydrogen content is estimated from a calibration performed on a sample for which the hydrogen content was known from hot vacuum extraction. The equation used to relate the local hydrogen content $[H]_{total}$ with the hydride area fraction is [59, 60]:

$$[H]_{total} = [H]_{ZrH_x} . F_{ZrH_x} . \left[\frac{\rho_{ZrH_x}}{\rho_{\alpha-Zr} . (1 - F_{ZrH_x}) + \rho_{ZrH_x} . F_{ZrH_x}} \right] \quad 3\text{-}2$$

where $[H]_{total}$ is the local hydrogen content of the sample in wt.ppm, $[H]_{ZrHx}$ is the hydrogen content of the hydride phase of ZrH_x (for delta hydrides it is equal to 17 500 wt.ppm), ρ_{ZrHx} is the density of the hydride phase of ZrH_x at room temperature (5.646 g/cm^3), $\rho_{\alpha\text{-}Zr}$ is the density of the α-Zr phase at room temperature (6.51 g/cm^3) and F_{ZrHx} is the hydride area fraction (i.e. for the binary images the ratio of black pixels over white pixels). Using the calibration, the hydrogen contents of two samples was determined as shown in Table 3-1. Although hot vacuum extraction is more exact, with calibration this method can be used for hydrogen content determination, and it allows such determination to be done at a local level.

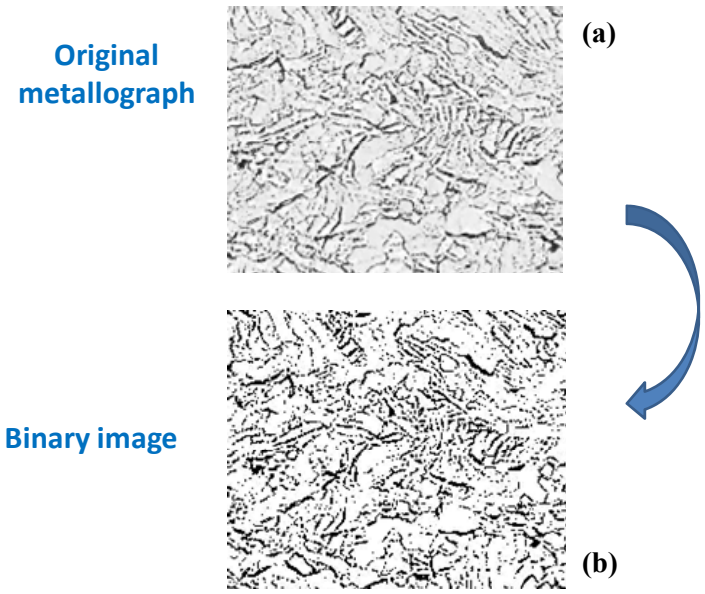

Figure 3-2 Illustration of transformation process of an optical metallograph (a) into a binary image (b); the hydride precipitates appear dark on a white zirconium matrix.

The three methods were applied to two Zircaloy-2 samples and the results are shown in Table 3-1. Considering the uncertainties and possible sources of error, the three methods are in good agreement and can be used to obtain a first-order estimate of the local hydrogen content in the sample.

Table 3-1 Comparison of three methods for estimation of hydrogen content of zirconium alloys

	Measured hydrogen contents (wt. ppm)		Reference hydrogen contents (wt. ppm)
	Diffraction Intensity Ratio	Image analysis	Hot vacuum Extraction
Zircaloy 2 Sample A	527	588	613
Zircaloy 2 Sample B	153	233	172

3.2. Relationship of Zirconium Matrix Texture with Hydride Orientation and Morphology

3.2.1. Hydride Orientation

In this section, the hydride precipitate orientation obtained after gaseous charging is studied using optical metallography and bulk x-ray diffraction. Figure 3-3 shows optical metallographs of Zircaloy-2 samples containing 610 wt.ppm hydrogen, and cut in two different directions. The hydride particles precipitate in platelets, mostly oriented with the platelet normal parallel to the sample normal direction (ND). This qualitative observation is confirmed by Hydromorph analysis. Hydromorph analysis (section 2.3) was performed on the metallographs shown in Figure 3-3 to determine the orientation of each hydride particle. These orientations are presented in Figure 3-4 as a function of hydride length. In Figure 3-4, the orientation angle is the angle between the habit plane of the hydride platelet and the horizontal direction of the figure. If the hydrides were perfectly oriented along the ND, the angles for the ND sample would all fall along the 0º line and the angles for the TD sample would fall along the 90º line as represented by the arrows in Figure 3-4. It is clear that the orientations of the hydride particles are closer to 0º in the ND sample than in the transverse direction sample. This is borne out by the calculated radial hydride content which is 24 % for the normal direction sample and 57 % for the transverse direction sample. We also see a greater degree of scatter in the orientation of the hydrides in the transverse direction sample than in the normal direction sample.

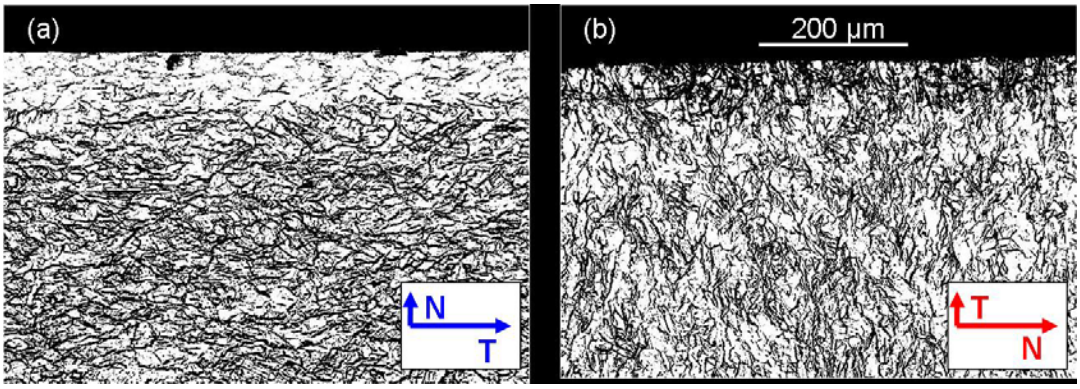

Figure 3-3 (a) Metallography of Zircaloy-2 sample with 610 wt. ppm hydrogen content and the normal direction coming out of the sample surface; (b) Metallography of Zircaloy-2 sample with 610 wt. ppm hydrogen content and the transverse direction coming out of the sample surface.

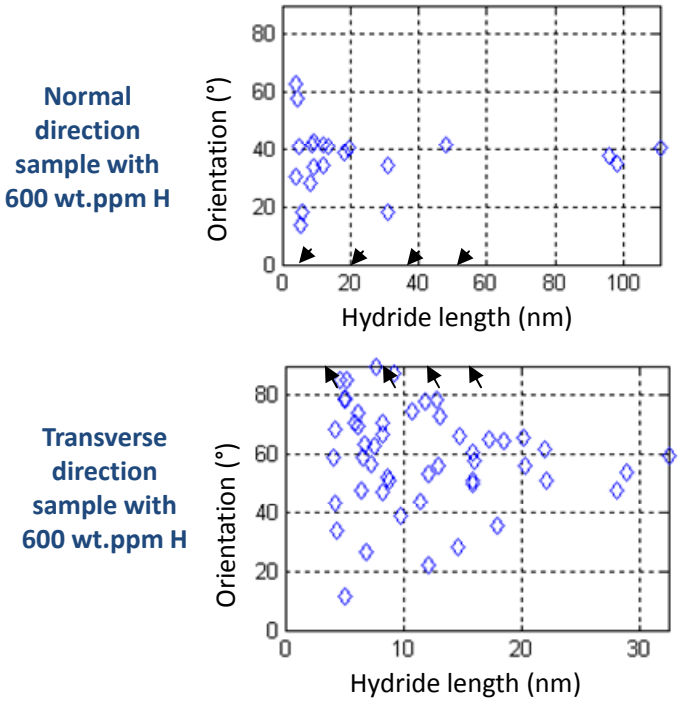

Figure 3-4 Hydride orientation as a function of hydride length for two Zircaloy-2 samples with 610 wt.ppm of hydrogen with different orientations.

Figure 3-5 presents a bulk x-ray diffraction pattern of the same two samples studied in Figure 3-3 and Figure 3-4 acquired using synchrotron radiation. The α-zirconium peaks intensities are in agreement with the measured texture: the $(0002)_\alpha$ peaks are much stronger for the ND sample than for the TD sample and the inverse behavior is observed for the $(10\bar{1}0)_\alpha$ and $(10\bar{1}1)_\alpha$ peaks. The behavior of the $(111)_\delta$ hydride peaks is stronger for the ND sample than for

the TD sample, in qualitative agreement with an orientation relationship where $(111)_\delta$ // $(0002)_\alpha$ (the hydride peaks do not diminish as much as the zirconium peaks when changing the orientation because of the multiplicity of the FCC (111) hydride peaks is higher than for the zirconium HCP (0002) peaks). The $(200)_\delta$ peaks are stronger for the TD sample than for the ND sample, which is consistent with this orientation relationship as well.

In summary we have seen that the macroscopic hydride platelets are oriented with their normal parallel to the ND and that observations are consistent with the $(111)_\delta$ // $(0002)_\alpha$ orientation relationship found in the literature.

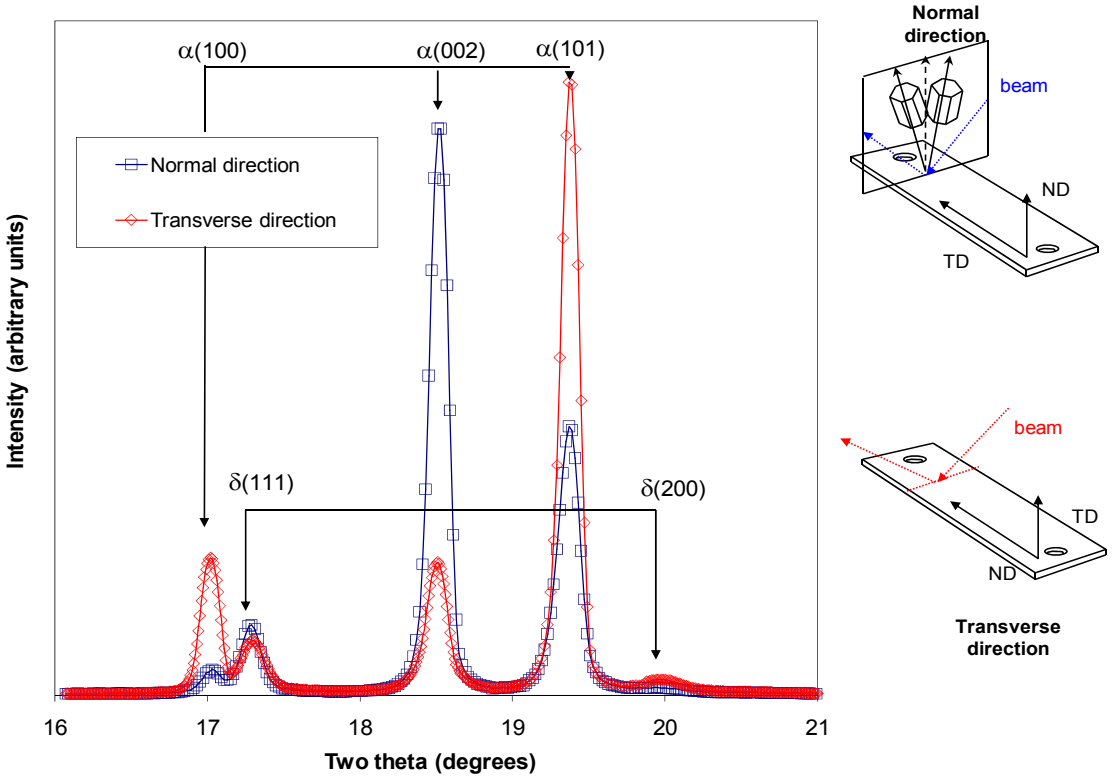

Figure 3-5 X-ray diffraction patterns of two Zircaloy-2 samples with different microstructural orientation.

3.2.2. *Hydride Morphology*

In this section the hydride platelet morphology is investigated using transmission x-ray diffraction. The three sample orientations studied in this section are illustrated in Figure 3-6, in each case with a different surface normal. The RD sample is in reality a dog-bone sample with a square cross-section (2 x 2 mm^2), thus allowing equal x-ray penetration in each direction.

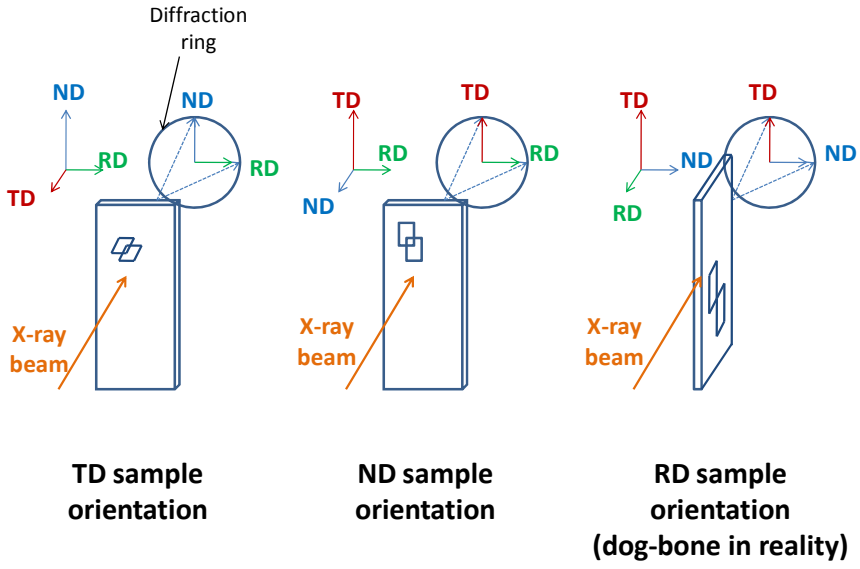

Figure 3-6 Schematic representation of the three sample and hydride orientations studied in this section

The diffraction rings detected by the plate detector are integrated ± 10º around particular directions (such as ND and RD for a TD sample for example), these different integrations are called integration 'banks'. In Figure 3-7, the diffraction patterns for the two integration banks of the RD sample (TD and ND) are presented. The $(111)_\delta$ peak in the ND bank is much broader than the same peak in the TD bank. The relative intensities of the (100) zirconium peak are consistent with the expected matrix texture, i.e. the (100) peak is much higher in the TD than in the ND. In the diffraction pattern for the ND sample presented in Figure 3-8, both integration banks of the $(111)_\delta$ peak have the same shape, which is also similar to that of the TD bank of the RD sample

studied in Figure 3-7. The comparison of the two integration banks for the TD sample presented in Figure 3-9 was expected to confirm the platelet shape. However both banks of the $(111)_\delta$ peaks have a similar peak shape and have a higher integrated intensity that the similar banks observed in the RD and the ND sample. The higher integrated intensity could be due to a higher hydrogen content of the TD sample compared to that of the RD and ND samples but this hypothesis is ruled out by Figure 3-10 which shows the integrated intensity of the TD sample and the RD sample over the full diffraction ring. Both $(111)_\delta$ peaks have a similar intensity which suggests that they have similar hydrogen contents. Another hypothesis that can explain the higher integrated intensity and the similar peak shape of the $(111)_\delta$ peaks of the TD sample is the greater scatter in hydride orientation in this sample as compared to the TD sample, as was pointed out by Figure 3-4. This means that for the TD sample the scatter in hydride orientation causes the intensity of the $(111)_\delta$ peaks to come from hydrides oriented as in Figure 3-6 and others perpendicular to it, making it difficult to ascertain hydride orientation.

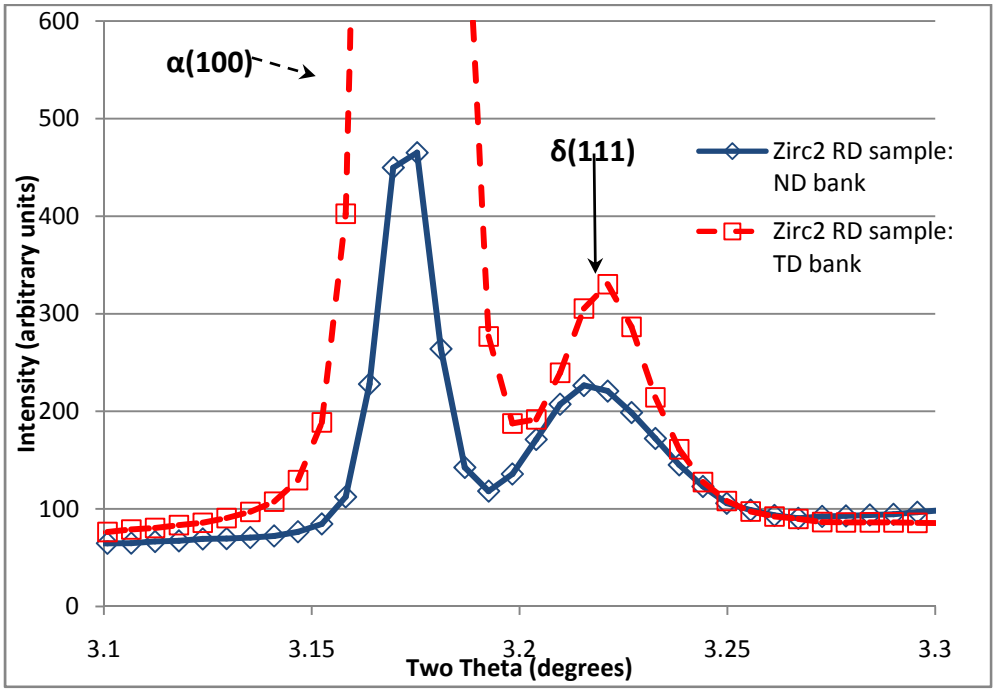

Figure 3-7 X-ray diffraction pattern of the two integration banks of the Zircaloy-2 RD sample with 600 wt.ppm.

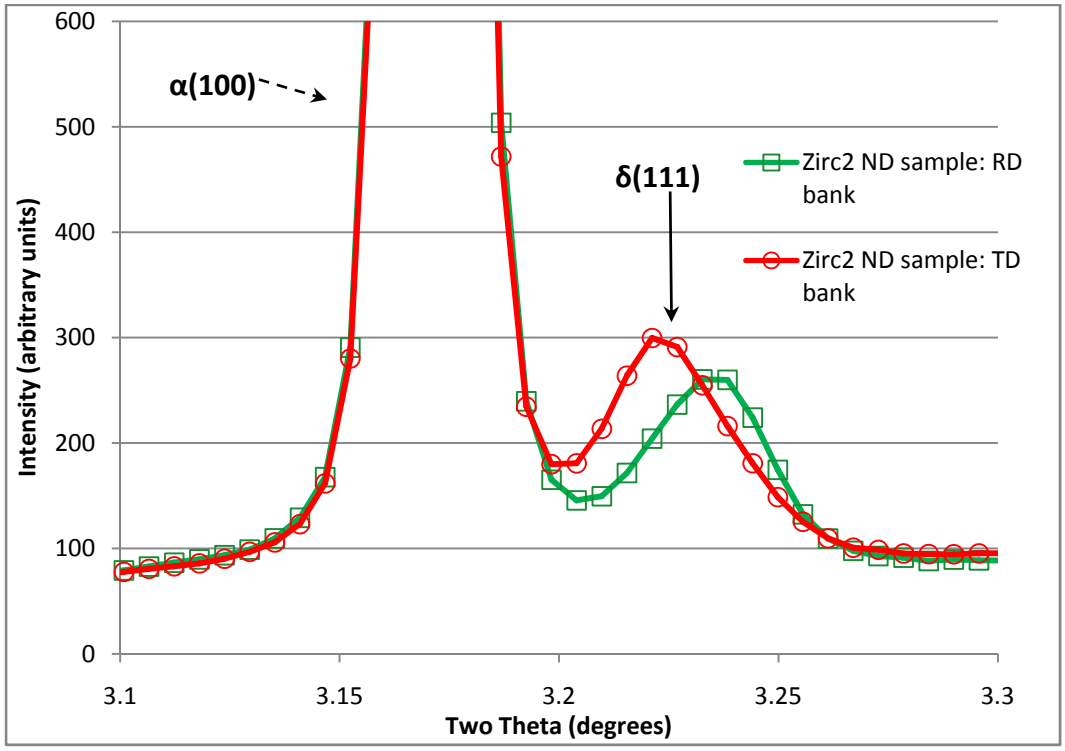

Figure 3-8 X-ray diffraction pattern of the two integration banks of the Zircaloy-2 ND sample with 600 wt.ppm

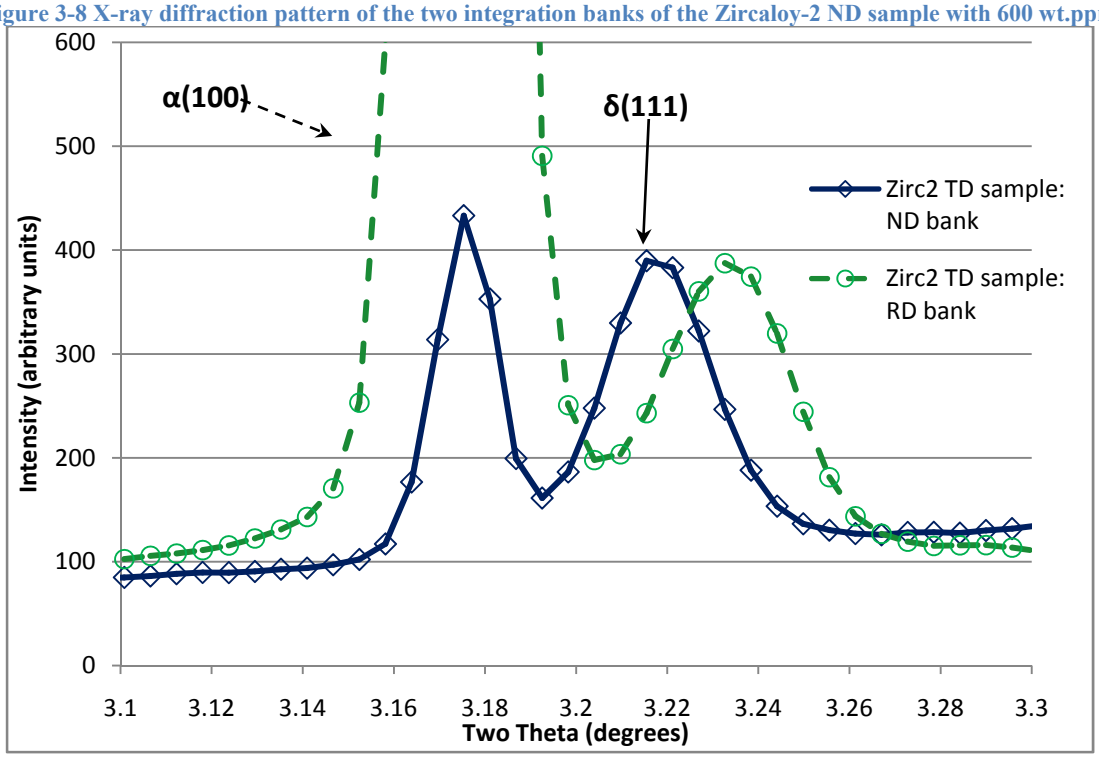

Figure 3-9 X-ray diffraction pattern of the two integration banks of the Zircaloy-2 TD sample with 600 wt.ppm.

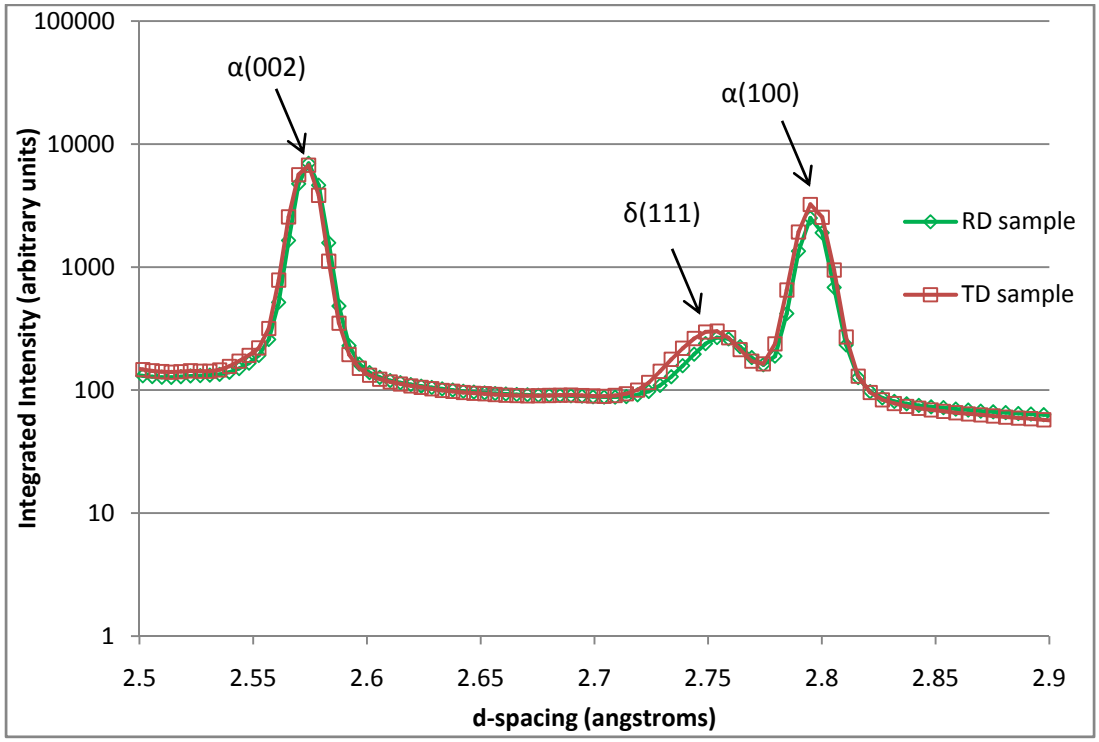

Figure 3-10 X-ray diffraction pattern (logarithmic scale) of the overall integrated intensity of the RD Zircaloy-2 and the TD Zircaloy-2 sample both with 600 wt.ppm.

Another feature observed in Figure 3-7, Figure 3-8 and Figure 3-9 is the peak shift for the RD bank of the $(111)_\delta$ peak compared to the other integration banks (the alpha zirconium peaks correspond well with the expected PDF values reported in Table 2-1). The peak location for the $(111)_\delta$ peak in the RD bank of both samples is 3.233º, while that for the TD bank it is 3.221º and for the ND bank it is 3.215º. This is to be compared to the PDF value at 80 keV of 3.218º. The TD and ND banks are very close to the expected PDF value, although the ND bank has a slightly lower peak position than expected. This suggests that these planes are under a small amount of tension. The TD bank has a slightly higher peak location than the PDF, which suggests a small amount of compression. The RD bank has a higher peak position than the PDF which means a smaller d-spacing. The RD bank is therefore likely in compression. First order calculations show a stress slightly above the yield stress:

$$\sigma = E\,\varepsilon = 140 \times 4 \times 10^{-3} = 560 \text{ MPa}$$

where E is the elastic constant for hydrides (140 GPa), ε is the strain measured from the shift in d-spacing ($\varepsilon \sim (3.233\text{-}3.218)/3.218 \sim 4 \times 10^{-3}$) . The yield stress for hydrided Zircaloy-2 is about 480 MPa at room temperature. This implies that any stress above the yield stress will be accommodated with plastic deformation such as dislocations leaving a resulting stress on the hydrides of about the yield stress.

This compression of the RD bank is likely related to the fact that the hydrides have a lower density (higher volume) than the matrix. There are anisotropic strains applied to the hydrides as they precipitate. The data would suggest greater compression in the RD, but no reason is apparent for this.

In this section, it was confirmed that the TD and RD bank had a similar peak shape as the ND and TD sample whereas the ND bank was broader. This is linked to the hydride platelet shape that induces different strain or size broadening for hydride peaks in the ND. The TD sample had hydrides that were too scattered in orientation to confirm the platelet shape. Finally the hydride $(111)_\delta$ planes in the RD direction were determined to be more in compression in the alpha zirconium matrix than the other two banks.

3.3. Kinetics of Dissolution and Precipitation of Hydrides without Load

3.3.1. Study of Parameters Influencing the Dissolution and Precipitation Temperatures of Hydrogen in Zirconium

In this section, the dissolution and precipitation of hydrides is studied by transmission x-ray diffraction. Figure 3-11 shows the integrated intensity of the RD bank of the hydride $(111)_\delta$ peaks as a function of time and temperature for two Zircaloy-2 samples with different hydrogen contents. As shown by the temperature curve, the samples were first heated up to a temperature sufficient to completely dissolve the hydrides, and then cooled allowing the hydrides to re-precipitate. The intensities of the $(111)_\delta$ peaks return to their initial value after cooling down, indicating the same amount of hydrides that were initially present have re-precipitated upon cooling.

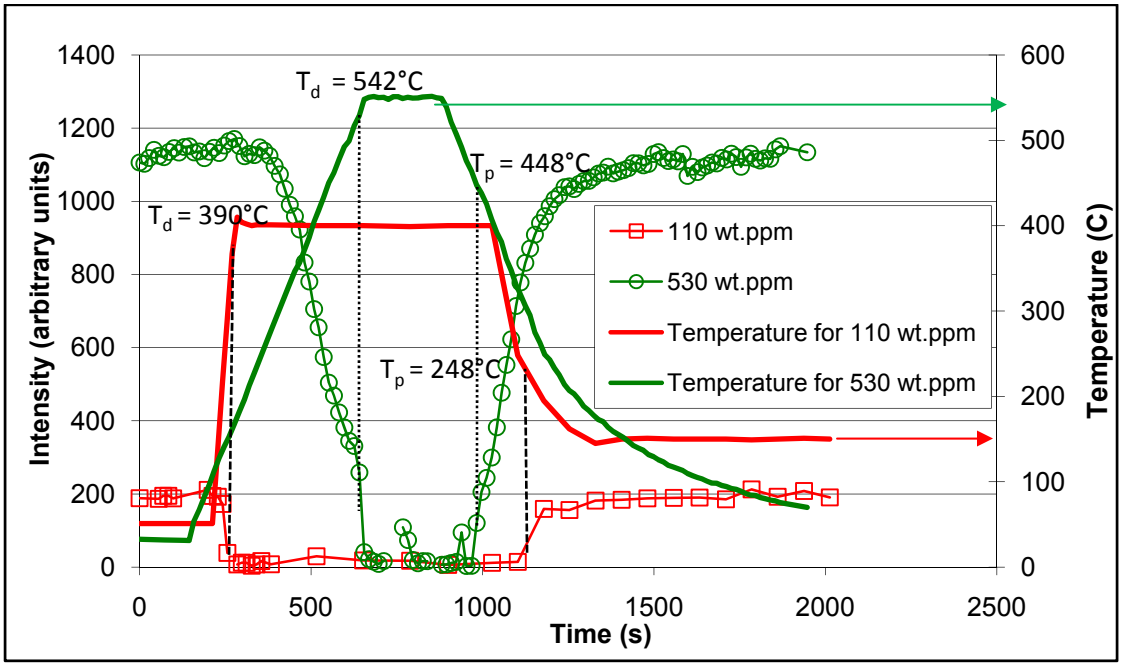

Figure 3-11 Evolution of the integrated intensity of delta(111) hydride peaks RD bank with temperature for two Zircaloy-2 ND samples with 110 wt.ppm and 530 wt.ppm of hydrogen.

The dissolution temperature, T_d, is defined as the temperature at which the hydride peak intensity is 10 % of its initial plateau value during heating. The precipitation temperature, T_p, is defined as the temperature at which the hydride peak intensity is 10 % of its initial value during cool down. The T_d and T_p have been estimated for Figure 3-11 and are compared to the expected temperature at the terminal solid solubility in Table 3-2. In Table 3-2, the T_d and T_p from several samples including those from Figure 3-12 are also shown. No significant difference is seen between the two banks for a given sample. The T_d and T_p presented in Table 3-2 are in good agreement with the temperatures at the TSSd and the TSSp for the three first samples. This shows that the T_d and T_p can be accurately determined by examining the diffraction pattern signal for the $(111)_\delta$ peaks. One should also note that the dissolution rate (as measured by the diffracted intensity) increases towards the end of the dissolution process, likely because the precipitates are already significantly smaller, thus having a larger surface to volume ratio, which results in a faster dissolution rate towards the end of the dissolution process.

For the fourth sample shown in Table 3-2 (data shown in Figure 3-11 and Figure 3-12), there is less agreement between the T_d and temperature at TSSd and the T_p and the temperature at TSSp. One should note that the heating and cooling rates are higher than for the first three samples, which renders the comparison of the T_d and T_p with the TSSd and TSSp more difficult, since the sample is further away from thermodynamic equilibrium.

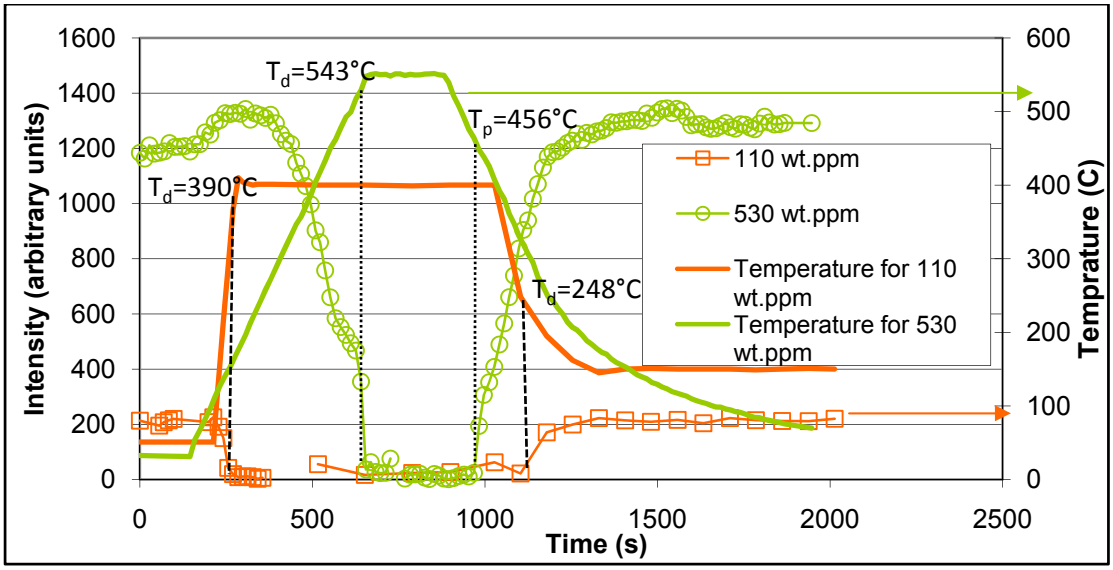

Figure 3-12 Evolution of the integrated intensity of delta(111) hydride peaks TD bank with temperature for two Zircaloy-2 ND samples with 110 wt.ppm and 530 wt.ppm of hydrogen.

Table 3-2 Comparison of Td and Tp estimated from the diffraction graphs to the predicted temperatures[8]; the rates are for both heating and cooling.

		Estimated T_d (°C)	Predicted Temperature at TSSd (°C)	Estimated T_p (°C)	Predicted Temperature at TSSp (°C)
Zircaloy-2 ND 80wt.ppm (0.05°C/sec)	delta(111) RD bank	310	320 ± 10	285	280 ± 10
	delta(111) TD bank	312	320 ± 10	276	280 ± 10
Zircaloy-2 ND 530wt.ppm (1°C/sec)	delta(111) RD bank	542	540 ± 10	448	460 ± 10
	delta(111) TD bank	543	540 ± 10	456	460 ± 10
Zircaloy-2 TD 530wt.ppm (1°C/sec)	delta(111) RD bank	498	510 ± 10	428	440 ± 10
	delta(111) ND bank	500	510 ± 10	430	440 ± 10
Zircaloy-2 ND 110wt.ppm (5°C/sec)	delta(111) RD bank	390	340 ± 10	248	290 ± 10
	delta(111) TD bank	390	340 ± 10	248	290 ± 10

The effect of heating and cooling rate on the T_d and T_p is shown in Figure 3-13 for a Zircaloy-2 sample with 80 wt.ppm hydrogen. The expected temperature for this hydrogen content for dissolution (heating) is 320ºC and the expected temperature for precipitation is 280ºC. At slow cooling rates (below 0.2ºC/s) the T_d and T_p are close to the expected values. For faster cooling rates however, T_d is higher than the expected value and T_p is lower than the expected value. This is because for non-equilibrium situations, the samples require higher temperatures or longer times at temperature to dissolve and lower temperatures or longer time at temperature to precipitate.

In summary, we have shown that the T_d and T_p can be determined fairly accurately by observing the diffracted intensity of the $(111)_\delta$ hydride peaks. This determination agreed with the expected values for slower heating/cooling rates. For faster cooling and heating rates, the T_d and T_p were respectively higher and lower than the expected values because the samples are farther away from thermodynamic equilibrium during the thermo-mechanical treatment.

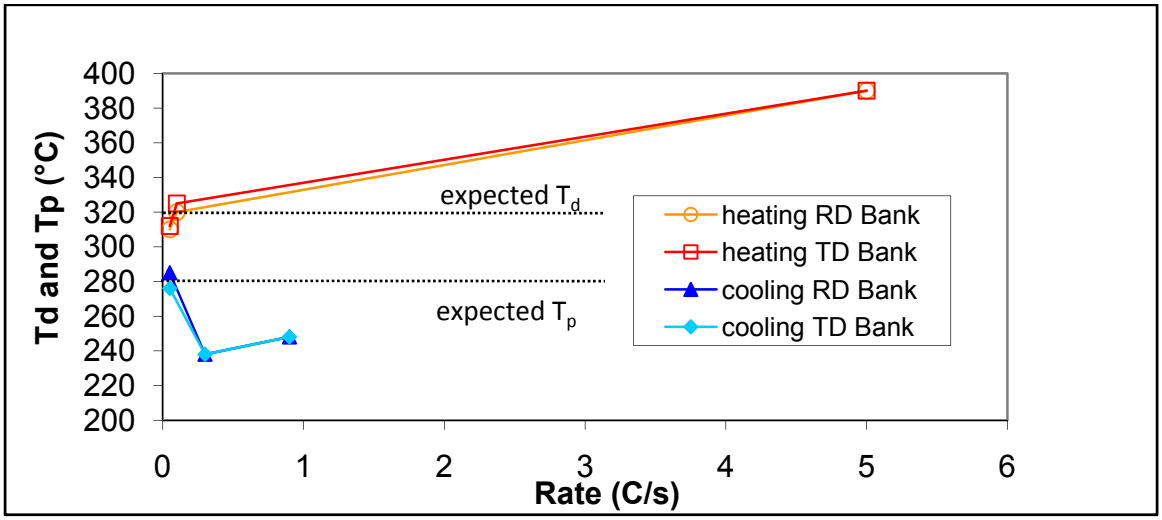

Figure 3-13 Precipitation and dissolution temperatures as a function of heating and cooling rates for a Zircaloy-2 ND sample with 80 wt.ppm of hydrogen.

3.3.2. Study of the effect of cooling rates on hydride size

In this section, the effect of cooling rates on the macroscopic hydride size has been studied using image analysis and transmission x-ray diffraction. Firstly, we compare the metallographs of samples that were slow-cooled in a vacuum furnace to those of the same samples cooled at fast rates (around 1ºC/sec). The hydride size analysis is performed using Hydromorph®. As explained in section 2.3, the hydride length calculated by Hydromorph® is the distance between the two farthest points of the hydride particle. The results of the analysis of several samples are presented in Table 3-3 in which the mean hydride length averaged over all particles analyzed is presented in microns. For all samples analyzed, the average hydride length is smaller after fast cooling than after slow cooling. This is consistent with the increase of hydride size with increasing cooling rates found in the literature.

Table 3-3 Mean hydride length calculated by Hydromorph® for several samples at different cooling rates

	Mean hydride length after slow vacuum cooling in furnace before APS (µm)	Mean hydride length after fast air cooling at APS (µm)
Sample 1	9.2	7.0
Sample 2	13	11
Sample 3	10	7.0
Sample 4	10	8.7

In Figure 3-14, the Gaussian full width at half maximum, noted FWHM, calculated by peak fitting with GSAS (GSAS is the General Structure Analysis System which is a peak fitting software described in section 2.4.3) is plotted for two samples as a function of cooling rate. For each sample, the FWHM values do not change significantly with cooling rate. This means that the effect of size broadening cannot be observed for samples with similar cooling rates, since a change in FWHM would imply a change in size broadening.

In this section, image analysis showed that for faster cooling rates the hydride particles are smaller as would be expected. This could not be revealed by x-ray diffraction by comparing the peak broadening of hydride peaks for different cooling rates.

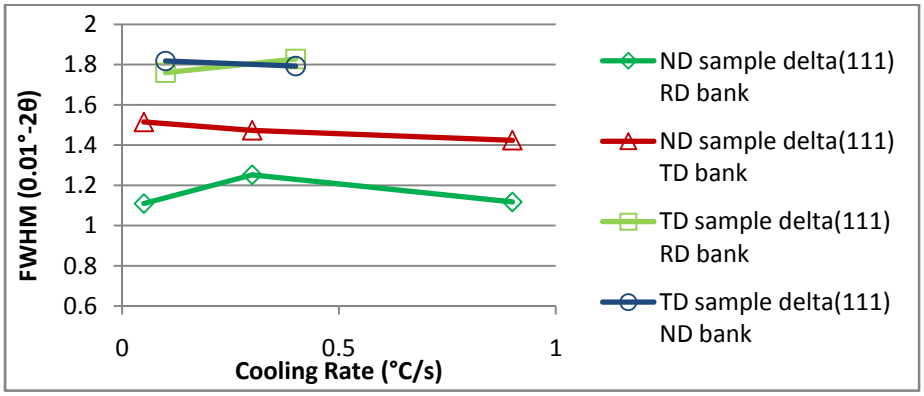

Figure 3-14 Gaussian broadening of the delta(111) hydride peak for two Zircaloy-2 samples with 100 wt. ppm cooled under different rates

3.3.3. *Morphology of precipitating hydrides*

In this section, the study of the morphology of hydrides as they precipitate under no applied load is performed using transmission x-ray diffraction. The hydride peaks found in the different integrated orientations (or banks) are analyzed using GSAS. This analysis process yields the instrumental broadening, peak intensity, peak location and Gaussian full width at half maximum (FWHM). In particular, the Gaussian FWHM is studied for several hydride peaks for a Zircaloy-2 sample hydrided at 510 wt.ppm. In Figure 3-16, Figure 3-17, Figure 3-18, Figure 3-19 and Figure 3-20, we plot ($FWHM_{Sample}$ x cos θ) versus (sin θ) for different points along the heating and cooling of the sample represented in Figure 3-15 (the fits from which the values for FWHM are extracted for a few hydride peaks are presented in Figure 3-21 and Figure 3-22). This type of plot allows us to distinguish size from strain broadening since:

$$FWHM_{Sample} \propto \varepsilon_{lattice} \frac{sin\theta}{\cos\theta} \quad \text{strain broadening} \qquad 3\text{-}3$$

$$FWHM_{Sample} \propto \frac{0.9\,\lambda}{t\cos\theta} \quad \text{size broadening} \qquad 3\text{-}4$$

where $FWHM_{Sample}$ is the measured Gaussian FWHM minus the instrumental broadening (in radians 2θ), θ is the Bragg angle (in radians), $\varepsilon_{lattice}$ is the lattice strain, t is the sample particle size (in nm) and λ is the x-ray beam wavelength (in nm). Therefore the slope of the curves plotted in Figure 3-16, Figure 3-17, Figure 3-18, Figure 3-19 and Figure 3-20 is proportional to strain and the y-intercept is proportional to the amount of size broadening.

Figure 3-17, Figure 3-18 and Figure 3-19 were taken at different times as the hydrides precipitate (decreasing temperature); these precise times are indicated in Figure 3-15. It is seen that for all times, the size broadening is negligible since the fitted lines cut the ordinate axis at about 0 (by extrapolation of the fitted lines to the ordinate axis). This is likely because, when detected the particles must be at a size that does not give rise to significant size broadening. This

confirms that size broadening for hydrides precipitates is very difficult to observe with our x-ray diffraction techniques.

Also the slope of the RD bank of the curves at t=1027s is lower than the one for t=1070s which is in turn lower than the one at t=1090s (Figure 3-16 to Figure 3-18). This implies that, for smaller hydride precipitates (t=1027s), the strain is smaller. As temperature decreases (and hydrides grow) the slope of the curve increases which implies an increasing strain on the hydrides. This might be due to the thermal expansion mismatch between the hydrides and the alpha zirconium matrix: as the temperature decreases, the hydrides contract faster than the matrix, (the thermal expansion coefficients are $\alpha_{Zr} = 6x10^{-6}$ per ºC and $\alpha_{Hydride} = 14.2x10^{-6}$ per ºC [27]) thus implying a higher strain on the precipitates.

When comparing the final state (Figure 3-20) to the initial state (Figure 3-16), it is seen that the broadening is similar for both states, and consists mostly of strain broadening with little size broadening. This implies that the strain caused by volume expansion of hydrides upon precipitation was not affected by one thermal cycle and that size broadening is not seen in the RD or TD directions when comparing the initial and final states.

In this section, we have seen that hydrides precipitation is associated with strain. This strain is likely a combination of elastic and plastic strains, caused by both size mismatch and differential thermal expansion. It was also observed that after full precipitation, the hydrides exhibit the same broadening, and thus the same strain as initially.

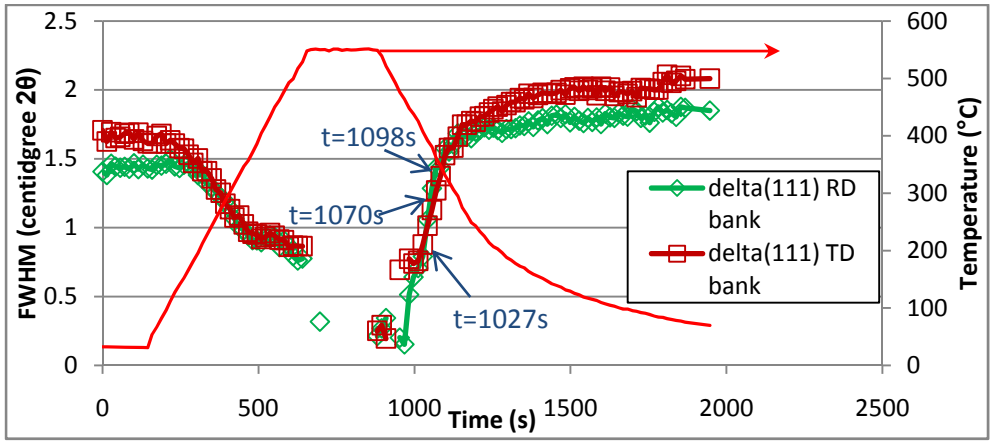

Figure 3-15 Time evolution of the FWHM Gaussian broadening of the delta(111) peaks of a Zircaloy-2 sample with 510 wt.ppm of hydrogen heated and cooled under no load.

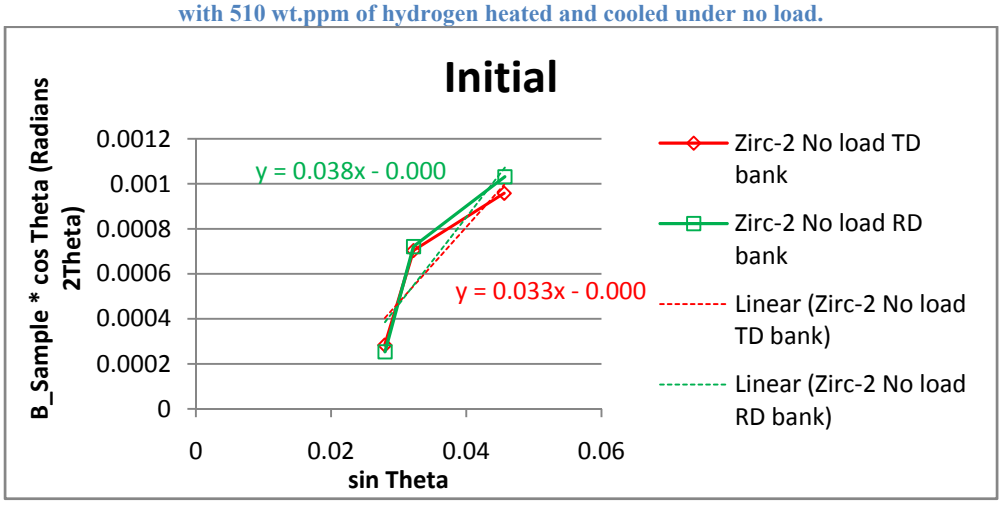

Figure 3-16 Study of size and strain broadening for a Zircaloy-2 sample with 510 wt.ppm at time t=0s.

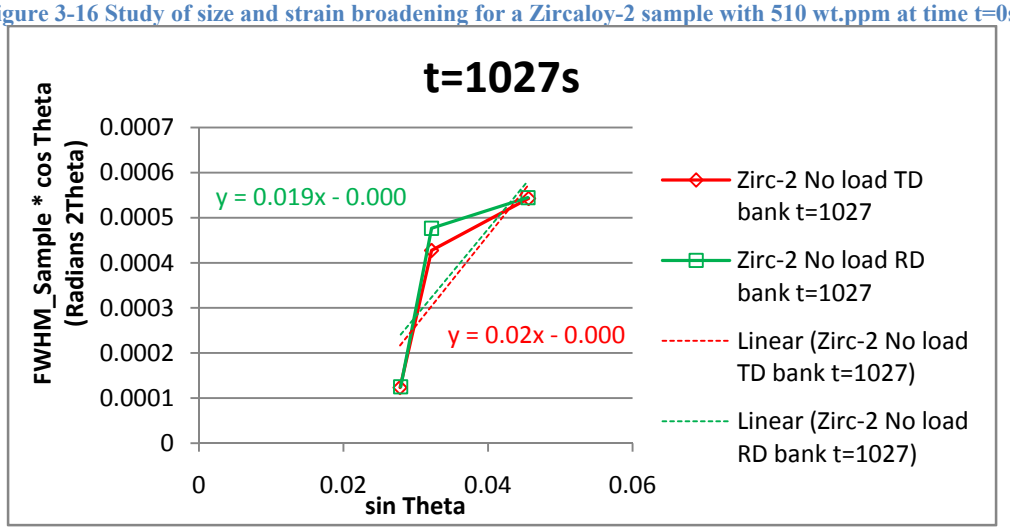

Figure 3-17 Study of size and strain broadening for a Zircaloy-2 sample with 510 wt.ppm at time t=1027s.

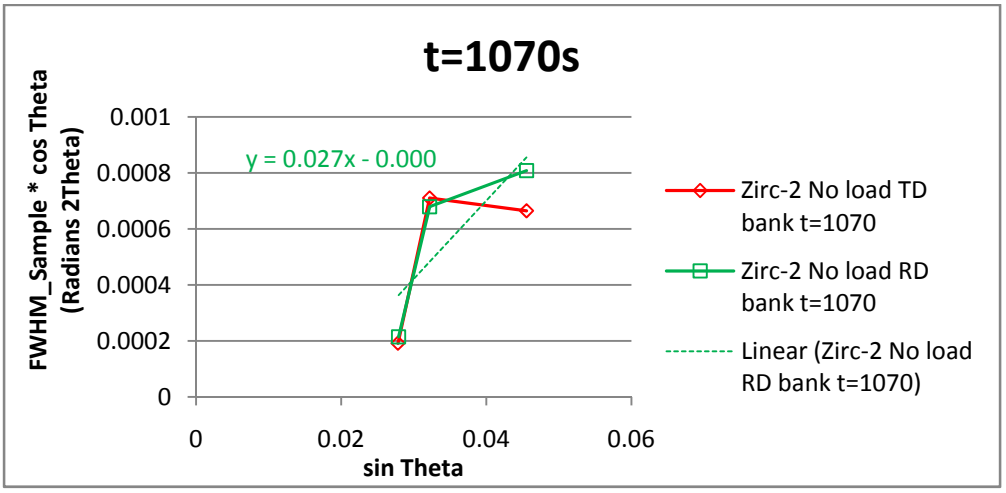

Figure 3-18 Study of size and strain broadening for a Zircaloy-2 sample with 510 wt.ppm at time t=1070s.

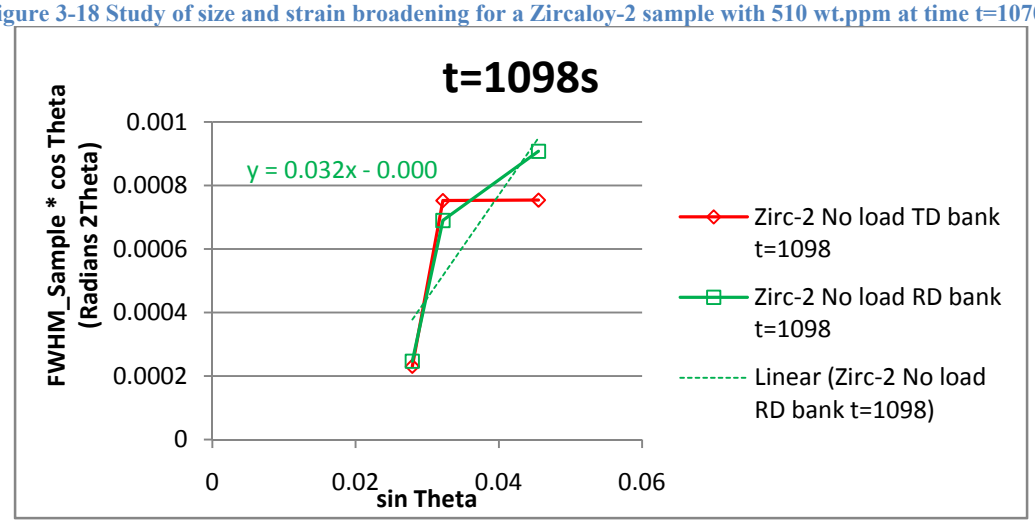

Figure 3-19 Study of size and strain broadening for a Zircaloy-2 sample with 510 wt.ppm at time t=1098s.

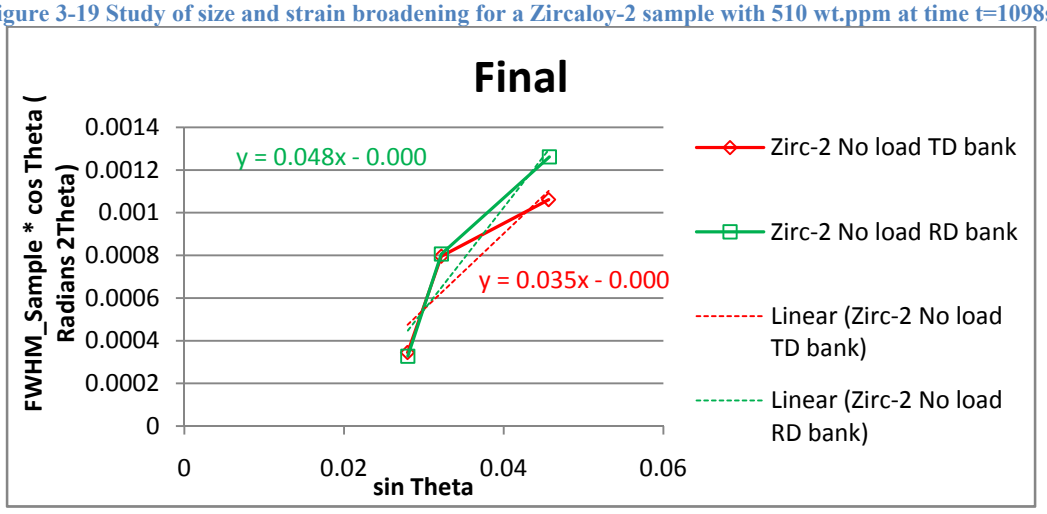

Figure 3-20 Study of size and strain broadening for a Zircaloy-2 sample with 510 wt.ppm at the final time.

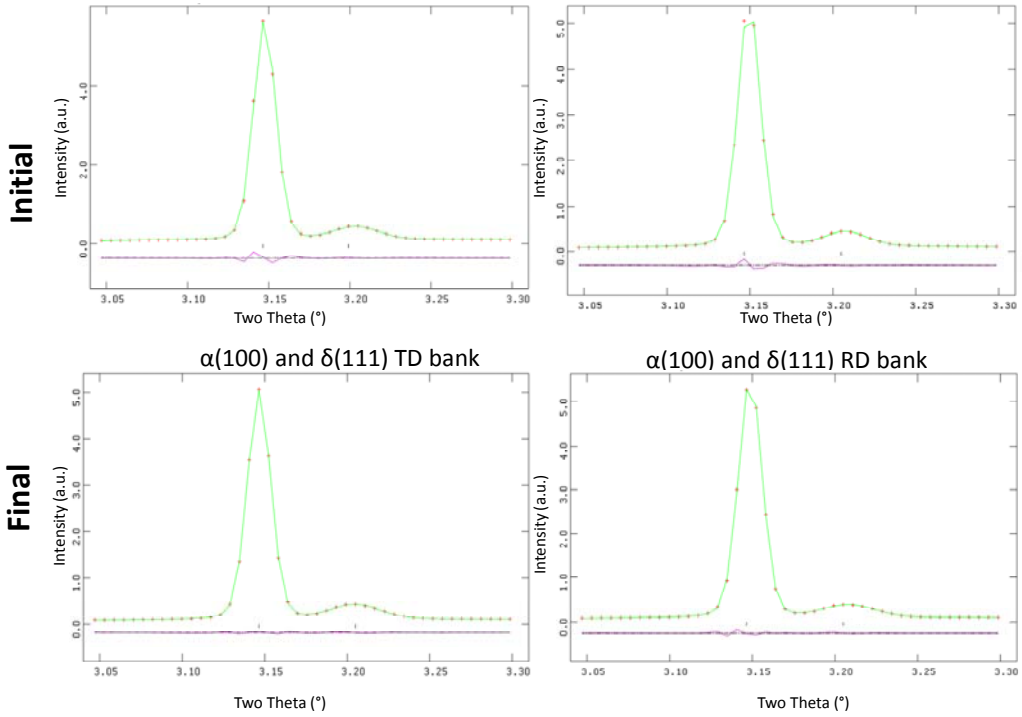

Figure 3-21 Fits of the delta(111) peaks for a Zircaloy-2 sample with 510 wt.ppm before and after heat cycle, obtained using GSAS.

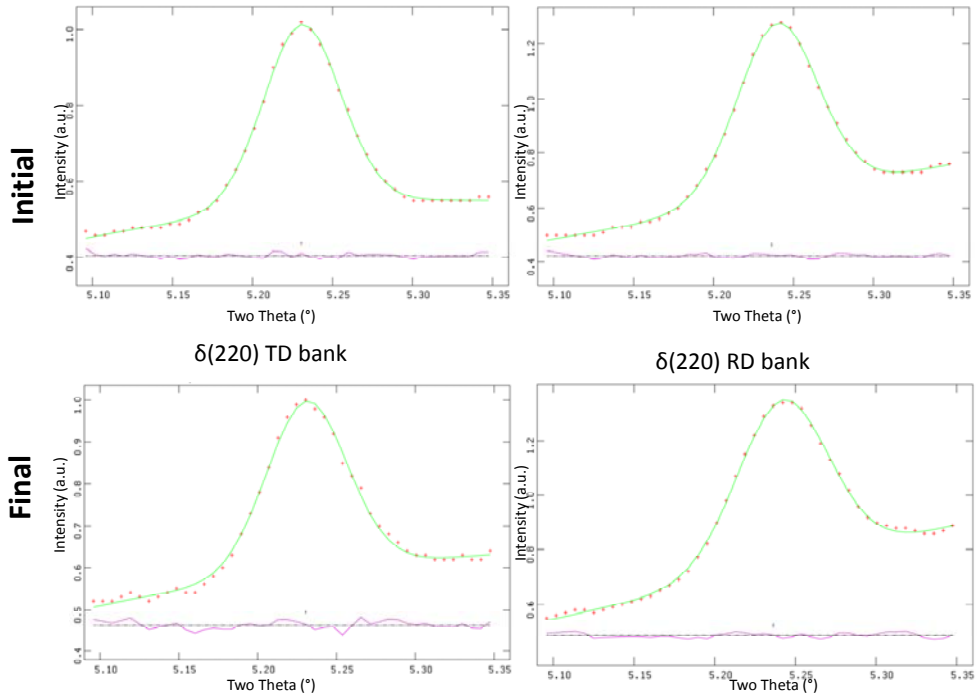

Figure 3-22 Fits of the delta(220) peaks for a Zircaloy-2 sample with 510 wt.ppm before and after heat cycle, obtained using GSAS.

3.4. Kinetics of Dissolution and Precipitation of Hydrides under Load

3.4.1. Estimation of Threshold Stress for Reorientation

In this section, the evolution of the hydride precipitates orientation with applied tensile stress during cool down is investigated. Metallography performed before and after a heating under no stress and cooling cycle under tensile stress allows the observation of hydride precipitate reorientation. Figure 3-23(a) shows a micrograph of a Zircaloy-2 sample containing 605 wt. ppm of hydrogen, and which exhibits similar texture and hydride orientation as the sample shown in Figure 3-3(a).

This sample was heated to 550°C and then cooled down under an applied tensile stress of 75MPa (note that this is the engineering stress, calculated by dividing the force in Newtons by the initial cross-sectional area of the sample in the direction indicated). The zirconium hydrides appear to have re-precipitated in an orientation similar to that present before the experiment. In contrast, when the same experiment was performed under an applied stress of 85MPa, the final hydride microstructure (Figure 3-23 (d)) was found to be significantly different from the initial one (Figure 3-23(c)). In the initial stage the hydrides are all oriented parallel to the sample surface, while, after heating and cooling under load, a significant fraction of hydrides precipitate with their platelet normal aligned with the load axis.

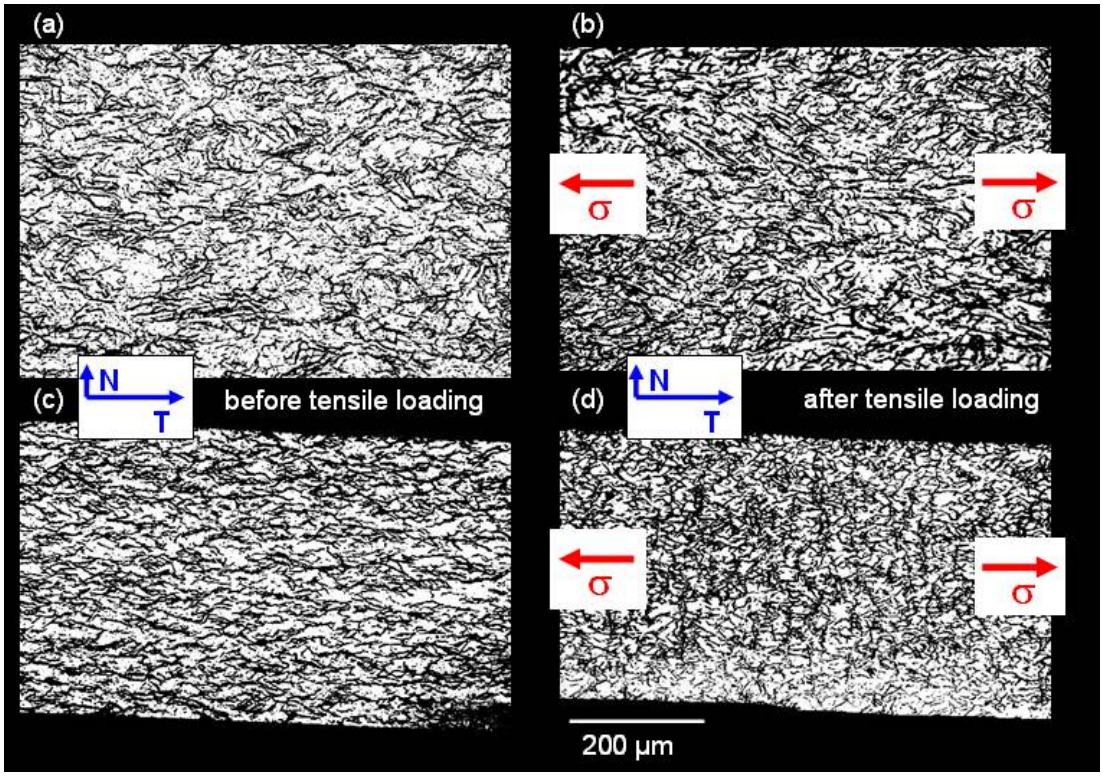

Figure 3-23 Optical metallography of hydride orientation before and after cooling under load (a) Zircaloy-2 sample with 605 wt.ppm of hydrogen; (b) Same sample after being heated up to 500°C then cooled down with an applied tensile stress of 75 MPa; (c) Zircaloy-4 sample with 608 wt.ppm of hydrogen; (d) Same sample after being heated up to 500°C then cooled down with an applied tensile stress of 85 MPa.

Figure 3-24 shows optical metallographs of a Zircaloy-4 dog-bone sample with 608 wt. ppm of hydrogen. This sample was heated to 550°C then cooled under an applied tensile stress of 100 MPa (calculated in the gage section of the dog-bone specimen). The sample was cut along its length and different pictures were taken at different locations along the dog-bone shaped sample. Figures 3-24 (a) and (d) were taken at the thick end of the sample (where the applied stress is much lower than 100 MPa because of larger cross-sectional area), whereas Figures 3-24 (b) and (c) were taken in the gage section in which the stress is close to 100 MPa. In the metallographs taken in the gage section, many hydrides have reoriented (indicated by red arrows) with the platelet normal now aligned with the load axis, while in the thick ends of the dog-bone shaped sample, the hydride orientation has remained the same.

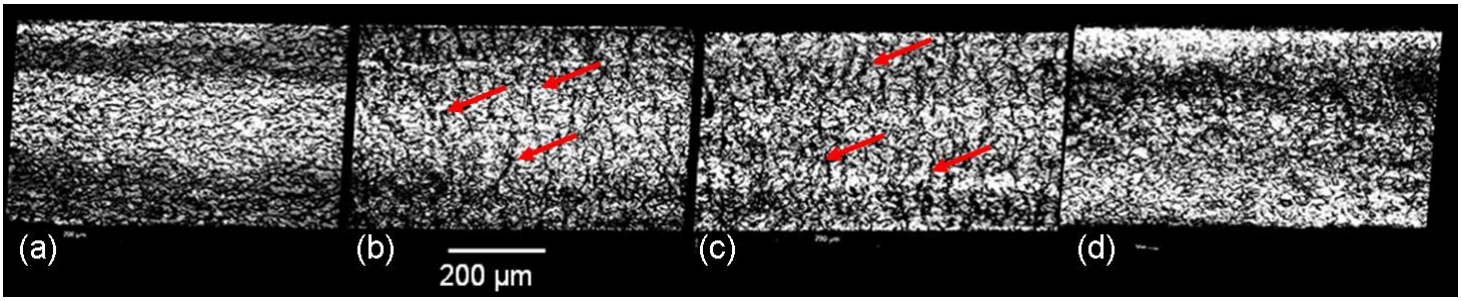

Figure 3-24 Zircaloy-4 sample 608 wt ppm heated at 550°C then cooled down with 100 MPa applied (a) 2mm from left edge of sample (LE); (b) 6mm from LE (gage section); (c) 8 mm from LE (gage section); (d) 12 mm for LE which is the right edge (the arrows indicate re-oriented hydrides).

In order to determine the threshold stress for reorientation, several samples with different applied tensile load but similar hydrogen content and same heating and cooling cycle were studied using metallography. By analyzing the metallographs using Hydromorph®, we were able to determine for each sample the percent of radial hydrides before and after each experiment. The radial hydride content (RHC) is defined in section 2.3 as the number of hydride particles lying at an angle between 65º and 90º with respect to the circumferential direction (which is the ND in our plate shaped samples) plus 0.5 times the number of 'mixed hydrides' which are those that lie between 40º and 65º away from the ND. The circumferential hydrides are those that lie between 0º and 40º away from the ND. The evolution of the RHC as a function of applied tensile stress is presented in Figure 3-18 for Zircaloy-2 and Zircaloy-4 samples with approximately 600 wt.ppm. The RHC values before and after heat cycling with applied stress are presented in Table 3-4. For the Zircaloy-2 samples, the percent of radial hydrides after cooling under a stress of 75 MPa is about 40%, compared to initial values of about 20%. The fact that no meaningful difference is seen between the Zircaloy-2 samples cooled at 75 MPa-100 MPa suggests that the threshold stress seems is below 75 MPa. For the Zircaloy-4 sample, there is a clear increase of the RHC at about 85 MPa. This leads us to believe that for Zircaloy-4 samples, the threshold stress for reorientation is around 80 MPa since at 75 MPa no significant change in the RHC is observed and

at 85 MPa there is a significant change in RHC (see Table 3-4). After 85 MPa, the RHC continues to increase for Zircaloy-4 samples.

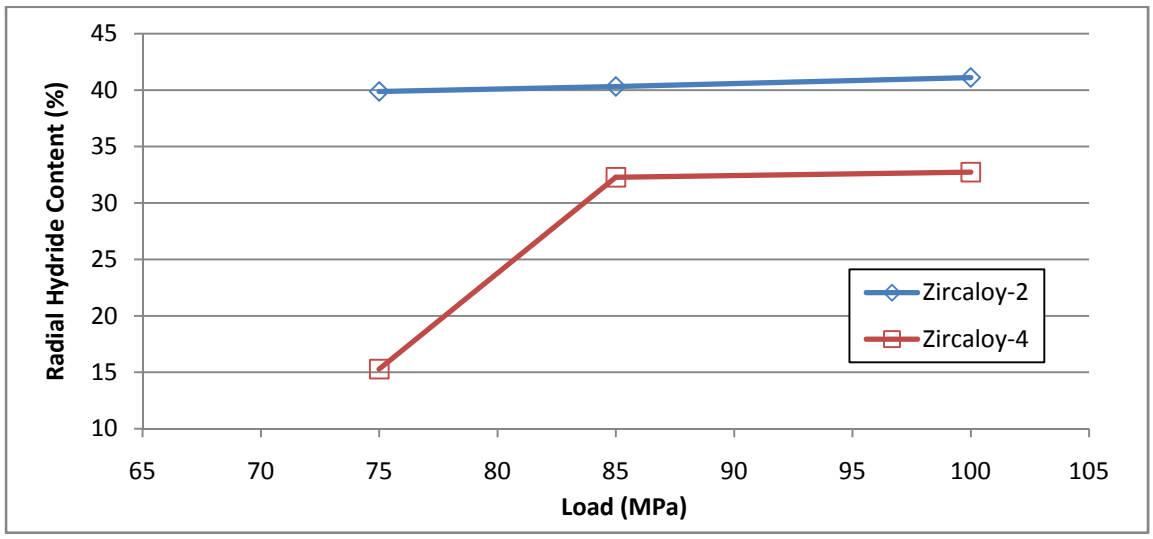

Figure 3-25 Evolution of radial hydride content in percent with tensile load applied to the sample for Zircaloy-2 and Zircaloy-4 samples which have approximately 600 wt.ppm.

Table 3-4 Radial hydride content in percent before and after applied tensile load for Zircaloy-2 and Zircaloy-4 samples which have approximately 600 wt.ppm.

	Stress (MPa)	RHC (%)	
		Before treatment	After treatment
Zircaloy-2	75	19	40
	85	24	40
	100	24	41
Zircaloy-4	75	15	15
	85	17	32
	100	18	33

In this section, hydride reorientation while cooled under tensile stress has been observed by metallography, and quantified using image analysis. The threshold stress for reorientation is estimated to be approximately 80 MPa for cold worked stress relieved Zircaloy-4 samples and below 75 MPa for fully recrystallized Zircaloy-2 samples. This difference in threshold stress is possibly due to different pulling directions (TD for the Zircaloy-2 samples and RD for the Zircaloy-4 samples) and different initial matrix microstructures for both alloys. It was also observed that the reoriented hydrides are much coarser for Zircaloy-4 than for Zircaloy-2.

3.4.2. *Effect of stress on the kinetics of dissolution and precipitation of hydrides*

In this section, the effect of applied stress on the kinetics of dissolution and precipitation is studied using transmission x-ray diffraction. Figure 3-26 shows the heat/load cycles applied to a Zircaloy-2 TD sample with different tensile stresses in the ND for each cycle. The maximum temperature during each cycle is 400ºC which is enough to dissolve all the hydrides for a sample with 140 wt.ppm of hydrogen. The integrated intensities of the hydride $(111)_\delta$ peaks are plotted for both integration banks. It is seen that the $(111)_\delta$ peak intensity in the RD bank increases with increasing stress for stresses higher than 60 MPa (that of the ND bank remains constant). This might be due to the fact that hydrides that were initially scattered for the TD samples as seen in the previous sections are reoriented, thus changing their diffracted intensity. The reorientation threshold stress for Zircaloy-2 samples has been seen to be below 75MPa, consistent with the possibility of reorienting hydrides for the TD sample.

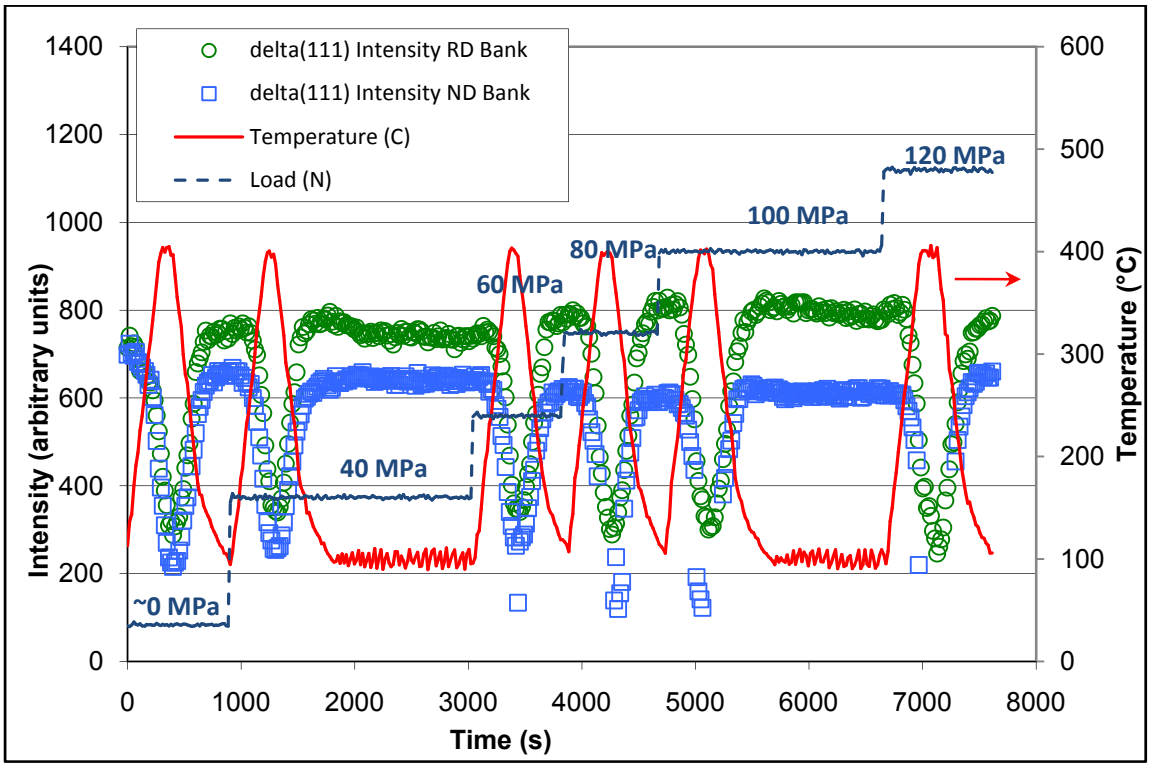

Figure 3-26 Diffracted intensity of the two integration banks of the delta(111) hydride peaks for a TD Zircaloy-2 sample with 140 wt.ppm loaded at different values (heating and cooling rates were constant at 1ºC/s).

It is interesting to note that the minimum values for the intensity along the ND bank decrease further than the initial values after 60 MPa is applied while the minima of the RD bank curve stay constant suggesting that stress stabilizes those hydrides with $(111)_\delta$ planes perpendicular to the applied stress.

For each cycle, the T_d and T_p have been estimated and their values are reported in Table 3-5 and plotted in Figure 3-27. It is seen that for no applied stress, the dissolution and precipitation temperatures are in good agreement with the temperatures for TSSd and TSSp from McMinn [8]. As the applied stress is increased, the dissolution temperature remains constant and within the expected values. The precipitation temperature decreases for stresses below 60 MPa, which is likely due to easier nucleation and precipitation of hydrides in-between stretched zirconium planes. After 80 MPa which is above the threshold stress for reorientation of hydrides in Zircaloy-2, the precipitation temperature increases. This is likely due to reoriented hydride precipitation which has different kinetics than the non-reoriented hydride precipitation.

Table 3-5 Dissolution and precipitation temperatures for the TD Zircaloy-2 sample studied in Figure 3-26 compared to the expected values from [8].

Stress (Mpa)	Td (°C)	Expected dissolution temperature (°C)	Tp (°C)	Expected precipitation temperature (°C)
0	397	390 ± 10	356	340 ± 10
40	397	390 ± 10	352	340 ± 10
60	398	390 ± 10	345	340 ± 10
100	399	390 ± 10	383	340 ± 10
120	404	390 ± 10	395	340 ± 10

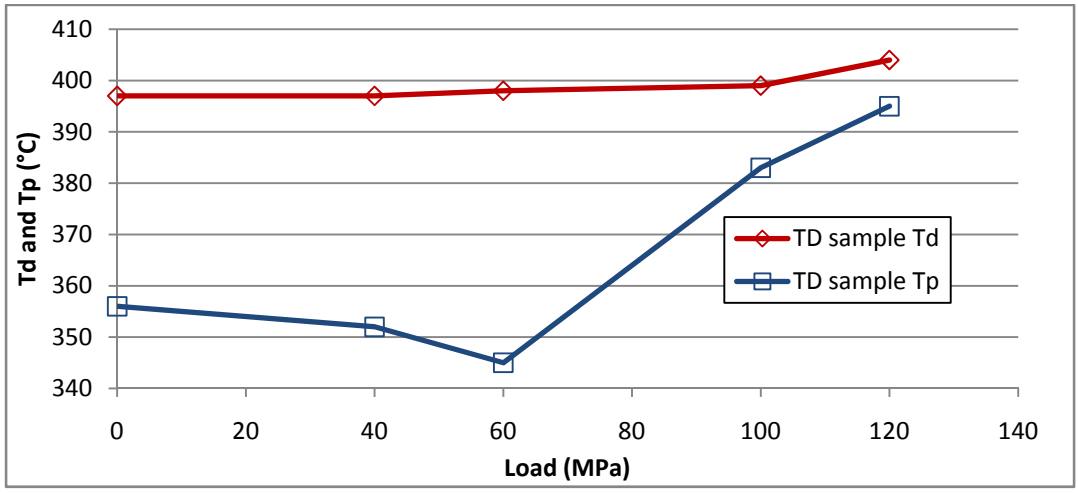

Figure 3-27 Dissolution and precipitation temperatures as a function of load for a loaded Zircaloy-2 TD sample with 140 wt.ppm of hydrogen.

In this section, we have seen that hydrides precipitate faster (at higher precipitation temperature) with applied stress likely because hydride nucleation is made easier by the applied stress until reorientation starts to occur, at which point a higher precipitation temperature is observed. The dissolution temperature, however, is not significantly affected by stress and remains within the expected values at all applied loads. It has also been observed that above 60 MPa, the delta (111) peak intensity increases in the RD bank but stays constant for the TD bank. This change in diffracted intensity could be caused by hydride reorientation since the threshold stress for reorientation for Zircaloy-2 is below 75 MPa, as seen in section 3.4.1.

3.4.3. Effect of stress on hydride morphology

In this section, a Zircaloy-4 sample loaded under tension at 75 MPa but for which no reorientation occurred is studied by transmission x-ray diffraction. By comparing the peak broadening occurring before and after heat/load cycling the sample, we are able to understand the influence of applied stress on hydride orientation and morphology during cool down of hydrides.

In Figure 3-28 and Figure 3-29, the same types of curves as in Figure 3-16 are plotted for the initial state and for the final state after the heat/load cycle (the fits from which the values of FWHM are extracted are shown in Figure 3-30 and Figure 3-31). It is seen that for both integration banks, TD and RD, the strain increases by a similar amount. This is because as the hydrides are strained in the RD, a uniaxial tensile strain is applied on the hydrides in the RD and a corresponding compressive strain occurs in the TD due to Poisson's contraction. Thus both integration banks are strained by a similar amount resulting in an increase in d-spacing of the planes aligned with the RD and a decrease in d-spacing of the planes aligned with the TD direction, as shown by Figure 3-32 (note that a similar variation in d-spacing is seen in the $(100)_{\alpha}$ zirconium peaks). No size broadening is observed in these figures likely because the hydride particles are too big for detectable size broadening.

In this section, the influence of applied stress on hydrides was discussed. It was seen that both integrations banks are more strained after the heat/load cycle by a similar amount. The hydrides in the RD bank are strained in the tensile direction whereas those in the TD bank are strained in the compressive direction. This is physically consistent, since the applied tensile stress is in the RD.

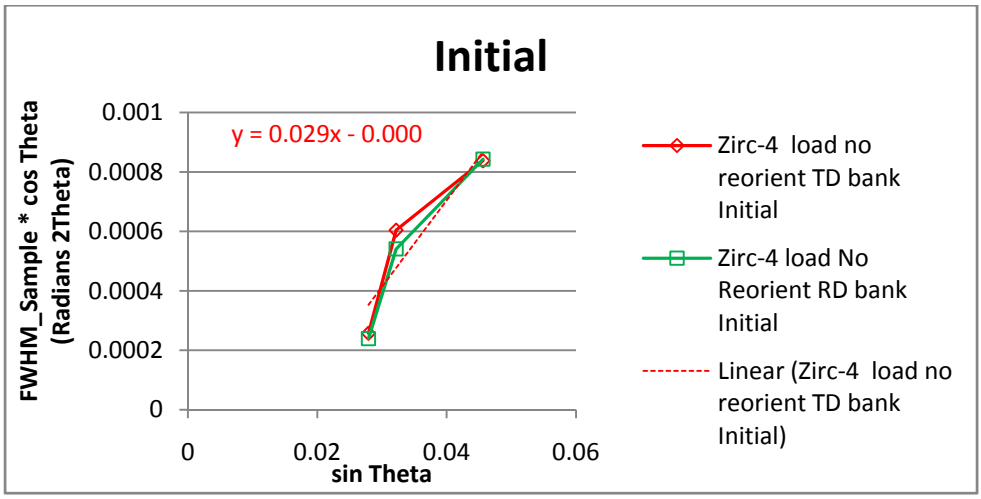

Figure 3-28 Study of size and strain broadening for a Zircaloy-4 sample with 520wt.ppm loaded at 75MPa initially.

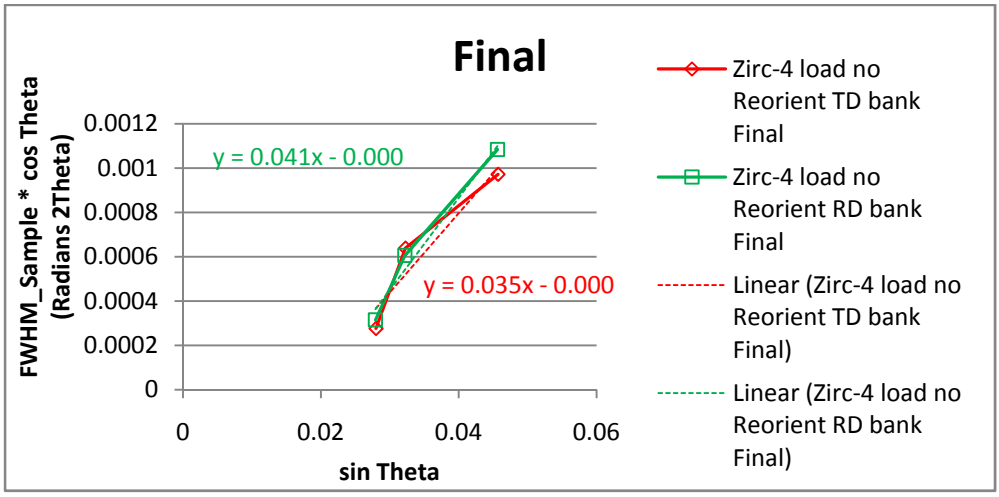

Figure 3-29 Study of size and strain broadening for a Zircaloy-4 sample with 520 wt.ppm loaded at 75MPa after heat/load cycle.

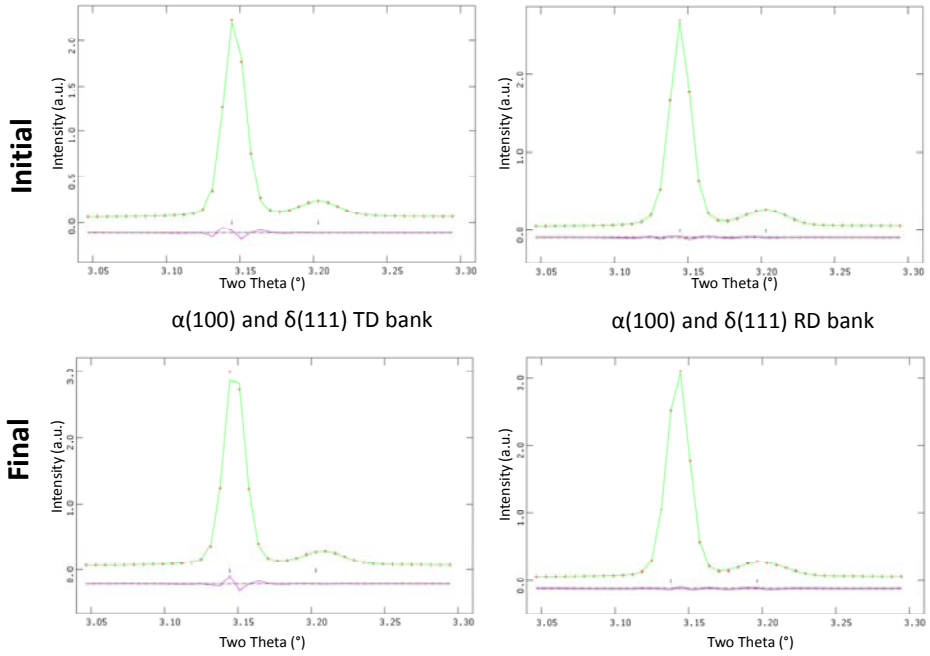

Figure 3-30 Fits of the delta(111) peaks for a Zircaloy-4 sample with 520 wt.ppm before and after heat cycling under 75 MPa stress, obtained using GSAS.

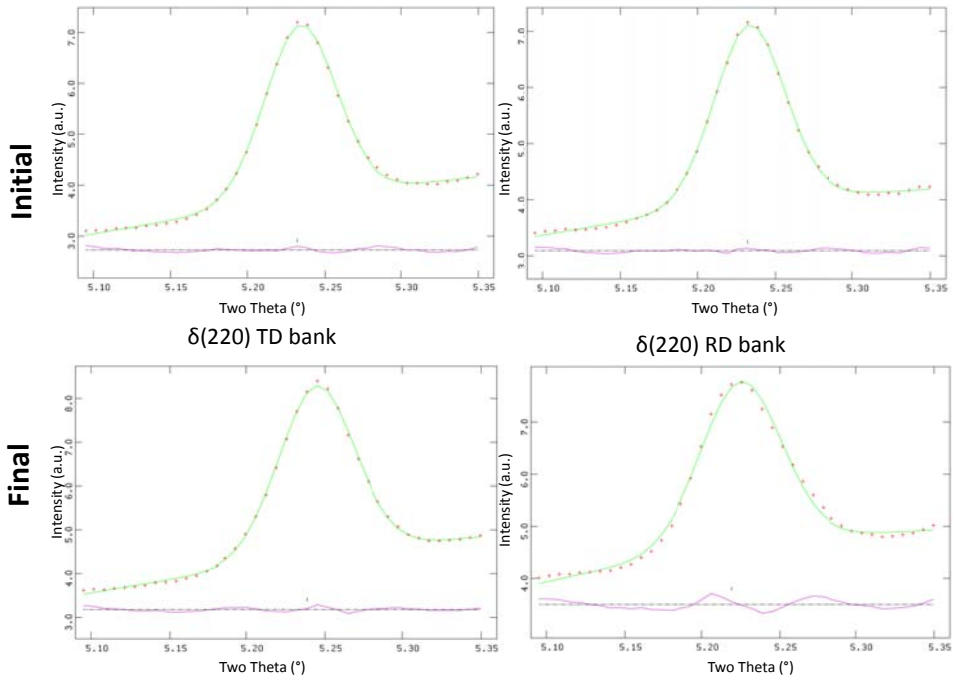

Figure 3-31 Fits of the delta(220) peaks for a Zircaloy-4 sample with 520 wt.ppm before and after heat cycling under 75 MPa stress, obtained using GSAS.

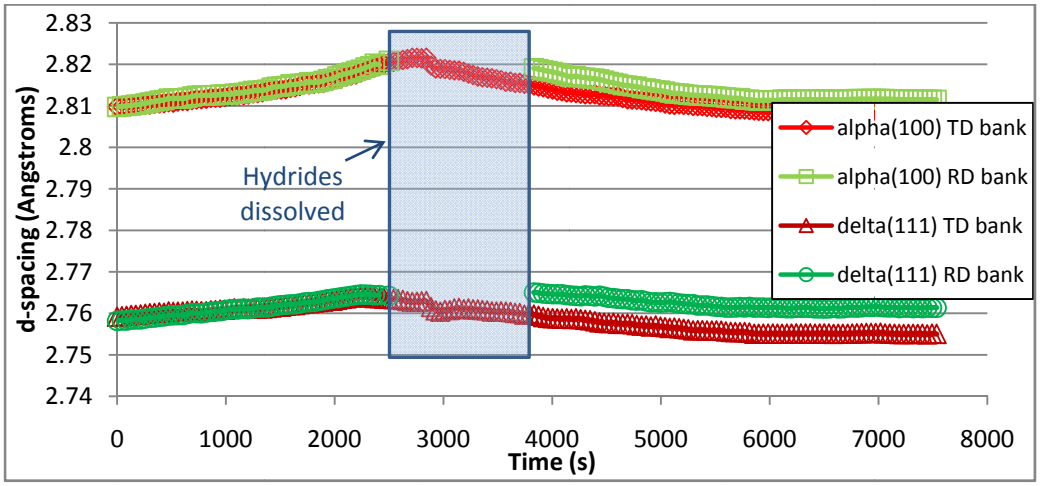

Figure 3-32 d-spacing of the alpha(100) and delta(111) peaks of a Zircaloy-4 sample with an applied stress of 75 MPa (no reorientation) and 520 wt.ppm of hydrogen.

3.4.4. *Microstructure of Reoriented Hydrides*

In this section, samples that have reoriented hydrides are studied by transmission x-ray diffraction. The analysis of the hydride peak intensities before and after heat treatment, performed using GSAS, showed that the diffracted intensities of the hydride peaks for the reoriented sample did not change significantly. As will be shown in the following only the study of the peak shape (specifically peak broadening) was able to provide a consistent "diffraction signature" of reoriented hydrides. The first type of graph observed is the Gaussian FWHM for the hydride peak $(111)_{\delta}$ plotted against time (and temperature) in Figure 3-33 and Figure 3-34 for Zircaloy-4 samples with 530 wt.ppm loaded at 85 MPa and 100 MPa respectively. It is observed that the FWHM for the TD bank is constant when comparing its initial value to its final value. For the RD bank however, the FWHM increases after re-precipitation has occurred and continues to increase with time even though the temperature decreases below 150ºC. This behavior is also observed for the 100 MPa sample in Figure 3-34. This particular behavior of the RD bank of the hydrides is only observed in reoriented hydrides and can be considered a reorientation "signature" of reoriented samples.

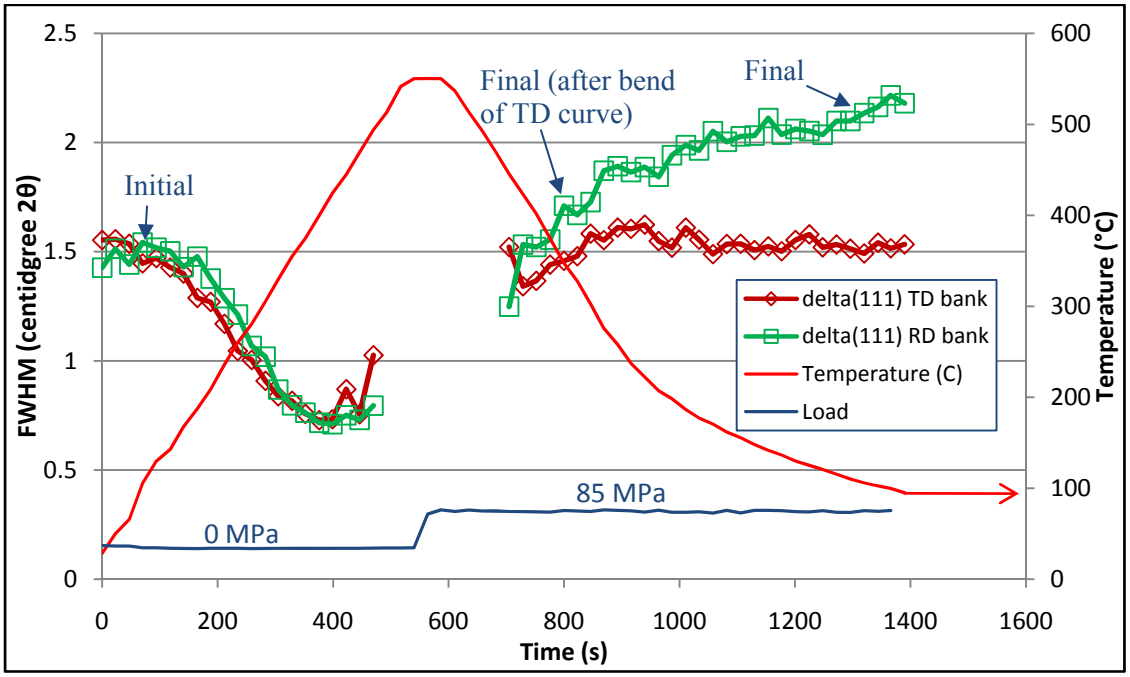

Figure 3-33 Time evolution of the Gaussian broadening of the delta(111) peaks of a Zircaloy-4 sample with 530 wt.ppm of hydrogen heated and cooled under 85 MPa applied stress (with reorientation).

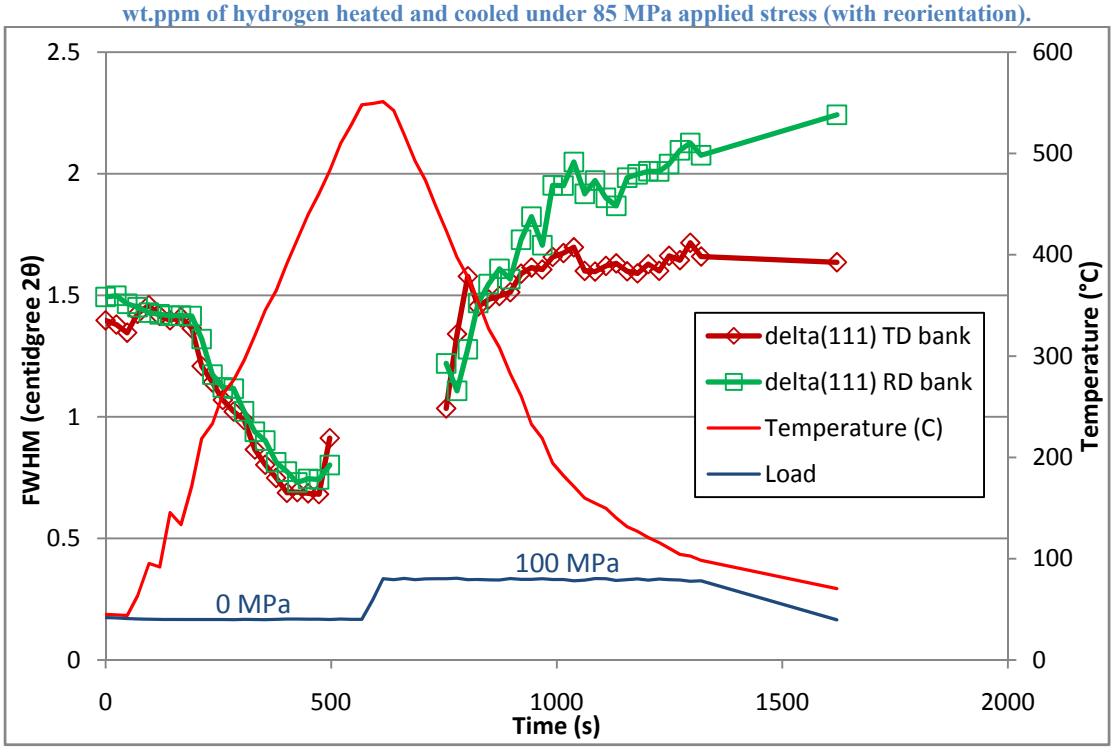

Figure 3-34 Time evolution of the Gaussian broadening of the delta(111) peaks of a Zircaloy-4 sample with 530 wt.ppm of hydrogen heated and cooled under 100 MPa applied stress (with reorientation).

In Figure 3-36, Figure 3-37, Figure 3-38, the size versus strain broadening plots are presented for the reoriented sample loaded at 85 MPa at the initial value, at the bend of the FWHM curve for the TD bank presented in Figure 3-33 and at the final time of recording (some fits for the hydride peaks before and after reorientation are shown in Figure 3-39 and Figure 3-40). The first point is that because the broadening increases with θ, the cause of broadening can likely be attributed to strain. This is true, both for reoriented and non-reoriented hydride particles. This is also true for hydride particles in the as-charged state (see Figure 3-35). Thus the hydride peak broadening is likely due to strain, for the cases studied here. The difference in the reoriented hydrides is that the broadening of the $(111)_\delta$ peak is *larger* in the RD than in the TD. We should note that the diffraction signal of the RD bank after hydride reorientation comes both from $(111)_\delta$ planes whose normals are *aligned* with the stress and planes whose normals are *perpendicular* to the applied stress. In contrast, the signal for the TD bank comes only from $(111)_\delta$ planes whose normal are *perpendicular* to the stress. In this context, a plausible explanation for the broadening difference between the RD and the TD is that more strain (either plastic or elastic) is accumulated in the direction normal to the hydride platelet as it precipitates and grows. This is in fact, where strain is likely to accumulate during plate-like precipitate growth. The examination of Figure 3-34 shows that even as the stress was removed towards the end of the run, the observed broadening remained, which suggests that the strain causing the broadening is mostly *plastic* strain, likely in the form of dislocations.

Paradoxically, the analysis of the slopes from the Figure 3-36 to Figure 3-38 would suggest that the strain is larger on the TD than the RD (higher slope). However, because hydride reorientation was not complete, such that half of the hydrides present at the end are in-plane hydrides, it is likely that much of the $(220)_\delta$ peak intensity in the RD comes from in-plane hydrides. The analysis mentioned above is only valid of the same hydride particle contributes intensity to both $(111)_\delta$ and $(220)_\delta$. This hypothesis is confirmed by the analysis of Figure 3-35, in

which all hydrides are in-plane but the sample is examined from the RD, yielding a curve in which the slope of the TD is similar to that of the ND.

In summary the data is consistent with greater strain observed in the direction normal to the hydride platelets. When the examination is conducted in the RD, this difference shows a "signature" of hydride reorientation.

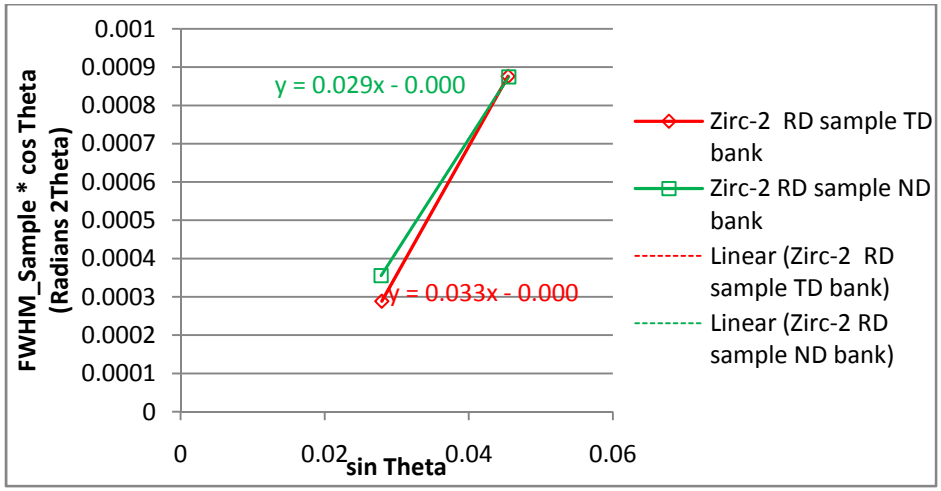

Figure 3-35 Study of size and strain broadening for a RD Zircaloy-2 sample with 520 wt.ppm before any heat/load treatment (x-ray beam parallel to RD).

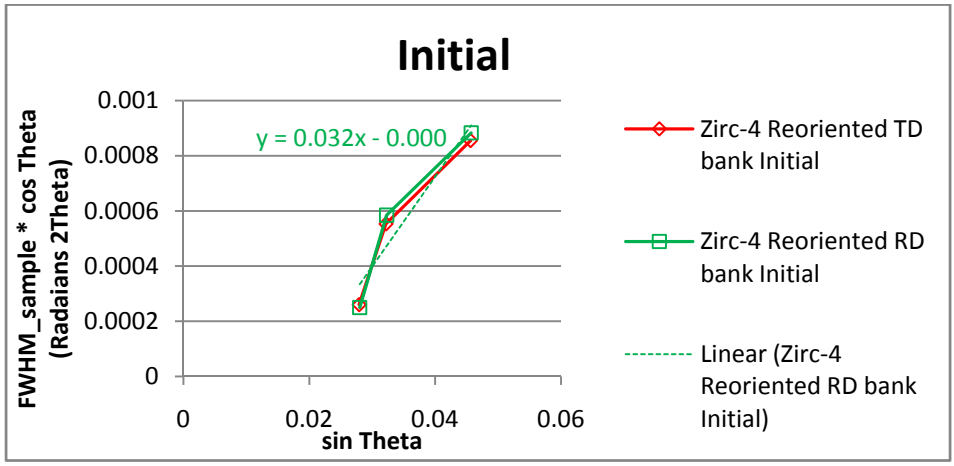

Figure 3-36 Study of size and strain broadening for a reoriented Zircaloy-4 sample with 530 wt.ppm loaded at 85MPa initially.

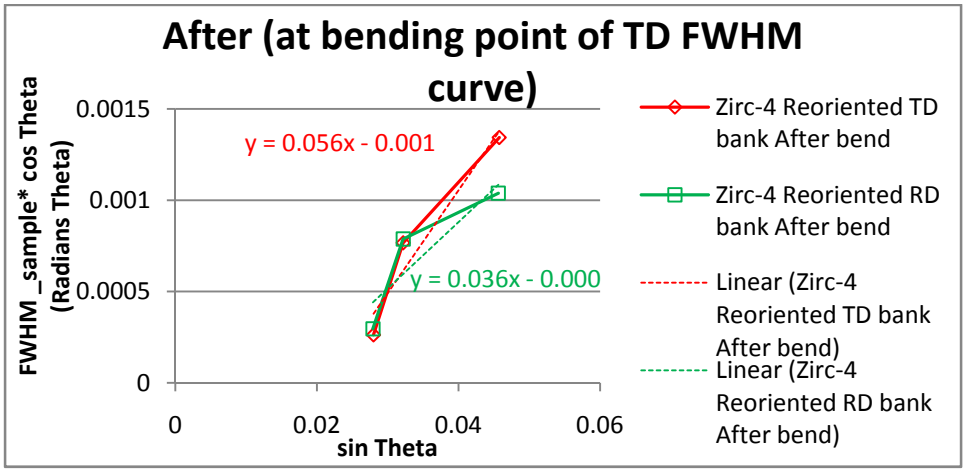

Figure 3-37 Study of size and strain broadening for a reoriented Zircaloy-4 sample with 530 wt.ppm loaded at 85MPa at the bending point.

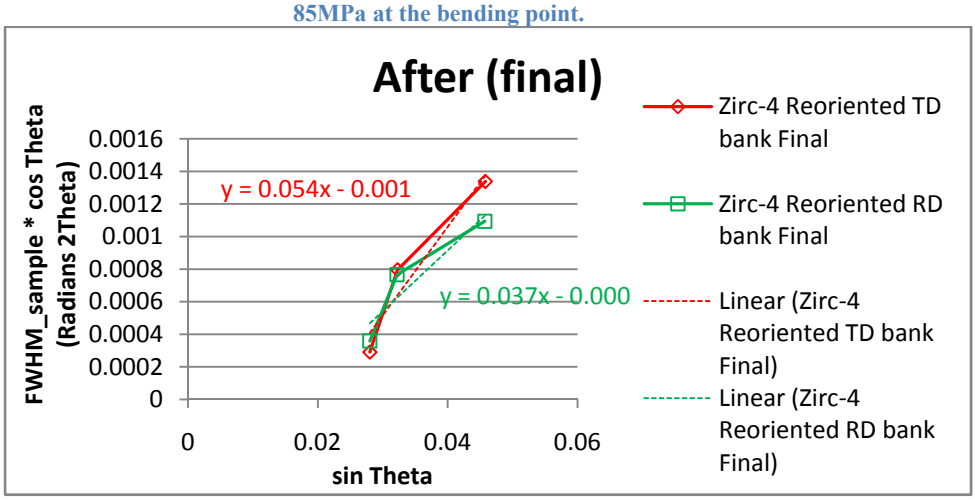

Figure 3-38 Study of size and strain broadening for a reoriented Zircaloy-4 sample with 530 wt.ppm loaded at 85MPa after the heat/load cycle.

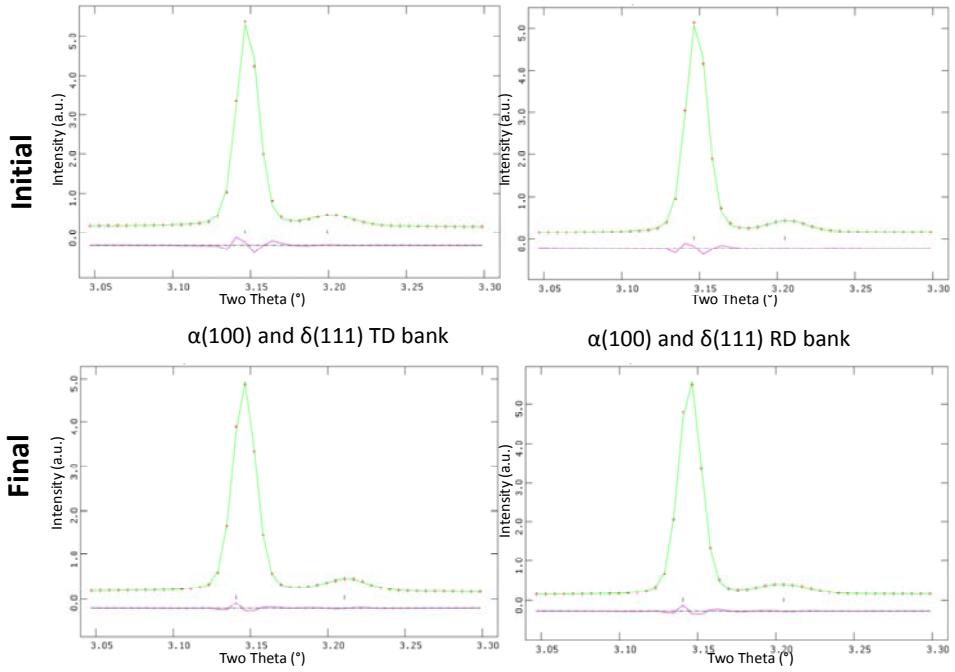

Figure 3-39 Fits of the delta(111) peaks of a Zircaloy-4 sample with 530 wt.ppm before and after heat cycling with applied load of 85 MPa and reorientation of hydrides, obtained using GSAS.

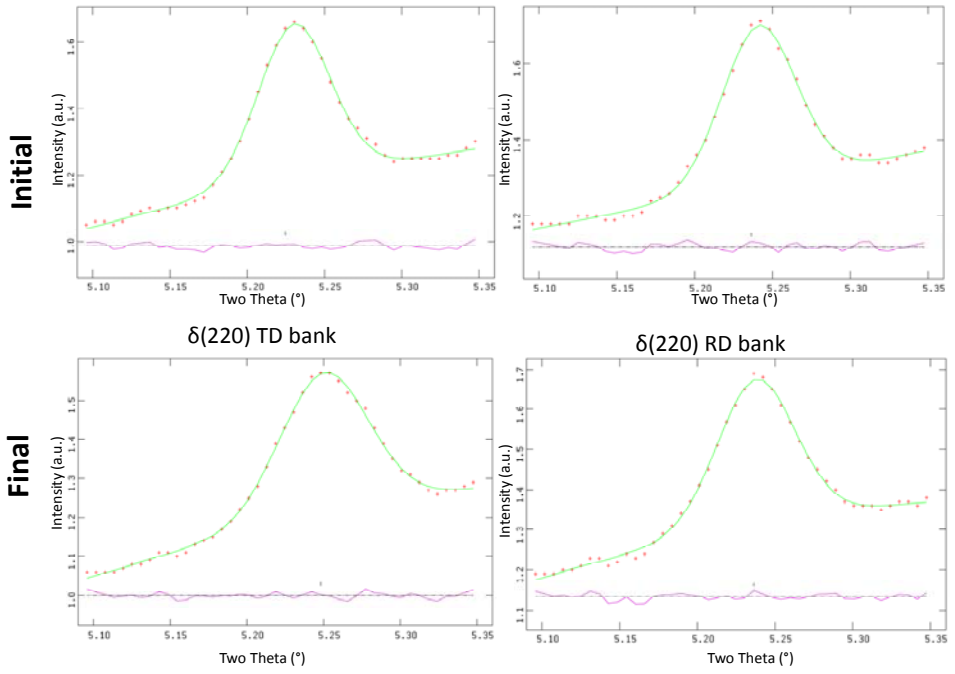

Figure 3-40 Fits of the delta(220) peaks of a Zircaloy-4 sample with 530 wt.ppm before and after heat cycling with applied stress of 85 MPa and reorientation of hydrides, obtained using GSAS.

The d-spacings of the reoriented hydrides for the 85 MPa sample and the 100 MPa sample are presented in Figure 3-41 and Figure 3-42, respectively. For the $(111)_\delta$ hydrides, the d-spacing of the hydrides in the RD bank increases when compared to the initial state (without stress) and the final state (stressed in the RD), and the d-spacing of the TD bank of the hydrides decreases compared to the initial. It is interesting to note that when the stress is removed, the d-spacings become closer to the initial values. This behavior is consistent with the alignment of the RD with the pulling direction and the resultant compressive strain in the TD from Poisson's contraction. These observations imply that it is most likely not because of differences in the d-spacings compared to non-reoriented hydrides that the strain in the TD bank of the reoriented hydrides is much higher than the strain in the RD bank such as observed previously.

The observed strain in the direction normal to the hydrides is likely caused by a combination of the accommodation of size-mismatch (volume expansion during hydride precipitation) and differential thermal expansion of the hydrides and matrix (the thermal expansion for hydrides ($\alpha_{Hydride}$=14.2 x10^{-6} per ºC) is much larger than for alpha zirconium (α_{Zr}=6 x10^{-6} per ºC) [27]).

In this section we have identified a "signature" for hydride reorientation. The main part of this signature is that the FWHM continues to increase in the RD with time even for temperatures below 150ºC whereas the FWHM does not change in the TD. The second part is that the strain in the TD is much higher than the one in the RD. The d-spacing behavior of reoriented hydrides is the same than the behavior for samples under tensile stress without reorientation. This implies that this reorientation "signature" is not due to differences in the d-spacings but to other phenomenon. A possible explanation would be that the diffraction signal from the $(220)_\delta$ peaks comes mostly from circumferential hydrides whereas the diffraction signal from the $(111)_\delta$ peaks comes mostly from reoriented hydrides.

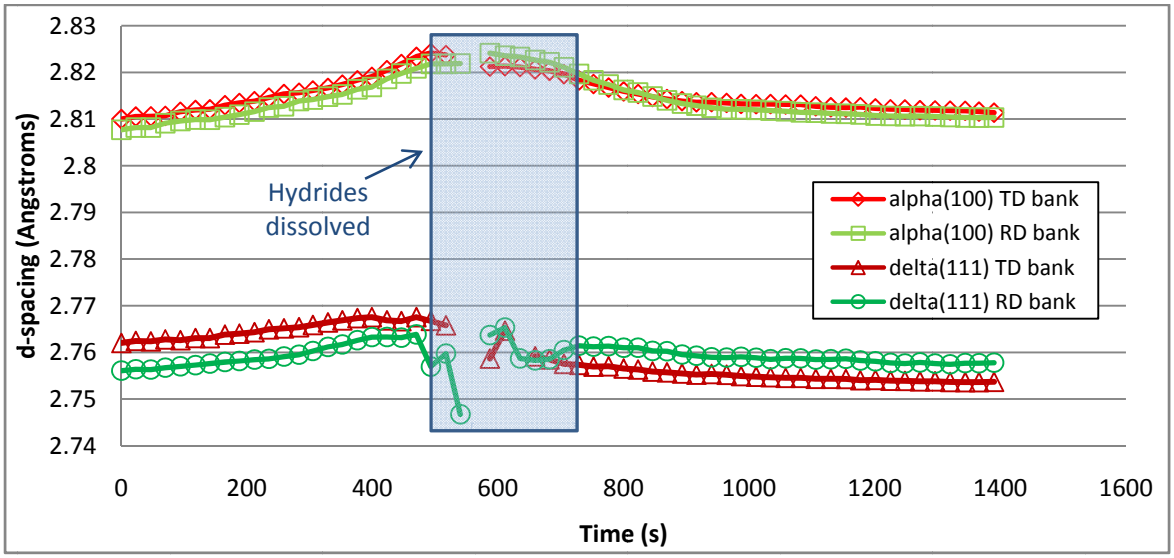

Figure 3-41 d-spacing of the alpha(100) and delta(111) peaks of a Zircaloy-4 sample with an applied load of 85 MPa (with reorientation) and 530 wt.ppm of hydrogen.

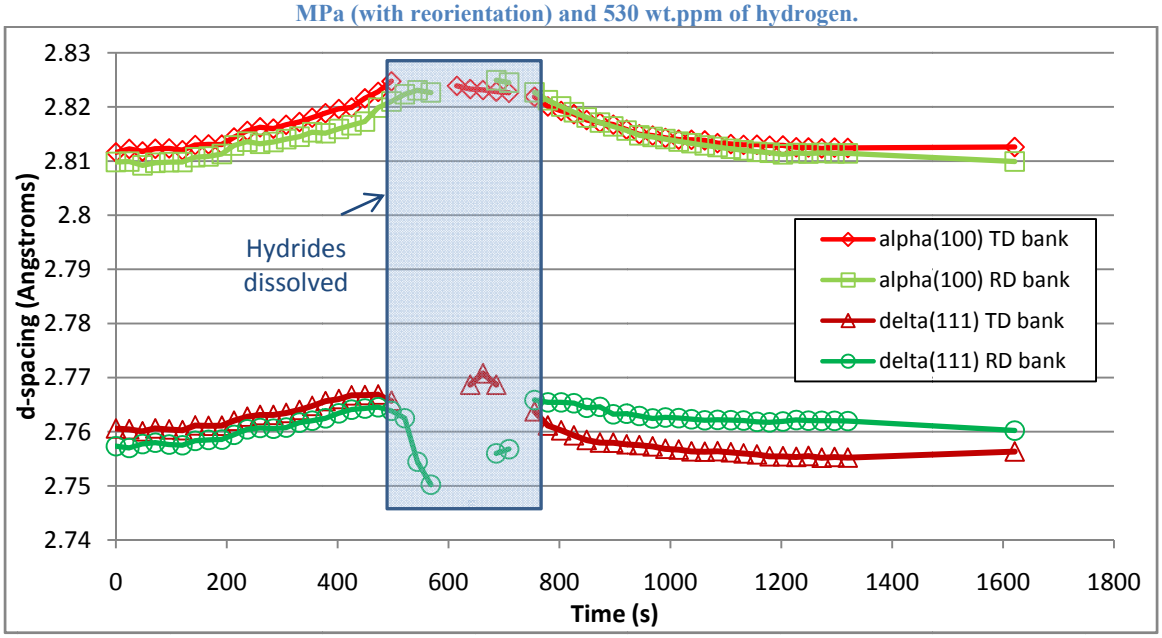

Figure 3-42 d-spacing of the alpha(100) and delta(111) peaks of a Zircaloy-4 sample with an applied load of 100 MPa (with reorientation) and 530 wt.ppm of hydrogen.

3.5. Observation of Crack-tip Hydrides

To better understand what occurs during delayed hydride cracking, it is important to study how a hydrided cracked sample reacts to thermal cycling and loading. Thus a limited test was performed using micro-beam x-ray diffraction to investigate the crack tip in a CT specimen. As explained in section 2.4.4, the crack tip experiment performed in this study is at room temperature with no applied load. The goal of this experiment is to characterize whether the micro-beam of beamline 2-IDD at the APS can observe individual alpha grains and, more importantly, hydride platelets highly concentrated in a small region. The CT sample studied here is a re-crystallized Zircaloy-2 sample that was previously hydrided to 100 wt.ppm, followed by heat treatment under load so that the hydrides have grown at the crack of the tip. Two scans are performed in the 'horizontal' and the 'vertical' directions as illustrated in Figure 3-43.

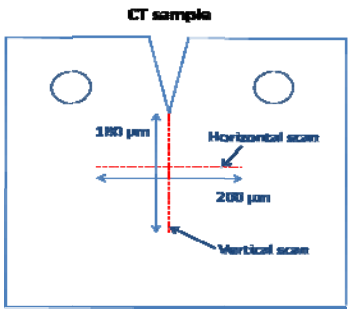

Figure 3-43 Schematic representation illustrating the scans performed on the CT sample at beamline 2-IDD.

Each scan has a step size of 5µm. Figure 3-44 shows the diffracted intensity plotted versus 2θ angle for various horizontal scan positions. Figure 3-45 present the same information in the form of a contour plot. The alpha zirconium peaks and (at certain positions) some hydride peaks are identified in Figure 3-44 and Figure 3-45. This illustrates the fact that the beam is able to detect hydrides and individual alpha zirconium grains. The vertical scan diffraction patterns for each step are plotted as a function of distance to the crack tip in Figure 3-46 and Figure 3-47. The alpha peaks and some delta hydride peaks are observed. The variation in intensity of the alpha and the delta peaks is due to the fact that the grains are oriented in different orientation with respect to the beam and thus are not always in a good position for Bragg diffraction.

For each step in a scan, the diffraction patterns can be individually plotted as in Figure 3-48 for some steps extracted from the vertical scan and in Figure 3-49 for some steps extracted from the horizontal scan. In these figures, we see that the Bragg peaks are distorted and, for many peaks, if we compared the value of the peak position to the expected position presented in Table 2-1, the peaks are shifted. This demonstrates that the matrix, and the hydrides, is highly stressed around the crack. The hydrides peaks in this highly stressed zone are also distorted in an inhomogeneous manner. In Figure 3-48, for the scan at the tip of the crack we observe the $(111)_{\delta}$ and the $(200)_{\delta}$ peaks for the hydride. This shows that there are crack tip hydrides and validates the use of the micro-beam XRD to observe in-situ hydride precipitation at the tip of a crack. The other peaks observed in the diffraction patterns presented in Figure 3-48 and Figure 3-49 are not likely to be intermetallic precipitates [54]. The observation of Figure 3-45 and Figure 3-47 shows an approximate grain size for the alpha zirconium of about 20 μm which is what is expected for the re-crystallized material we used in this study.

In this section, we have seen by observing a CT specimen by micro-beam XRD that we can observe individual alpha grains and hydride precipitates. Some of the hydride precipitates for this sample are located at the tip of the crack. The strong shift and distortion of the Bragg peaks suggest that there is a stress state effect at the tip of the crack where alpha grains and hydride precipitates are stressed. The use of micro-beam for the in-situ study of hydride precipitation at the tip of a crack is seen to be possible, but more systematic study need to be conducted. Suggestions for crack tip experiment are presented in Chapter 5.

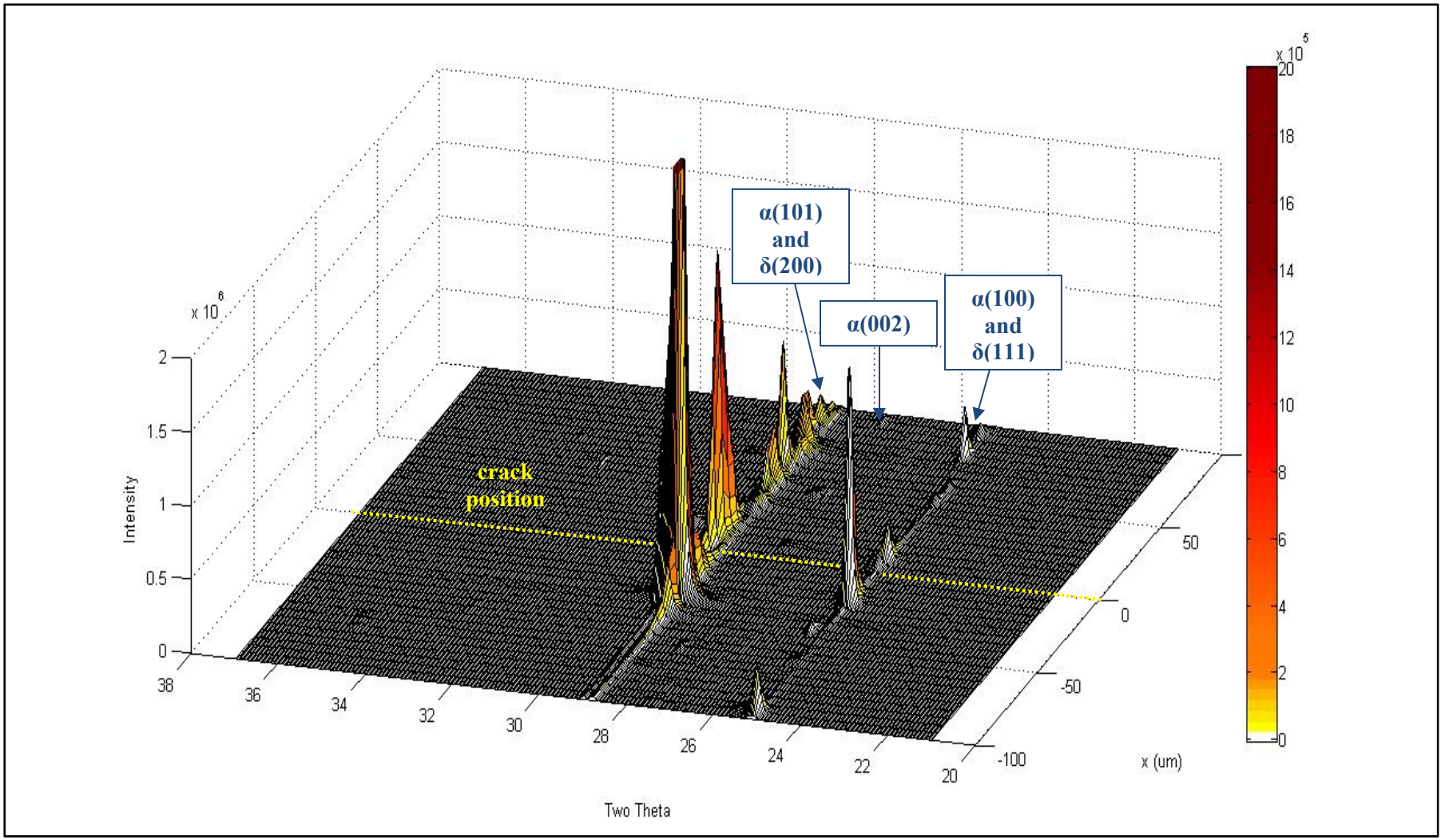

Figure 3-44 Horizontal scan of a Zircaloy-2 CT sample hydrided at 100 wt.ppm pre-cracked with hydrides grown at the tip of the crack; surface plot of the diffraction patterns.

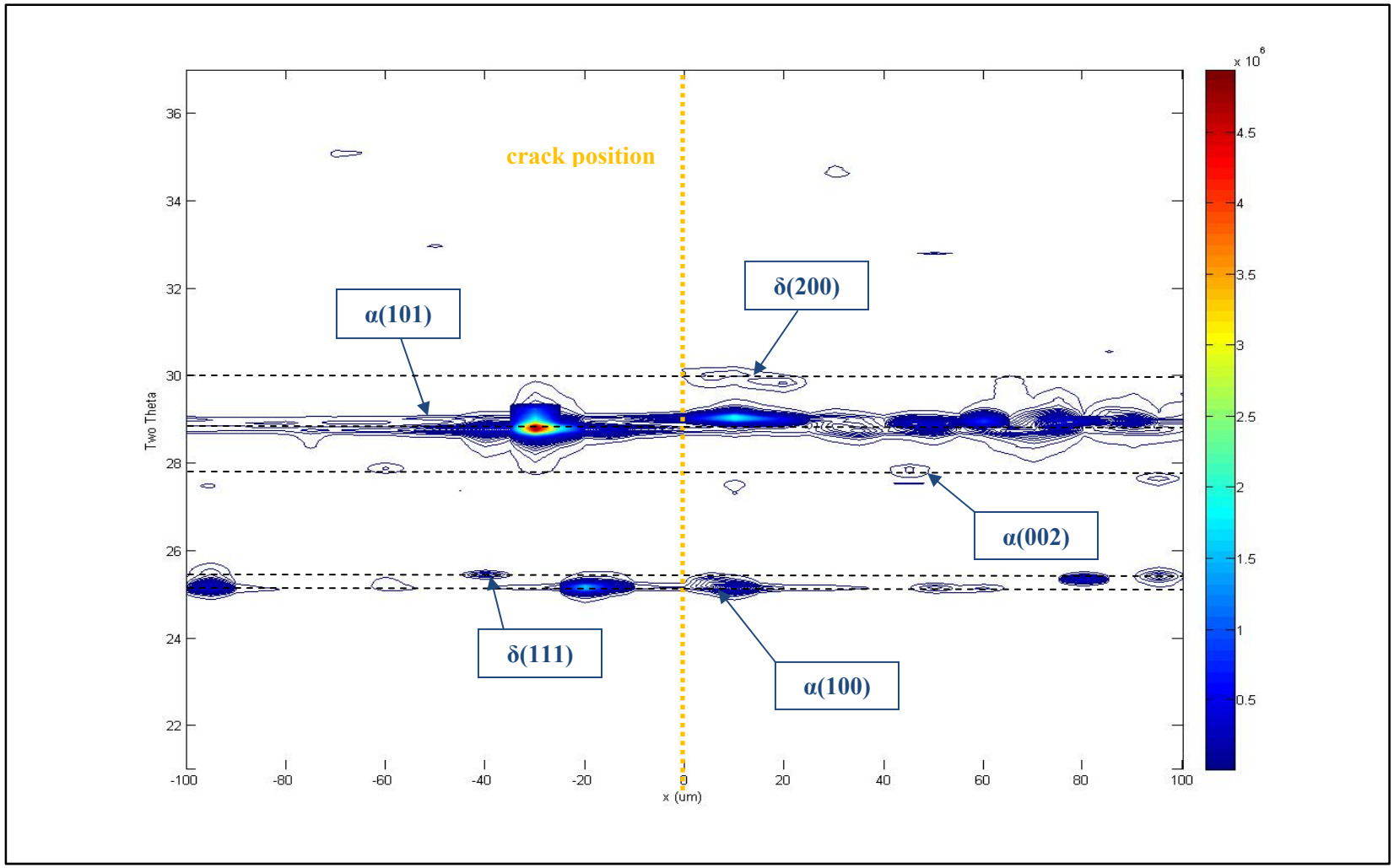

Figure 3-45 Horizontal scan of a Zircaloy-2 CT sample hydrided at 100 wt.ppm pre-cracked with hydrides grown at the tip of the crack; contour plot of the diffraction patterns.

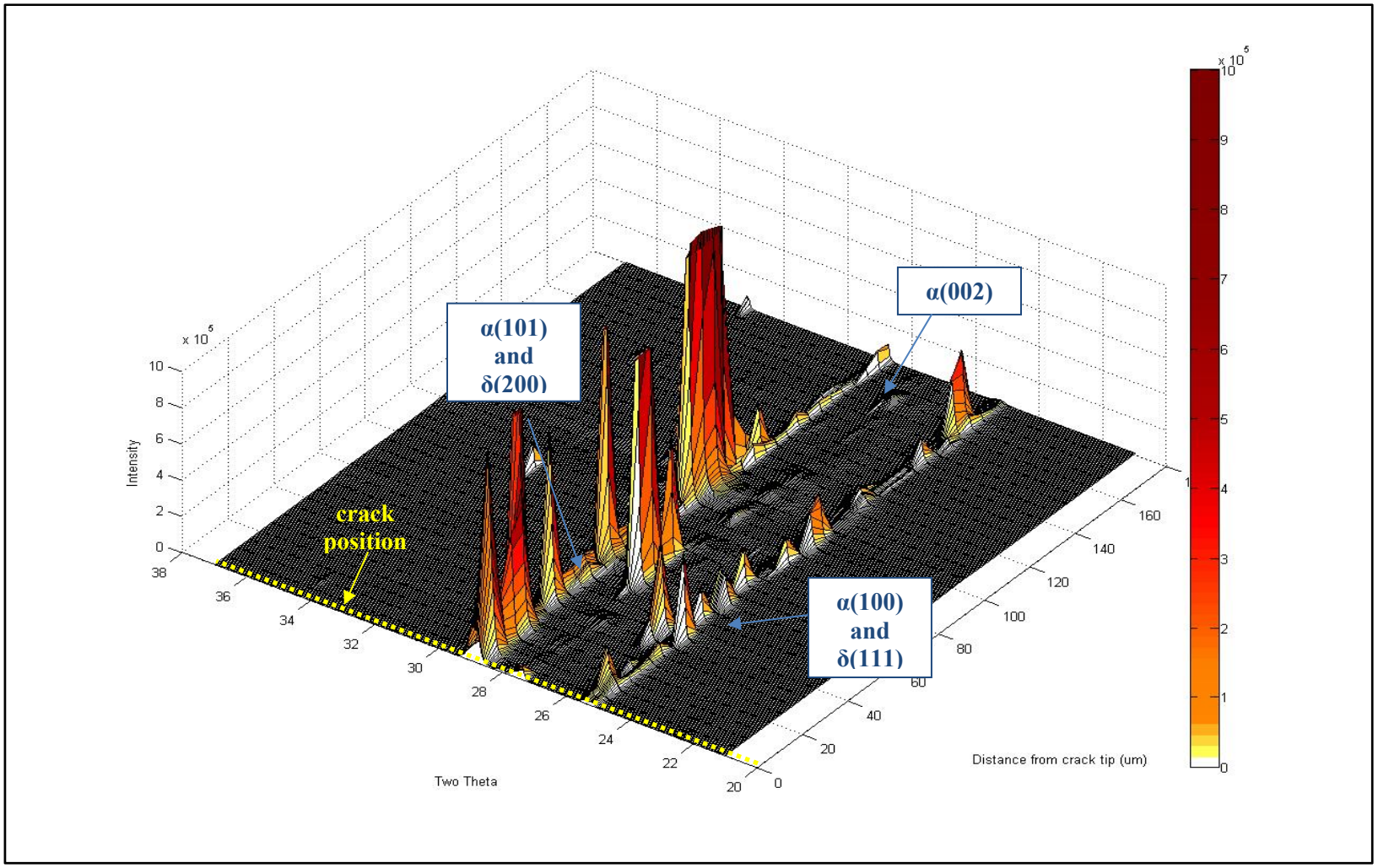

Figure 3-46 Vertical scan of a Zircaloy-2 CT sample hydrided at 100 wt.ppm pre-cracked with hydrides grown at the tip of the crack; surface plot of the diffraction patterns.

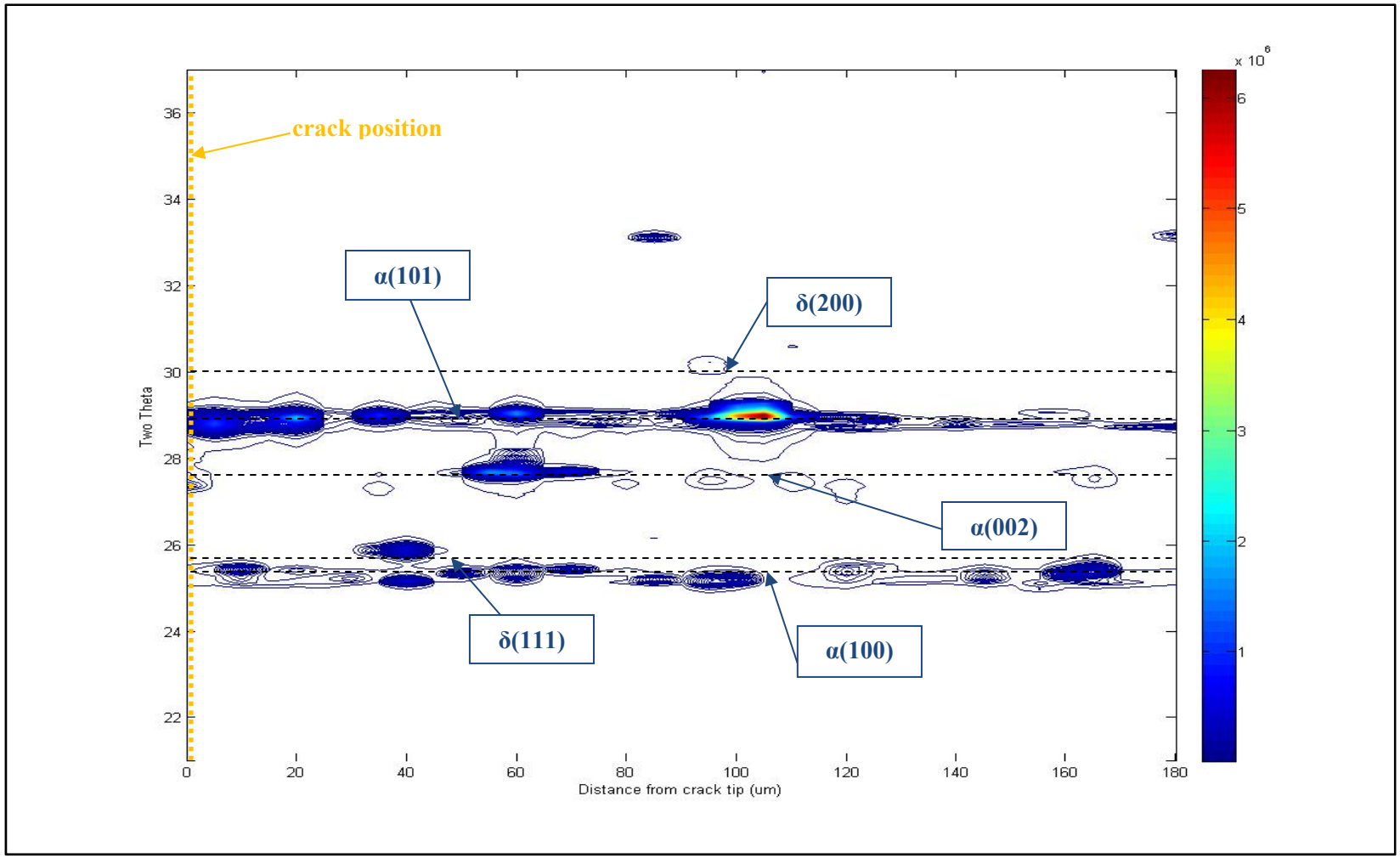

Figure 3-47 Vertical scan of a Zircaloy-2 CT sample hydrided at 100 wt.ppm pre-cracked with hydrides grown at the tip of the crack; contour plot of the diffraction patterns.

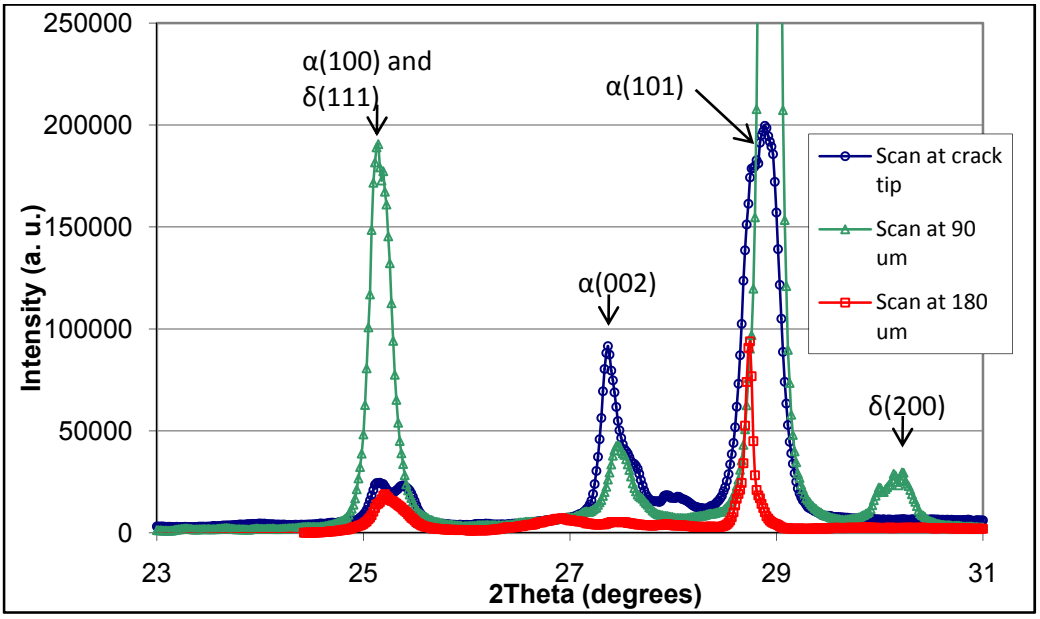

Figure 3-48 Selected diffraction patterns from the vertical scan of the CT Zircaloy-2 sample with 100 wt.ppm of hydrogen and crack tip hydrides.

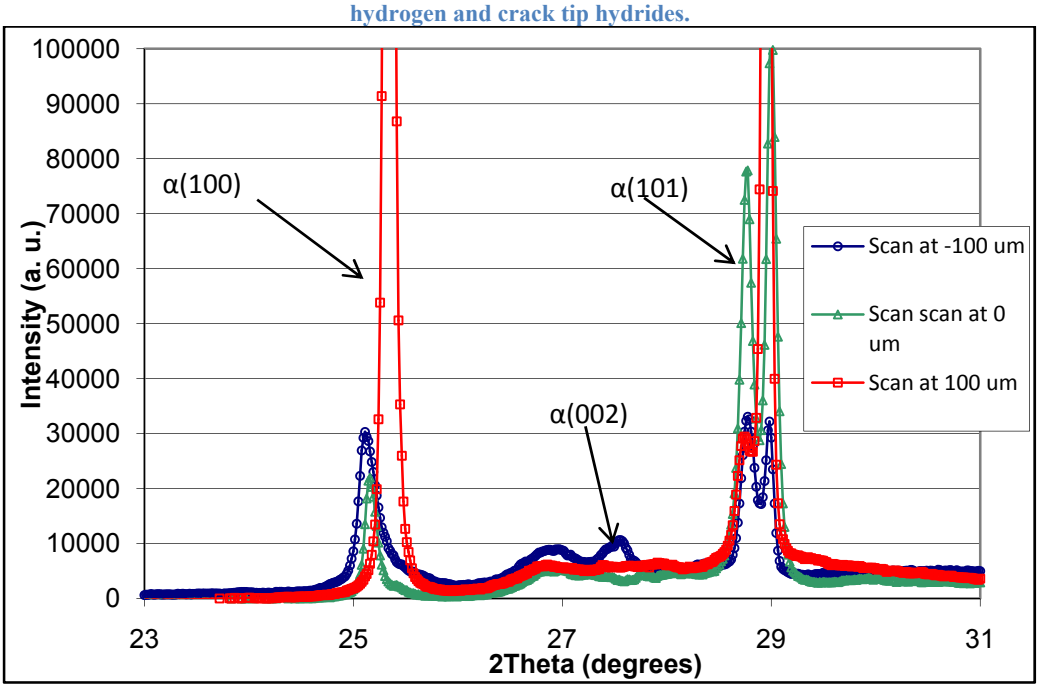

Figure 3-49 Selected diffraction patterns from the horizontal scan of the CT Zircaloy-2 sample with 100 wt.ppm of hydrogen and crack-tip hydrides.

Chapter 4

CONCLUSIONS AND FUTURE WORK

4.1. Summary and Conclusions

The kinetics of hydride dissolution and precipitation was studied using synchrotron radiation and metallography. The observed materials were Zircaloy-2 and Zircaloy-4 hydrided from 80 to 610 wt.ppm. The samples were heated and cooled at different rates and with different applied stresses during cooling. The use of synchrotron radiation enabled a unique in-situ study of the parameters influencing the hydride dissolution and precipitation. The main conclusions of this study are:

1. The hydrogen content of the alloys was determined using two techniques, based on synchrotron radiation diffraction and on image analysis of metallographs, which were compared to hot vacuum extraction for the estimation of the hydrogen contents of a sample. A calibration factor was found for the image analysis method. These methods are shown to give a good first order approximation of the local hydrogen contents of a sample.

2. Metallographs show that in the absence of applied stress, the zirconium hydrides precipitate in the RD/TD plane and they are platelet shaped. The perpendicular to the thin direction of the platelet is parallel to the matrix normal direction (ND). Given the matrix texture this orientation is consistent with an orientation relationship of $(111)_{\delta}//(0002)_{\alpha}$. In the Zircaloy-2 samples, the RD bank of the

$(111)_\delta$ peak shows greater broadening than the TD bank. The ND bank of the same peak is slightly broadened as well.

3. The hydride dissolution and precipitation temperatures, T_d and T_p, were determined by studying the evolution of the diffracted intensity of the hydride peaks. At slower cooling rates, these temperatures are in good agreement with the expected temperatures at the TSSp and TSSd for the samples' hydrogen contents from the literature. For fast heating and cooling rates however, the dissolution and precipitation temperatures differ from the expected values at the TSS likely because the sample is then farther from thermodynamic equilibrium. Hydrides that precipitate at slower cooling rates are coarser than those than precipitate at faster cooling rates, as shown by optical metallography

4. The analysis of the dependence of the observed hydride peak broadening with $\sin\theta$ indicates that most of the broadening is caused by strain. This is true both in the as-prepared hydrided samples and in those that underwent heat treatment and cooling under stress.

5. When stress is applied during cool down, the precipitation temperature T_p first decreases suggesting faster hydride nucleation rate under stress then increases when reorientation starts to occur. The dissolution temperature T_d is not significantly affected by stress.

6. When cooled under stress, hydrides are found to reorient with the platelets normals parallel to the loading axis. The threshold stress for reorientation is

estimated to be around 80 MPa for Zircaloy-4 and between 60 and 75 MPa for Zircaloy-2.

7. When hydrides are heated and stressed in the RD during cool-down but do not reorient, they show similar increases in peak broadening (relative to the initial value) in the TD and in the RD. The variations in the d-spacings of the hydride planes in question are consistent with the planes whose normals are parallel to the loading axis (RD) being under tension and those whose normals are perpendicular to the loading axis (TD) being under compression.

8. A distinct hydride reorientation diffraction "signature" has been identified for hydrided Zircaloy-4 samples which are heated and cooled under stress applied in the RD. This signature is present only when cooled under an applied stress above the threshold stress for reorientation. The analysis of the FWHM of the $(111)_\delta$ hydride peaks in the RD and TD shows it to be distinctly different in samples with reoriented hydrides from those in which reorientation did not occur. In samples where reorientation occurred, the $(FWHM)_{TD}$ returns to the initial value, while the $(FWHM)_{RD}$ increases steadily as precipitation proceeds. In the non-reoriented samples, the FWHM for both TD and RD return to the original value. The fact that greater peak broadening of the $(111)_\delta$ peaks is seen in the direction which contains hydride short dimension is consistent with most tensile stress effects occurring in the direction normal to the surface of the platelet. However, the broadening of the $(220)_\delta$ peak is smaller in the RD than in the TD, which causes the estimated strain (proportional to the slope of these graphs) along the RD to be smaller than along the TD. This could be due to the fact that the

diffraction signal from the $(220)_\delta$ peaks comes more strongly from non-reoriented hydrides whereas the one from the $(111)_\delta$ peaks comes more strongly from reoriented hydrides.

9. Preliminary studies using micro-beam synchrotron radiation were conducted at the tip of a crack in previously hydrided and cracked specimen, showing that hydrides can be detected using this small beam, but greater variability should be expected due to the small volume sampled.

4.2. Recommendations for future work

A more systematic study on the parameters influencing the dissolution and precipitation temperature should be performed at the 1-ID beamline at the APS using transmission x-ray diffraction. Such parameters as heating and cooling rates, hydrogen content and microstructure and stress level should be varied.

A more thorough study of the reoriented hydrides has to be performed. Samples with less hydrogen should be allowed to fully reorient by letting the samples at temperature under load for longer times. The analysis of such samples would be more straightforward and would complement this study well. TEM imaging of reoriented hydrides can yield information on their microplatelet structure, which combined with synchrotron observation could show better understanding of the orientation relationship between microplatelets and the macroscopic hydride platelets. Also a study should be performed of the parameters influencing hydride reorientation (alloys composition, heating/cooling rates, time at temperature, etc). This could lead to a better understanding of the influence of these parameters on the kinetics of dissolution and precipitation of zirconium hydrides.

Finally, as suggested by the last section of chapter 3, a micro-beam crack tip experiment would allow in-situ observation of hydrides growing at the tip of a pre-existing crack and thus be relevant to hydride precipitation near a crack tip. Preliminary studies conducted in present work show promise in this technique.

Appendix A

Hydrogen Charging System and Procedures

The pre-hydrogen charging procedure (oxide layer removal and nickel coating) is done by the following manner:

-Clean samples with acetone and methanol.

-Etch by dipping for 1 minute in a HNO_3 (10 parts), HF (1 part) and H_2O (10 parts).

-Rinse by dipping samples in water for 1 minute.

-Dry by blowing nitrogen on samples.

The hydrogen charging procedure is done by the following manner:

-Heat furnace under vacuum.

-Introduce desired amount of hydrogen in control volume (check with pressure gauge).

-Once furnace is at desired temperature, introduce sample and hydrogen in vacuum chamber.

-Let in place for desired time (1 hour) while noting the pressure in the tank.

-Take samples out of furnace and pump the vacuum back in the chamber.

-Cycle as many times as necessary.

The hydrogen charging system is detailed in Figure A-1:

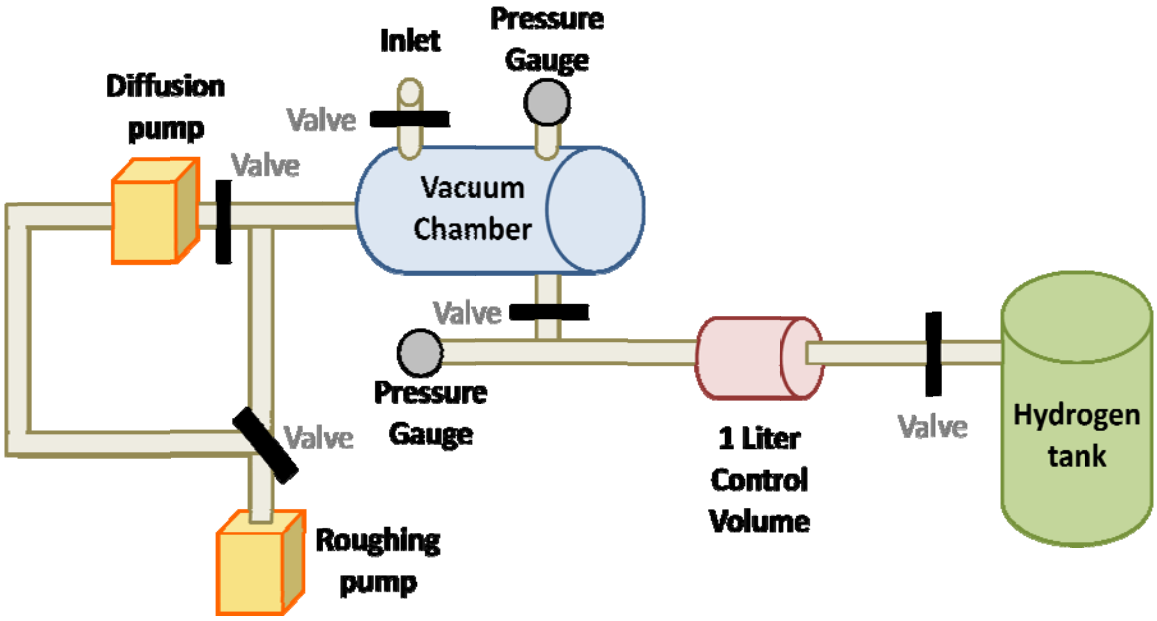

Figure A-1 Hydrogen charging set-up

Appendix B

Powder Diffraction Files for Zirconium and Zirconium Hydrides

The following Powder Diffraction Files are from [53]. Table B-1 and Table B-4 were used in particular in this study:

Table B-1 PDF for α-zirconium.

α-Zirconium			
PDF No 00-005-0665			
d (Angstroms)	Intensity (a.u.)	(h k l)	Theta (degrees)
2.798	33	(1 0 0)	15.980
2.573	32	(0 0 2)	17.420
2.459	100	(1 0 1)	18.256
1.894	17	(1 0 2)	23.998
1.616	17	(1 1 0)	28.468
1.463	18	(1 0 3)	31.770
1.399	3	(2 0 0)	33.408
1.368	18	(1 1 2)	34.269

Table B-2 PDF for γ-hydride (a=4.596 angstroms, c=4.969 angstroms).

γ-hydride			
PDF No 00-034-0690			
d (Angstroms)	Intensity (a.u.)	(h k l)	Theta (degrees)
3.250	1	(1 1 0)	13.710
2.720	100	(1 1 1)	16.451
2.484	19	(0 0 2)	18.065
2.298	30	(2 0 0)	19.585
1.687	24	(2 0 2)	27.170
1.625	11	(2 2 0)	28.300
1.476	16	(1 1 3)	31.468
1.395	14	(3 1 1)	33.522

Table B-3 PDF for γ-hydride (a=4.586 angstroms, c=4.948 angstroms).

γ-hydride			
PDF No 03-065-6223			
d (Angstroms)	Intensity (a.u.)	(h k l)	Theta (degrees)
3.2428	0.1	(1 1 0)	13.741
2.7122	100	(1 1 1)	16.500
2.474	18	(0 0 2)	18.141
2.293	28.2	(2 0 0)	19.629
2.1774	0.1	(1 0 2)	20.718
1.9669	0.1	(1 1 2)	23.056
1.6818	18.9	(2 0 2)	27.26
1.6214	8.2	(2 2 0)	28.365

Table B-4 PDF for δ-hydride (a=4.781 angstroms).

δ-hydride			
PDF No 00-034-0649			
d (Angstroms)	Intensity (a.u.)	(h k l)	Theta (degrees)
2.760	100	(1 1 1)	16.206
2.391	47	(2 0 0)	18.794
1.6903	37	(2 2 0)	27.111
1.4415	43	(3 1 1)	32.301
1.3802	12	(2 2 2)	33.925
1.1952	7	(4 0 0)	40.127
1.0968	26	(3 3 1)	44.613
1.0691	26	(4 2 0)	46.096

Table B-5 PDF for δ-hydride (a=4.777 angstroms and ZrHx where x=2.16 wt.%).

δ-hydride			
PDF No 01-071-4972			
d (Angstroms)	Intensity (a.u.)	(h k l)	Theta (degrees)
2.758	100	(1 1 1)	16.218
2.3885	44.7	(2 0 0)	18.814
1.6889	28	(2 2 0)	27.135
1.4403	27.8	(3 1 1)	32.331
1.379	7.5	(2 2 2)	33.958
1.1943	3.2	(4 0 0)	40.166
1.0959	8.6	(3 3 1)	44.658
1.0682	7.7	(4 2 0)	46.148

Table B-6 PDF for δ-hydride (a=4.777 angstroms and ZrHx where x=1.77 wt.%).

δ-hydride			
PDF No 03-065-6972			
d (Angstroms)	Intensity (a.u.)	(h k l)	Theta (degrees)
2.758	100	(1 1 1)	16.218
2.389	45.2	(2 0 0)	18.814
1.689	27.8	(2 2 0)	27.135
1.440	27.8	(3 1 1)	32.331
1.379	7.5	(2 2 2)	33.958
1.194	3.2	(4 0 0)	40.166
1.096	8.6	(3 3 1)	44.658
1.068	7.7	(4 2 0)	46.148

Table B-7 PDF for ε-hydride (PDF# 00-036-1339).

ε-hydride			
PDF No 00-036-1339			
d (Angstroms)	Intensity (a.u.)	(h k l)	Theta (degrees)
2.761	100	(1 0 1)	16.200
2.489	50	(1 1 0)	18.026
2.225	29	(0 0 2)	20.251
1.760	29	(2 0 0)	25.954
1.659	63	(1 1 2)	27.666
1.484	63	(2 1 1)	31.265
1.381	31	(2 0 2)	33.916
1.367	23	(1 0 3)	34.292

Table B-8 PDF for ε-hydride (PDF #00-036-1340).

ε-hydride			
PDF No 00-036-1340			
d (Angstroms)	Intensity (a.u.)	(h k l)	Theta (degrees)
2.760	100	(1 0 1)	16.207
2.469	26	(1 1 0)	18.18
2.253	8	(0 0 2)	19.994
1.746	13	(2 0 0)	26.184
1.664	19	(1 1 2)	27.574
1.475	27	(2 1 1)	31.473
1.3780	21	(1 0 3)	33.942
1.3780	21	(2 0 2)	33.942

Table B-9 PDF for ε-hydride (PDF # 03-065-4542).

ε-hydride			
PDF No 03-065-4542			
d (Angstroms)	Intensity (a.u.)	(h k l)	Theta (degrees)
2.766	100	(1 0 1)	16.170
2.500	34.1	(1 1 0)	17.943
2.220	11.5	(0 0 2)	20.303
1.768	11.1	(2 0 0)	25.829
1.660	17.1	(1 1 2)	27.646
1.490	21	(2 1 1)	31.137
1.383	7.5	(2 0 2)	33.847
1.365	7.3	(1 0 3)	34.348

Bibliography

1. Lamarsh, J.R. and A.J. Baratta, *Introduction to Nuclear Engineering*. Third Edition ed. 2001, Upper Saddle River, NJ: Prentice Hall.
2. Lemaignan, C. and A.T. Motta, *Zirconium Alloys in Nuclear Applications*, in *Materials Science and Technology, A Comprehensive Treatment*, R.W. Cahn, P. Haasen, and E.J. Kramer, Editors. 1994, VCH: New York. p. 1-51.
3. Sabol, G.P. *ZIRLO - An alloy development success*. in *Zirconium in the Nuclear Industry: 14th International Symposium*. 2005: ASTM **1467** 3-24.
4. Garner, G.L. and J.-P. Mardon, *Alloy M5 in action.* Nuclear Engineering International, 2002. **47**(578): p. 36-37.
5. Clayton, J.C., *Cladding corrosion and hydriding in irradiated defected Zircaloy-4 fuel rods.* Corrosion, 1989. **45**(12): p. 996-1002.
6. Kearns, J.J., *Dissolution kinetics of hydride platelets in Zircaloy-4.* Journal of Nuclear Materials, 1968. **27**: p. 64-72.
7. Kearns, J.J., *Terminal solubility and partitioning of hydrogen in the alpha phase of zirconium, Zircaloy-2 and Zircaloy-4.* Journal of Nuclear Materials, 1967. **22**: p. 292-303.
8. McMinn, A., Darby, E.C., Schofield, J.S., *The Terminal Solid Solubility of Hydrogen in Zirconium Alloys.* Zirconium in the Nuclear Industry: The Twelfth International Symposium, 2000. **ASTM STP 1354**: p. 173-195.
9. Beck, R.L., *Zirconium-Hydrogen phase system.* Transactions of the ASM, 1962. **55**: p. 542-555.
10. Northwood, D.O. and U. Kosasih, *Hydrides and delayed hydrogen cracking in zirconium and its alloys.* International Metal reviews, 1983. **28**(2): p. 92-121.
11. Mishra, S., K.S. Sivaramakrishnan, and M.K. Asundi, *Formation of the gamma phase by a peritectoid reaction in the zirconium-hydrogen system.* Journal of Nuclear Materials, 1972. **45**: p. 235-244.
12. Racine, A., *Influence de l'orientation des hydrure sur les modes de deformation, d'endommagement et de rupture du Zircaloy-4 hydrure*, PhD Thesis in *Mecanique et Materiaux*. 2005, Ecole Polytechnique: Palaiseau, France.
13. Hillner, E., J.N. Kass, and J.J. Kearns, *Hydrogen supercharging during corrosion of Zircaloy.* Journal of Nuclear Materials, 1972. **45**: p. 175-178.
14. Marino, G.P., *Hydrogen supercharging in Zircaloy.* Material Sciences Engineering, 1971. **7**: p. 335-341.
15. Bradbrook, J.S., G.W. Lorimer, and N. Ridley, *The precipitation of zirconium hydride in zirconium and zircaloy-2.* Journal of Nuclear Materials, 1972. **42**(2): p. 142-160.
16. Nath, B., G.W. Lorimer, and N. Ridley, *Effect of hydrogen concentration and cooling rate on hydride precipitation in [alpha]-zirconium.* Journal of Nuclear Materials, 1975. **58**(2): p. 153-162.
17. Daum, R.S., *Hydride-Induced Embrittlement of Zircaloy-4 Cladding under Plane-Strain Tension*, PhD Thesis in *Materials Science*. 2007, The Pennsylvania State University: University Park.
18. Elston, J., *Hydrures*, in *Genie Atomique*, F. Perrin, Editor. 1965, INSTN-PUF. p. 249-278.
19. Zuzek, E., *H-Zr (Hydrogen-Zirconium)*, in *Binary Alloy phase diagram*, T.B. Massalski, Editor. 1990, (ASTM International). p. 2078-2080.

20. Libowitz, G.G., *A pressure-composition-temperature study of the zirconium-hydrogen system at high hydrogen contents.* Journal of Nuclear Materials, 1962. **5**(2): p. 228-233.
21. Cann, C.D., M.P. Puls, E.E. Sexton, and W.G. Hutchings, *The effect of metallurgical factors on hydride phases in zirconium.* Journal of Nuclear Materials, 1984. **126**(3): p. 197-205.
22. Westlake, D.G., *The habit planes of zirconium hydride in zirconium and zircaloy.* Journal of Nuclear Materials, 1968. **26**(2): p. 208-216.
23. Perovic, V., G.C. Weatherly, and C.J. Simpson, *Hydride precipitation in [alpha]/[beta] zirconium alloys.* Acta Metallurgica, 1983. **31**(9): p. 1381-1391.
24. Perovic, V., G.C. Weatherly, S.R. McEven, and M. Leger, *The influence of prior deformation on hydride precipitation in Zircaloy.* Acta metallurgica and materalia, 1992. **40**(2): p. 363-372.
25. Chung, H.M., R.S. Daum, J.M. Hiller, and M.C. Billone. *Characteristics of hydride precipitation in spent-fuel cladding*. in *Zirconium in the Nuclear Industry: 13th International Symposium*. 2002: ASTM STP 91878-101.
26. Hardie, D. and M.W. Shanahan, *Stress reorientation of hydrides in zirconium-2.5% niobium.* Journal of Nuclear Materials, 1975. **55**(1): p. 1-13.
27. Douglass, D.L., *The Metallurgy of Zirconium*, in *Atomic Energy Review*, Z.I. Turkov, Editor. 1971, International Atomic Energy Agency: Vienna, Austria.
28. Bertolino, G., G. Meyer, and J. Perez Ipiña, *Degradation of the mechanical properties of Zircaloy-4 due to hydrogen embrittlement.* Journal of Alloys and Compounds, 2002. **330-332**: p. 408-413.
29. Eadie, R.L. and C.E. Coleman, *Effect of stress on hydride precipitation in zirconium-2.5% niobium and on delayed hydride cracking.* Scripta Metallurgica, 1989. **23**(11): p. 1865-1870.
30. Mishima, Y., S. Ishino, and S. Nakajtma, *A resistometric study of the solution and precipitation of hydrides in unalloyed zirconium.* Journal of Nuclear Materials, 1968. **27**(3): p. 335-344.
31. Une, K. and S. Ishimoto, *Dissolution and precipitation behavior of hydrides in Zircaloy-2 and high Fe Zircaloy.* Journal of Nuclear Materials, 2003. **322**(1): p. 66-72.
32. Root, J.H. and R.W.L. Fong, *Neutron diffraction study of the precipitation and dissolution of hydrides in Zr-2.5Nb pressure tube material.* Journal of Nuclear Materials, 1996. **232**(1): p. 75-85.
33. Kammenzind, B.F., B.M. Berquist, R. Rajaj, P.H. Kreyns, and D.G. Franklin. *The long-range migration of hydrogen through Zircaloy in response to tensile and compressive stress gradients*. in *Zirconium in the Nuclear Industry: 12th International Symposium*. 2000: ASTM STP 1354196-233.
34. Ells, C.E., *The stress orientation of hydride in zirconium alloys.* Journal of Nuclear Materials, 1970. **35**(3): p. 306-315.
35. Singh, R.N., R. Kishore, S.S. Singh, T.K. Sinha, and B.P. Kashyap, *Stress-reorientation of hydrides and hydride embrittlement of Zr-2.5 wt% Nb pressure tube alloy.* Journal of Nuclear Materials, 2004. **325**(1): p. 26-33.
36. Kim, Y.S., Y. Perlovich, M. Isaenkova, S.S. Kim, and Y.M. Cheong, *Precipitation of reoriented hydrides and textural change of [alpha]-zirconium grains during delayed hydride cracking of Zr-2.5%Nb pressure tube.* Journal of Nuclear Materials, 2001. **297**(3): p. 292-302.
37. Cox, B., *Environmentally-induced cracking of zirconium alloys -- A review.* Journal of Nuclear Materials, 1990. **170**(1): p. 1-23.
38. Dutton, R., K. Nuttal, M.P. Puls, and L.A. Simpson, *Mechanisms of hydrogen cracking in zirconium and its alloys.* International Metal reviews, 1977. **28**(2): p. 92-121.

39. Simpson, C.J. and C.E. Ells, *Delayed hydrogen embrittlement in Zr-2.5 wt % Nb.* Journal of Nuclear Materials, 1974. **52**(2): p. 289-295.
40. Chung, H.M. *Understanding hydride- and hydrogen-related processes in high-burnup cladding in spent-fuel storage and accident situations*. in *Proceeding of International Meeting on LWR Fuel performance*. 2004. Orlando, Fl470-479.
41. Simpson, L.A. and M.P. Puls, *The effects of stress temperatures and hydrogen content on hydride-induced crack growth in Zr-2.5 Pct Nb.* Metallurgical Transactions A, 1979. **10A**: p. 1093-1105.
42. Shi, S.Q. and M.P. Puls, *Criteria for fracture initiation at hydrides in zirconium alloys I. Sharp crack tip.* Journal of Nuclear Materials, 1994. **208**(3): p. 232-242.
43. Shi, S.Q., M.P. Puls, and S. Sagat, *Criteria of fracture initiation at hydrides in zirconium alloys II. Shallow notch.* Journal of Nuclear Materials, 1994. **208**(3): p. 243-250.
44. Mills, J.S. and F.H. Huang, *Delayed hydride cracking behavior for Zircaloy-2 plate.* Engineering Fracture Mechanics, 1991. **39**(2): p. 241-257.
45. Coleman, C.E. *Effect of texture on hydride reorientation and delayed hydrogen cracking in cold-workied Zr-2.5Nb*. in *Zirconium in the Nuclear Industry: 5th conference*. 1982: ASTM STP 754
46. Xu, F., R.A. Holt, M.R. Daymond, R.B. Rogge, and E.C. Oliver, *Development of internal strains in textures Zircaloy-2 during uni-axial deformation.* Materials Science and Engineering: A, 2008. **473**(1-2): p. 139-146.
47. Kearns, J.J. and C.R. Woods, *Effect of texture, grain size, and cold work on the precipitation of irented hydrides in Zircaloy tubing and plate.* Journal of Nuclear Materials, 1966. **20**(3): p. 241-261.
48. SCDAP/RELAP5/MOD2, *Code Manual volume 4: MATPRO: "A Library of Materials Properties for Light Water Reactor Accident Analysis"*, NUREG/CR-5273, Editor. 1990.
49. Pierron, O.N., D.A. Koss, and A.T. Motta, *Tensile specimen geometry and the constitutive behavior of Zircaloy-4.* Journal of Nuclear Materials, 2003. **312**(2-3): p. 257-261.
50. Lepage, A.D., W.A. Ferris, and G.A. Ledoux, *Procedure for Adding Hydrogen to Small Sections of Zirconium Alloys*. 2004, IAEA Report FC-IAEA-03.
51. Kim, Y.S., S.B. Ahn, and Y.M. Cheong, *Precipitation of crack tip hydrides in zirconium alloys.* Journal of Alloys and Compounds, 2007. **429**(1-2): p. 221-226.
52. Cullity, B.D., *Elements of X-ray Diffraction*. Second Edition ed. 1978: Addison-Wesley Publishing Company, Inc.
53. *The Powder Diffraction File*. 2006, International Center for Diffraction Data.
54. Motta, A.T., K.T. Erwin, O. Delaire, R.C. Birtcher, Y.S. Chu, J. Maser, D.C. Mancini, and B. Lai. *Synchrotron Radiation Study of Second-Phase Particles and Alloying Elements in Zirconium Alloys*. in *Zirconium in the Nuclear Industry: 13th International Symposium*. 2002: ASTM International**ASTM STP 1423** 59-79.
55. Haeffner, D.R., J.D. Almer, and U. Lienert, *The use of high energy X-rays from the Advanced Photon Source to study stresses in materials.* Materials Science and Engineering: A, 2005. **399**(1-2): p. 120-127.
56. Cameron, D.J. and R.G. Duncan, *On the existence of a memory effect in hydride precipitation in cold-worked Zr-2.5% Nb.* Journal of Nuclear Materials, 1977. **68**: p. 340-344.
57. Larson, A.C. and R.B.V. Dreele, *General Structure Analysis System (GSAS)*. 2000, Los Alamos National Laboratory.
58. Bischoff, J., *Evolution of the Oxide Structure of Ferritic-Martensitic Steels Exposed to Supercritical Water*, M.Sc Thesis *Nuclear Engineering*. 2008, The Pennsylvania State University: University Park.

59. Daum, R.S., Y.S. Chu, and A.T. Motta, *Identification and quantification of hydride phases in Zircaloy-4 cladding using synchrotron X-ray diffraction.* Journal of Nuclear Materials, 2008. **In Press, Corrected Proof**.
60. Schrire, D.I. and J.H. Pearce. *Scanning electron microscope techniques for studying Zircaloy corrosion and hydriding*. in *Zirconium in the Nuclear Industry: 10th International Symposium*. 1994: ASTM STP 124598-115.